

**Department of Physics and Astronomy  
Heidelberg University**

Master Thesis in Physics  
submitted by

**Christian Amos Gölzhäuser**

born in Heidelberg (Germany)

**2025**

---

**Generation and Optimisation of arbitrarily shaped  
attractive trapping potentials for quasi-2D dysprosium  
quantum gases**

This Master Thesis has been carried out by  
**Christian Amos Gölzhäuser**  
at the  
**Physical Institute**  
of the  
**Ruprecht Karl University of Heidelberg**  
under the supervision of  
**Prof. Dr. Lauriane Chomaz**

---

**Abstract** In the Dysprosium Lab (DyLab) of the Quantum Fluids (QF) group at the Physical Institute of the University of Heidelberg, we aim to investigate ultracold dipolar quantum gases in reduced dimensionality and tailored geometry. Ultracold gases have proved to be a versatile platform to study a wide variety of different quantum phenomena emerging as classical behaviour is increasingly suppressed at finite temperatures near absolute zero. Dipolar gases in which standard contact interactions and anisotropic dipole-dipole interactions are competing additionally offer enhanced control over the internal interactions and have exhibited fundamentally different behaviour than a regular contact interacting gas, for example spontaneous density modulations. In this thesis, we report on the planning, development and implementation of an optical setup, allowing us to imprint tailored attractive potentials onto a quasi-2D dipolar quantum gas. Herein arbitrarily shaped potentials can be created through an amplitude modulation of a 532 nm laser beam with a digital micromirror device (DMD). The modulation can be iteratively optimized within one part of the optical setup by feeding the recorded intensity profile of the laser beam back to an algorithm which calculates a correction to be applied to the DMD pattern. Two different approaches to the iterative optimization were implemented and tested in a light-based setting, a global and a local (pixel-based) one. The optimised beam is sent, through another part of the optical setup, onto a high resolution microscope allowing us to produce a demagnified image of the DMD pattern at the position of the atomic cloud and therefore create arbitrarily shaped optical dipole traps.

**Kurzfassung** Im Dysprosium-Labor (DyLab) der Quantum Fluids (QF) Gruppe am Physikalischen Institut der Universität Heidelberg erforschen wir ultrakalte dipolare Quantengase in reduzierter Dimensionalität und maßgeschneiderter Geometrie. Ultrakalte Gase haben sich als vielseitige Plattform zur Untersuchung einer Vielzahl unterschiedlicher Quantenphänomene erwiesen, die auftreten, wenn klassisches Verhalten bei endlichen Temperaturen nahe dem absoluten Nullpunkt zunehmend unterdrückt wird. Dipolare Gase, in denen sowohl die üblichen Kontaktwechselwirkungen als auch anisotrope Dipol-Dipol-Wechselwirkungen miteinander konkurrieren, bieten darüber hinaus eine erweiterte Kontrolle über die internen Wechselwirkungen und zeigen ein grundsätzlich anderes Verhalten als reguläre, nur kontaktwechselwirkende Gase, beispielsweise das Auftreten spontaner Dichtemodulationen. In dieser Arbeit berichten wir über die Planung, Entwicklung und Implementierung eines optischen Aufbaus, der es uns ermöglicht, maßgeschneiderte attraktive Potentiale auf ein quasi-zweidimensionales dipolares Quantengas zu projizieren. Hierbei können beliebig geformte Potentiale durch eine Amplitudenmodulation eines 532-nm-Laserstrahls mittels eines Digital Micromirror Device (DMD) erzeugt werden. Die Modulation kann in einem Teil des optischen Aufbaus iterativ optimiert werden, indem das aufgezeichnete Intensitätsprofil des Laserstrahls an einen Algorithmus zurückgeführt wird, der eine Korrektur für das auf das DMD aufgebrachte Muster berechnet. Zwei verschiedene Ansätze zur iterativen Optimierung wurden implementiert und in einem lichtbasierten Aufbau getestet: ein globaler sowie ein lokaler (pixel-basierter) Ansatz. Der optimierte amplitudenmodulierte Laserstrahl wird in einem weiteren Teil des optischen Aufbaus in ein hochauflösendes Mikroskop geleitet, das eine verkleinerte Abbildung des Musters auf dem DMD an der Position der Atomwolke erzeugt und es uns somit ermöglicht, optische Dipolfallen in beliebiger Form zu realisieren.

# Contents

<b>1</b>	<b>Introduction</b>	<b>4</b>
<b>2</b>	<b>Experimental Background</b>	<b>6</b>
2.1	Dipolar quantum gases . . . . .	6
2.2	DyLab setup in Heidelberg . . . . .	8
<b>3</b>	<b>Theoretical Background</b>	<b>11</b>
3.1	Properties of dysprosium . . . . .	11
3.2	Optical trapping . . . . .	12
3.3	Trap shaping . . . . .	16
3.4	Polarizability calculations . . . . .	18
3.4.1	530 nm transition . . . . .	20
3.4.2	684 nm transition . . . . .	22
<b>4</b>	<b>Beam shaping optics</b>	<b>24</b>
4.1	Fourier optics . . . . .	24
4.1.1	Light propagation in free space . . . . .	24
4.1.2	Lens in a 2f setup . . . . .	25
4.1.3	Diffraction . . . . .	26
4.2	Gibbs-phenomenon . . . . .	27
4.3	DMD optics . . . . .	28
4.3.1	DMD illumination . . . . .	29
4.3.2	Greyscaling . . . . .	30
4.3.3	Dithering . . . . .	31
<b>5</b>	<b>DMD Imaging Setup</b>	<b>33</b>
5.1	Characterization . . . . .	36
5.1.1	Collimation in Fourier-space . . . . .	36
5.1.2	Point spread function in the image plane . . . . .	39
5.1.3	Modulation transfer function in the imaging plane . . . . .	40
5.1.4	Pointing stability . . . . .	42
5.2	Inclusion of microscope objective . . . . .	44
5.2.1	Alignment . . . . .	44
5.2.2	Imaging tests . . . . .	45
5.2.3	Optimisation mismatch in transmission and reflection . . . . .	46
<b>6</b>	<b>Optimisation algorithms</b>	<b>51</b>
6.1	Filtering optimisation . . . . .	51
6.2	Errormap optimisation . . . . .	53
6.2.1	Implementation and adaptation . . . . .	57
6.3	Smooth borders . . . . .	62
6.3.1	Target manipulation . . . . .	62
6.3.2	Corrected pattern manipulation . . . . .	65
6.3.3	Gradient pattern manipulation . . . . .	66
6.4	Evaluation . . . . .	66
6.4.1	Root Mean Square Error . . . . .	67
6.4.2	Grey Level Co-occurrence Matrix . . . . .	68

---

6.4.3	Density perturbation . . . . .	72
<b>7</b>	<b>Integration into DyLab setup</b>	<b>77</b>
7.1	Laser setup . . . . .	77
7.2	Alignment . . . . .	77
7.3	Pattern Generation and Optimisation Tool . . . . .	80
7.3.1	Generation . . . . .	80
7.3.2	Calibration . . . . .	81
7.3.3	Optimisation . . . . .	82
<b>8</b>	<b>Outlook</b>	<b>84</b>

# 1 Introduction

If modern physics experiments were to be described with a single word, it would probably be 'complex'. While complex is a broad term and can refer to many different aspects, in the context of a modern experiment, it probably most fittingly refers to the absolute abundance of small individual components which make up such an experiment. Many parts have undergone years if not decades of development themselves only to become one small mean to a much more complex end. Experiments on dilute atomic or molecular gases, cooled to degeneracy can (unlike let's say kilometre long evacuated tubes for example) often be confined in size to a moderately spacious laboratory. Yet they still involve hundreds if not thousands of small independent parts and setups and usually require a whole team to build and operate. It has become almost impossible for a single person to oversee such an operation. The (in retrospect romanticized) times when individual 'universal geniuses' or polymaths locked themselves in a room to design and conduct simple yet groundbreaking experiments or laid out theoretical foundations of modern physics are most definitely over and it is probably for the better, because if scientific research would still work this way, there is no way we would have made the incredible discoveries our modern and complex experiments on ultracold quantum gases have produced in the last few decades.

All that is to say that this Master's thesis, like many before only highlights one component of the experimental setup we are building in our dysprosium lab in Heidelberg and the development of this setup is based on the works of many excellent scientists from the past and was aided by a whole team of excellent scientists from the present. In the experiment which has been constructed since the beginning of 2022, we plan to probe fundamental equilibrium and out of equilibrium dynamics of an ultracold dipolar quantum gas of dysprosium atoms in reduced dimensionality and a tailored-shape potential geometry. The last part, namely the tailored-shape potential is where the component which will be described in detail in this thesis comes in. We report on the development of an optical setup, which is supposed to allow us to produce monochromatic light beams with an arbitrarily shaped intensity distribution with a Digital Micromirror Device (DMD). Such an arbitrarily shaped beam, projected onto a cloud of ultracold dipolar atoms imposes a tailored attractive optical potential. As one application of this setup, we aim to produce an intensity distribution, which is as flat and uniform as possible, so that atoms in this tailored potential are ideally all exposed to the same attractive forces and thus constitute a homogeneous system. The setup can though also be used to dynamically introduce disorder into the system to then probe its response.

A brief outline of the now following chapters of this thesis is given below:

**Chapter 2:** In this chapter a brief overview over the experimental background in the field of ultracold atoms and dipolar systems in general and the dysprosium experiment (or DyLab) in Heidelberg in particular will be given. The progress of DyLab is summarized until the beginning of 2025.

**Chapter 3:** We will go over some theoretical aspects which are relevant for the optical setup we are planning to build, yet are not directly related to optics. In particular we will highlight what distinguishes dipolar atoms such as dysprosium from species with a predominantly isotropic behaviour such as alkali atoms. We do this especially in the context of coherent atom-light interactions.

**Chapter 4:** We next introduce optical phenomena which are relevant for our setup. Especially

focusing on optical Fourier transforms, the reconstruction of real space images from Fourier components and the diffraction of light from apertures as these things will become important in the subsequent chapters. We also go over some techniques which are related specifically to beam shaping with a Digital Micromirror Device.

**Chapter 5:** In this chapter we will move on to describing the optical setup. We summarize what our goals for this setup were, how we set out to achieve them and perform a series of different tests to characterize and optimise the system we ultimately built. We also go over the challenge of including an external light-based optimisation routine for the intensity distribution of the beam.

**Chapter 6:** This chapter is solely concerned with the development and implementation of an optimisation algorithm to improve the production of a tailored shape beam from a Gaussian beam. We discuss two different approaches to this challenge and evaluate the results.

**Chapter 7:** In the penultimate chapter we discuss the implementation of our optical setup into the main experiment and go over a tool to simplify the generation, optimisation and monitoring of arbitrary beam shapes to be used in the main experimental sequence.

**Chapter 8:** In this last part of this thesis the results gathered from our various tests and characterizations of the optical setup are summarized and some ideas for future projects to improve, alter or utilize the setup are proposed.

## 2 Experimental Background

From the time when Albert Einstein, building on works of Satyendranath Bose, first predicted a macroscopic occupation of the lowest quantum state in a gas of identical particles with integer spin (now known as bosons) at finite temperature near absolute zero in 1924 [18], to the time when a gas of neutral atoms has been cooled to degeneracy and the first instance of such a Bose-Einstein condensate (BEC) has been observed in an experiment in 1995[1][36], it took about 70 years. In the last 30 years however, physicists all over the world have built vacuum systems, aligned lasers, magnetic fields and lots of optics to set up similar experiments to cool atoms or molecules down to an ultracold regime, where quantum effects are exalted. Ultracold quantum gases, be it single, few or many body systems have been proven to be an excellent platform to study not only Bose-Einstein condensation or Fermi degeneracy, but also other even more exotic quantum phenomena by making use of the great degree of tunability these systems provide. By engineering a suitable external environment one can tune the parameters of an ultracold system to explore far from equilibrium dynamics, phase transition driven through quantum fluctuations or few or many-body interactions in a nearly arbitrary geometry and dimensionality. In recent years the ability of ultracold atom systems to simulate dynamics of condensed matter systems such as superconductivity or in principle simulate any dynamics encoded in a Hamiltonian has sparked particular interest since it brought up the notion of ultracold quantum gases as a platform for quantum simulation. Special geometries such as tweezer arrays or lattices with one atom per lattice site can also serve as a platform for quantum computing with single atoms acting as qubits and information being encoded in them as internal states [13].

### 2.1 Dipolar quantum gases

What has also drawn attention in recent years are dipolar quantum systems. These may be constituted out of dipolar atoms or also molecules and have exhibited dynamics which are fundamentally different from non-dipolar systems. Within all ultracold atom systems, we are usually dealing with contact interactions between the particles. On top of that in dipolar systems we have also dipole-dipole interactions. Other than the contact interactions, they are long-range and anisotropic. Dipole-dipole interactions can be characterized by the following relation on the distance between dipoles  $r$  and their respective orientation  $\theta$  to each other.  $\theta = 0$  represents an attractive head to tail arrangement of the dipoles to each other, while  $\theta = \pi/2$  represents the repulsive side by side configuration.

$$V_{dd}(r, \theta) = \frac{C_{dd}}{4\pi} \frac{1 - 3 \cos^2 \theta}{r^3} \quad (2.1)$$

Here  $C_{dd}$  is a coupling constant characterizing the strength of the interaction, it depends on the magnetic moment of the atomic species (see 3.1). In a dipolar quantum gas, the two interactions, contact and dipolar, are competing. Whichever kind of interaction is dominant is usually indicated through the ratio of their respective characteristic length scales  $\epsilon_{dd} = \frac{a_{dd}}{a_s}$  with  $a_{dd}$  the dipolar length and  $a_s$  the s-wave scattering length. If  $\epsilon_{dd} > 1$  dipolar interactions dominate, if  $\epsilon_{dd} < 1$  contact interactions dominate. The s-wave scattering length can be tuned through Feshbach resonances and thus we can dynamically tune our system into a more or less dipolar regime.

What has made dipolar gases particularly interesting is that it was theoretically proposed that the dipolar interaction term in the Gross-Pitaevskii equation (GPE), which at sufficiently low temperatures describes the evolution of the system, gives rise to a minimum in the dispersion

relation at a finite spatial frequency. The GPE can be written as [49]:

$$i\hbar \frac{\partial \Psi}{\partial t} = \left[ -\frac{\hbar^2}{2m} \Delta + V(\vec{r}) + \frac{4\pi\hbar^2 a_s}{m} |\Psi|^2 + \frac{\mu_0 \mu_m^2}{4\pi} \int \frac{1 - 3 \cos^2 \theta}{|\vec{r} - \vec{r}'|^3} |\Psi(\vec{r}')|^2 d\vec{r}' \right] \Psi \quad (2.2)$$

There are three terms to it. In the order as they appear on the right hand side of 2.2, they are a kinetic term, a term for an external potential, a term for the interatomic contact interactions and last but not least a term for the dipolar interactions.

The minimum that appears resembles one predicted by Lev Landau in 1941 in the context of liquid Helium II[39]. He at that time coined the name 'roton' for the quasiparticle which may be excited at the minimum in the dispersion relation, since he assumed it may be related to vortex excitations and thus have a rotational character. Nowadays we know that there is nothing rotational about the roton, but it is rather a collective excitation of the system at a finite characteristic spatial frequency, yet the term roton carries on.

In 2003 a similar dispersion relation like Landau found for Helium II was also calculated for dipolar quantum systems[24][53][4]. The dispersion relation in terms of the wavenumber  $q$  for a two-dimensional dipolar gas, which we are particularly interested in reads [38]:

$$\epsilon(q) = \sqrt{\frac{\hbar^2 q^2}{2m} \left[ \frac{\hbar^2 q^2}{2m} + 2n_{2D} \left( g_{2D} + \tilde{V}_{dd}^{2D}(q) \right) \right]} \quad (2.3)$$

Here  $n_{2D}$  is the density in 2D and  $g_{2D}$  and  $\tilde{V}_{dd}^{2D}(q)$  are the coupling constant for the contact interactions and the Fourier transform of the dipolar interaction potential, both for the 2D case. In Figure 1 (a) we can observe a schematic of the system considered in the case of 2.3. 2D layers of a dipolar gas are confined in  $z$  direction. Dipoles are aligned in  $z$  direction through an external field as well. In Figure 1 (b), 2.3 is plotted for a suitable set of parameters where the roton minimum is clearly visible. Both Figures are from [38]

If our system becomes more and more dipolar, i.e.  $\epsilon_{dd}$  is adiabatically increased above one,

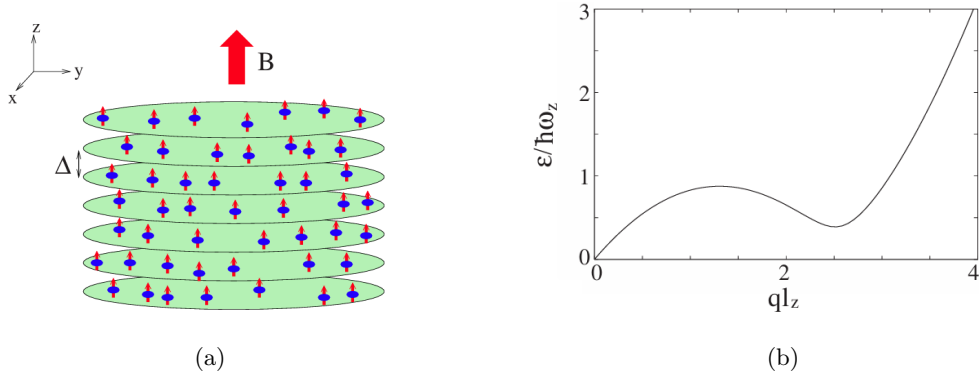


Figure 1: (a) 2D layers of dipolar atoms, separated by a spacing  $\Delta$ . (b) Dispersion relation of a 2D dipolar gas.  $X$ -axis scaled with the characteristic length of the harmonic oscillator ground state  $l_z = \sqrt{\hbar/m\omega_z}$  and  $y$ -axis in units of  $\hbar\omega_z$ ,  $\omega_z$  being the trapping frequency in  $z$ -direction. Roton minimum visible at  $ql_z \approx 2.5$

. Figures from [38].

the roton minimum not only forms, but its energy gap will reduce until it eventually approaches zero. Once the roton gap is closed, density modulated modes at finite spatial frequency will be spontaneously populated. The gas will then assume a crystal-like modulated density structure while global phase coherence is conserved, hence the term 'supersolid' for this phenomenon. This

was indeed experimentally observed in three dipolar gas experiments around the same time in 2019 [12][9][58]. What plays a critical role in the stabilization of the supersolid phase are quantum fluctuations. If dipolar atoms are bunched together in a droplet, they will partly be stacked on top of each other in an attractive head-to-tail configuration. In mean-field theory this arrangement leads to a collapse of the system. It is only through a beyond mean-field correction accounting for fluctuations that a stabilization of the system at finite density is predicted [59]. This correction is known as the Lee-Huang-Yang (LHY) term in the GPE [40].

In our new experiment at the Physical Institute of the University of Heidelberg, we aim to produce an ultracold dipolar quantum gas of dysprosium atoms in well controlled trap geometries to explore exotic quantum states such as supersolids and quantum droplets and study out of equilibrium dynamics.

## 2.2 DyLab setup in Heidelberg

In this section, the development of our dysprosium experiment or in short DyLab up until the current state will be briefly summarized. More in-depth references on individual parts of the setup will be pointed out along the way.

Our vacuum setup consists of a high-vacuum (HV) and an ultra-high-vacuum (UHV) section separated by a differential pumping stage. We reach a stable vacuum of roughly  $10^{-9}$  mbar and  $10^{-11}$  mbar in the HV and UHV section respectively[30]. The main component of the HV part is our 2D-MOT chamber of titanium. Atoms enter the chamber from a high temperature oven mounted horizontally on one side. The oven is typically operated at a temperature of  $800^{\circ}\text{C}$  with a hot lip at  $1100^{\circ}\text{C}$ . This is well below the melting point of dysprosium ( $1407^{\circ}\text{C}$ ), but it allows us to generate enough vapour pressure to produce a hot jet of atoms entering the 2D-MOT chamber. Our 2D-MOT itself consists of single laser beams at 421 nm and 400 mW which is sent through the chamber in a retroreflected bow-tie configuration and a total of eight stacks of permanent magnets forming a gradient of around 27 G/cm in the centre of the chamber and creating a very thin cigar shaped spatial confinement along the central axis of the experiment. With a capture velocity of around 100 m/s we manage to trap only a small fraction of the total jet of atoms, yet we manage to use the 2D-MOT as a compact source from which we can load our 3D-MOT[21][34]. The 3D-MOT is located in the UHV part. Atoms are pushed through the differential pumping stage into the main science chamber and recaptured in the 3D-MOT. The 3D-MOT is formed with three orthogonal and retroreflected laser beams at 626 nm and about 85 mW power in each beam. The magnetic field is produced by a pair of coils in anti-Helmholtz configuration, which are mounted above and below the chamber[55]. With this setup we produce a gradient of 0.42 G/cm. In the 3D-MOT we reach a capture velocity of about 10 m/s. We are able to load on the order of  $10^8$  atoms maximum in 4 s. The temperature after compression of the MOT is around 15-20  $\mu\text{K}$ .

In order to reach degeneracy in however the dissipative radiation pressure force exerted by a MOT is insufficient, which is why we load an optical dipole trap from our 3D-MOT. In the optical dipole trap, atoms are confined due to the conservative dipole force without the need of magnetic fields. Our attractive optical dipole trap consists of two 1064 nm beams whose waists are overlapped with each other near the position of the 3D-MOT to ensure efficient loading. ODT arm 1 has a waist of about  $34\ \mu\text{m}$  at around 37 W power. Arm 2's waist is roughly  $67\ \mu\text{m}$  at a power of about 12 W. To transfer the atoms from the MOT to the ODT, we first compress the MOT spatially. By decreasing the current in the coils and thus the gradient field, we can increase the confinement. We compress the MOT for 120 ms, while in the last 7 ms of the compression ODT arm 1 is ramped up to full power. We continue to hold the compressed MOT for another 50 ms and then turn it off. With

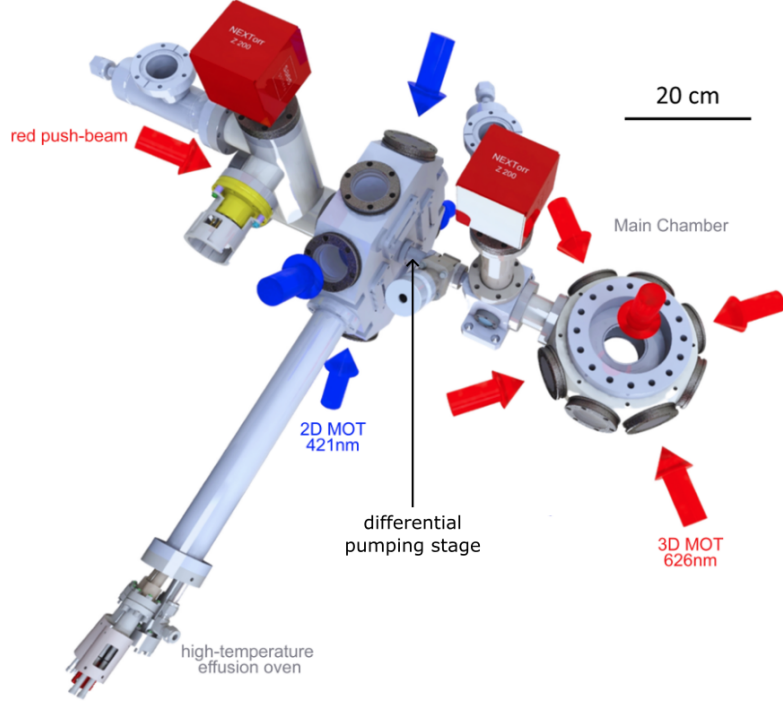


Figure 2: 3D model of the vacuum setup with blue and red arrows to indicate the 2D and 3D-MOT beams. Figure adapted from [56]

optimized parameters we are able to load around  $5 \times 10^7$  atoms in the optical dipole trap. By ramping down the power of the ODT in steps one can evaporatively cool the atoms in the trap below the critical temperature for Bose-Einstein condensation. In 2023 we reached a stable BEC of around  $1.5 \times 10^5$  atoms with a condensate fraction of about 70%.

In a next step we implemented an accordion lattice to go towards a 2D gas. The lattice is produced by two laser beams at 532 nm interfering at a shallow angle and thus creating multiple pancake like layers along the vertical axis in which atoms can be trapped through attractive dipole forces. The thickness and spacing of the layers can be tuned dynamically by changing the angle under which the beams enter the main chamber[56][17]. When atoms are loaded in the accordion lattice, a quasi-2D regime is reached as atoms are strongly confined along one direction. We typically speak of a quasi-2D regime, since unlike in a pure 2D system, motion along the confined direction is not entirely frozen out and dynamics are still modified through out-of-plane interactions.

We can impose attractive light potentials formed from 532 nm light onto the atom cloud through the vertical axis. The light potentials can be arbitrarily tailored with a Digital Micromirror Device (DMD). For now we aim to produce flat box-like potentials to ensure a high degree of homogeneity in our gas. We are able to image the atom cloud through a variety of different imaging setups. In the case of imaging the effect of the DMD on the atoms we primarily use our vertical absorption imaging system including a custom made microscope objective[48]. The microscope serves a dual purpose as it is itself also a part of the DMD imaging setup.

The alignment of the accordion lattice, the microscope and the DMD all in a good reference to each other and to the BEC in the ODT were no doubt challenging. However in the beginning of 2025 we for the first time achieved a configuration which allowed us to trap a quantum degenerate gas in the accordion lattice with a maximum trapping frequency of 1.2 kHz and also observe a clear signal of the DMD on the atoms. We were also able to observe the first evidence of supersolidity in the accordion.

In the future we want to continue to study also other exotic supersolid phases as well as utilize the DMD to probe dynamics of a homogeneous dipolar condensate and the systems response to dynamic perturbations.

### 3 Theoretical Background

In this chapter we will go over some of the basic principles of optical trapping of dipolar quantum gases. Since we are working with dysprosium, we will start out with a general review of the properties of dysprosium in 3.1 and then move on to the theory behind optical dipole traps (ODTs) in 3.2. We also go over the difficulties of implementing an ODT with dysprosium atoms due to their anisotropic properties and ultimately move towards creating arbitrary trap geometries with far detuned attractive or also repulsive laser light in 3.3 and 3.4.

#### 3.1 Properties of dysprosium

As mentioned above and in the summary of the current state of our experiment in Heidelberg, we are working with many-body systems of ultracold dysprosium atoms. The word dysprosium is derived from the Greek word *δυσπρόσιτος* (*dysprósitos*), which roughly translates to 'hard to get' or 'hardly accessible'. The reason for that being that still today the isolation of dysprosium out of its naturally occurring compounds, mostly in oxides, is an intricate and elaborate process.

Dysprosium can be found in the bottom part of the periodic table in the separate strip of the lanthanides and actinides. Like erbium, terbium and holmium it is part of the open-shell lanthanides, meaning, the  $4f$  shell, which can be filled with up to 14 electrons is only partly filled. Note that the  $4f$  shell is actually not the outermost shell of the lanthanides, but it is in fact the spherically symmetric  $6s$  shell, which however is fully filled with two atoms in the lanthanide ground state. The electrons in the open  $4f$  shell though carry large angular momentum quantum numbers and are ultimately responsible for the magnetic and dipolar properties of open-shell lanthanides. The electron configuration in the ground state of dysprosium is typically written as:

$$[\text{Xe}]4f^{10}6s^2 \quad (3.4)$$

meaning we have a set of fully filled shells corresponding to the electron configuration of xenon and on top of that 10 electrons in the  $4f$  shell and 2 in the  $6s$  shell. While the  $6s$  shell is thus fully filled, we have according to Hund's rules, in the  $4f$  shell four unpaired electrons in the ground state resulting in an orbital angular momentum quantum number  $L = 6$  and a spin quantum number  $S = 2$ , which together yield a total angular momentum quantum number  $J = 8$  ( $L = 5$ ,  $S = 1$  and  $J = 6$  for erbium) [45].

The magnetic dipole moment  $\mu$  of a bosonic atom is related to the total angular momentum via:

$$\mu = g_J \mu_B \sqrt{J(J+1)} \quad (3.5)$$

with  $g_J$  the Landé-factor and  $\mu_B$  the Bohr magneton. The Landé-factor of the ground state in LS-coupling is calculated the following way:

$$g_J = 1 + g_S \left[ \frac{J(J+1) - L(L+1) + S(S+1)}{2J(J+1)} \right] \quad (3.6)$$

With  $g_S \approx 2$  the gyromagnetic ratio. For dysprosium and erbium we thus get  $g_J \approx 1.25$  and  $g_J \approx 1.17$  respectively leading to a magnetic moment of  $10\mu_B$  for dysprosium and  $7\mu_B$  respectively. Dysprosium and terbium actually have the highest magnetic moment of the periodic table. An overview over the above listed elements can be seen in Tab. 1. Another characteristic of the open-shell lanthanides is, that every second element has only a single stable isotope, meaning while there is only one stable terbium isotope, there are seven stable dysprosium isotopes and while three of

them are very rare, the other four are roughly evenly abundant, with two of them bosonic and two fermionic (see Tab. 2). All this makes dysprosium a prime candidate to study dipolar quantum many body systems in ultracold gas experiments due to the degree tunability it offers and the availability of different isotopes for bosonic gases or also fermionic few body systems.

Element	Tb	Dy	Ho	Er
Atomic number [Z]	65	66	67	68
Magnetic moment	$10\mu_B$	$10\mu_B$	$9\mu_B$	$7\mu_B$
Stable isotopes	1	7	1	6

Table 1: Properties of some open shell lanthanides

Isotope	$^{161}\text{Dy}$	$^{162}\text{Dy}$	$^{163}\text{Dy}$	$^{164}\text{Dy}$
Natural abundance [%]	18.9	25.4	24.9	28
Atomic mass [u]	161	162	163	164
Quantum statistics	fermionic	bosonic	fermionic	bosonic

Table 2: Overview of the four most abundant stable isotopes of dysprosium

When it comes to cooling and trapping of the atoms, erbium and dysprosium are again relatively similar. Alkali atoms which were the first elements to be cooled to degeneracy, and have a relatively simple level structure as well as isotropic properties when it comes to interatomic or also atom-light interactions. In the case of dysprosium and erbium, the internal structure is much more complicated and the open  $4f$  shell introduces orbital anisotropy. Below in 3 the electronic level systems for erbium and dysprosium are shown. Even though the level structure may seem chaotic at first sight, we can see, that the typical transitions used for cooling are the same in both species and even lie in a similar region regarding their wavelength. There is a broad blue transition in which one of the electrons in the  $6s$  shell is excited into the  $6p$  shell in a triplet state at 421 nm and 401 nm dysprosium and erbium respectively. There is also the more narrow intercombination line at which the electron is excited into the  $6p$  shell in a singlet state at 626 nm and 583 nm respectively. And even though we are not using this transition there is also a very narrow line exciting one of the electrons from the  $4f$  shell into the  $5d$  shell at 741 nm for dysprosium and both at 631 nm and 841 nm for erbium. In addition to these  $J$  to  $J + 1$  transitions which are shown in Figure 3, there are many more, in particular such with  $J$  to  $J$  and  $J$  to  $J - 1$ . Of those we will later on examine the one at 530 nm and at 684 nm in more detail later on in 3.4

In addition to using these transitions for trapping and cooling of the atoms through light scattering, we can employ laser light which is detuned far from transition to trap atoms through the interaction of a light-induced dipole in the atom with the light field itself. This scheme will be introduced further in the next section.

### 3.2 Optical trapping

There are different ways of trapping neutral atoms with lasers, which are being applied in different scenarios. As mentioned before in 2.2 radiation pressure traps such as a MOT exert a dissipative force onto the atoms. This is essential for primary trapping and cooling stages. We however will focus on the mechanism of an optical dipole trap (ODT) and do so mostly in line with [26]. In an ODT a conservative force is exerted onto the atoms and random scattering is suppressed. Its mechanism employs light which is far detuned from an atomic transition. The oscillating electric field of the laser induces an atomic dipole moment in the atom which in turn oscillates at the same

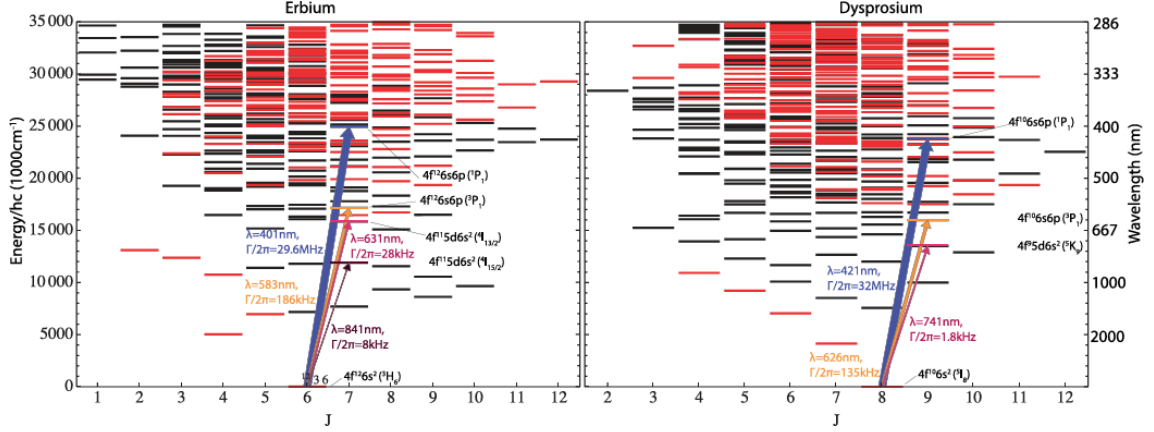


Figure 3: Energy level structure of erbium and dysprosium with the relevant cooling transitions marked. Figure taken from [11].

frequency. The dipole moment and the electric field interact dispersively and from performing a time average we can gather a dipole potential where the minimum can be used for trapping and a corresponding dipole force can be derived from it depending foremost on the intensity distribution of the laser beam and the polarizability. ODTs typically reach trap depths smaller than a millikelvin. Due to the detuning far outside the natural linewidth of a transition, optical scattering is negligible.

In the following chapter we will take a closer look at the trapping mechanism of ODTs, show which parameters are of essential importance and also investigate what role different trap shapes play. In order to understand the atom light interaction in an ODT, we will look at a two level system. We assume our neutral atom has a ground state  $|g\rangle$  and an excited state  $|e\rangle$ . They are eigenstates of the bare atomic Hamiltonian  $H_0$  and the transition energy between them will be written as  $\hbar\omega_0$ . On the other hand we have a light beam with frequency  $\omega_L/2\pi$  propagating in  $x$  direction. The corresponding electric field can be written as  $\vec{E} = \vec{E}_0 \cos(\omega_L t - k_L x)$  where we assume linearly polarized light  $\vec{E}_0 = E_0 \hat{e}_p$  with  $\hat{e}_p$  in the polarization direction and  $k_L$  the wave number corresponding to  $k_L = \omega_L/c$ ,  $c$  being the speed of light. This electric field displaces the positive and negative charges within the atom and thus induces a dipole moment  $\vec{d}$  that is proportional to  $\vec{E}$

$$\vec{d} = \alpha \vec{E} \quad (3.7)$$

where  $\alpha$  is the polarizability of the atom. According to perturbation theory, the dipole moment induced by the electric field in turn induces a tiny shift of the ground and excited state energy levels of the atom. From 3.7 we can immediately gather that in an electric field with a spatially varying amplitude, a shift in the energy level will create a potential landscape that can confine atoms. The shift in energy level is called the AC-Stark shift or also light shift and it has a similar effect as the Zeeman-shift in magnetic fields. We will investigate it a little further, since the exact form the AC-Stark shift takes will vary depending in which regime we operate our trap and what kind of atom species.

Assuming our electric field is uniform over the size of an atom we can write the dispersive coupling of the induced dipole with the electric field as an interaction Hamiltonian on top of our bare Hamiltonian treating it as a perturbation.

$$H_{int} = -\vec{d} \vec{E} \quad (3.8)$$

$$H = H_0 + H_{int} \quad (3.9)$$

We can write the dipole moment as  $\vec{d} = e\vec{r}$ . This means it is of odd parity as it will transform to  $-\vec{d}$  under inversion  $\vec{r} \rightarrow -\vec{r}$ . If we want to calculate the matrix element corresponding to the dipolar coupling between states we will find that

$$\langle e | \vec{d} | e \rangle = \langle g | \vec{d} | g \rangle = 0 \quad (3.10)$$

because these diagonal matrix elements will always have odd parity and thus yield zero when one integrates over the whole space.

In an appropriate setting where the laser frequency  $\omega_L$  is not relatively close to the resonance frequency  $\omega_0$ , we can gather that  $\omega_L + \omega_0 \gg \omega_L - \omega_0 = \delta$  with  $\delta$  the detuning, allowing us to perform the so-called rotating wave approximation which eliminates terms which are oscillating rapidly over the timescale during which the atom interacts with the light wave and thus yield zero. In this approximation we may write the full Hamiltonian in a very much simplified matrix form:

$$\hat{H} = \frac{\hbar}{2} \begin{bmatrix} 0 & \Omega \\ \Omega & -2\delta \end{bmatrix} \quad (3.11)$$

In the off-diagonal elements we have the Rabi frequency

$$\Omega = \frac{E_0}{\hbar} \langle e | \hat{d} \hat{e}_p | g \rangle \quad (3.12)$$

It describes the coupling strength between the ground and excited state when the two-level system is driven by an external field. It also quantifies the rate of population oscillation between the states. Note that  $\Omega$  is proportional to the electric field amplitude and thus  $\Omega^2 \propto I$ . The calculation of the eigenvalues is straightforward and gives us the energy shifts due to the Stark-effect in this approximation:

$$E_+ = \frac{\hbar}{2}(-\delta + \sqrt{\Omega^2 + \delta^2}); E_- = \frac{\hbar}{2}(-\delta - \sqrt{\Omega^2 + \delta^2}) \quad (3.13)$$

Now if we go further away from the resonance, the detuning  $\delta$  will grow larger and larger. Eventually we can say  $\Omega \ll |\delta|$  and perform an expansion in the square root. We find then that each state is shifted by

$$\Delta E_{eg} = \pm \frac{\hbar\Omega^2}{4\delta} \quad (3.14)$$

The energies in ground and excited state are shifted in opposite directions. Which energy level is shifted up or down is however determined by the sign of the detuning. For a positive, or red detuning, so a laser frequency higher than the resonance frequency, the ground state will be shifted to lower and the excited state to higher energy and the other way around for negative, or blue detuning. As mentioned before in an ODT light scattering is negligible. Thus it is safe to assume, that the overwhelming majority of atoms in our system are populating the ground state. Therefore in the case of red detuning atoms will be attracted to high intensity light as the energy shift is favourable. Blue detuned light on the other hand will repel atoms as they seek low intensity regions due to a positive shift in the ground state energy.

We have established the AC-Stark shift or light shift as the basic mechanism behind the optical dipole trap. In order to quantify more precisely the magnitude of the shift which corresponds to our trap depth we need to investigate how susceptible our atom is to an electric field inducing a charge displacement. Specifically we need to determine the polarizability of the atom. To do this we need to go beyond the rotating wave approximation.

We can employ the Lorentz oscillator model[26]. An electron point charge is bound to the core of an atom with  $\omega_0$  the eigenfrequency, analogue to the resonance frequency. The system is driven with the laser frequency  $\omega_L$  and damped through radiative losses of energy, which scale with the natural linewidth  $\Gamma$ . We can write the differential equation for the displacement of the electron:

$$\ddot{x} + \left(\frac{\omega_L}{\omega_0}\right)^2 \Gamma \dot{x} + \omega_0^2 x = -\frac{eE_0 e^{-i\omega_L t}}{m_e} \quad (3.15)$$

The stationary solution reads:

$$x(t) = -\frac{e}{m_e} \frac{1}{\omega_0^2 - \omega_L^2 - i\frac{\omega_L^3}{\omega_0^2}\Gamma} E_0 e^{-i\omega_L t} \quad (3.16)$$

The dipole moment in general is defined as some charge displacement  $\vec{d} = -e\vec{x}$ . Together with 3.7 we can quickly gather an expression for the polarizability and determine its real and imaginary parts:

$$\text{Re}(\alpha) = \frac{e^2}{m_e} \frac{(\omega_0^2 - \omega_L^2)}{(\omega_0^2 - \omega_L^2)^2 + \left(\frac{\omega_L^3}{\omega_0^2}\Gamma\right)^2} \quad (3.17)$$

$$\text{Im}(\alpha) = \frac{e^2}{m_e} \frac{\left(\frac{\omega_L^3}{\omega_0^2}\Gamma\right)}{(\omega_0^2 - \omega_L^2)^2 + \left(\frac{\omega_L^3}{\omega_0^2}\Gamma\right)^2} \quad (3.18)$$

The two parts of the complex polarizability are related to different effects. The real part describes to the in-phase component of the dipolar oscillation. The dipolar interaction potential is proportional to the real part and the gradient of the interaction potential corresponds to the conservative force responsible for trapping atoms in the ODT. The imaginary part describes the out-of-phase or quadrature component of the dipole oscillation. The power that is absorbed from the driving field through the oscillator is proportional to the imaginary part. As the power can be considered as a stream of photons, this can be interpreted as a cycle of absorption and spontaneous emission corresponding to light scattering [26]. The dipole potential and the scattering rate can be written in the following way:

$$U_{dip} = -\frac{1}{2} \langle \vec{d} \vec{E} \rangle = -\frac{1}{2\epsilon_0 c} \text{Re}(\alpha) I \quad (3.19)$$

$$\Gamma_{sc} = \frac{\langle \vec{d} \vec{E} \rangle}{\hbar\omega_L} = \frac{1}{\hbar\epsilon_0 c} \text{Im}(\alpha) I \quad (3.20)$$

In both cases we took the time average and used 3.7. We can formulate both the conservative and the dissipative part of the interaction in terms of the polarizability.

Note that  $\Gamma$  the natural linewidth corresponds to the on-resonance damping or scattering rate, while  $\Gamma_{sc}$  from 3.20 corresponds to the scattering rate to the spatially varying scattering rate to be expected from the layout of our trap. Note also that the exact form of  $\Gamma$  can vary depending on the approach. The classical damping rate due to radiative energy loss can be written according to Larmor's formula:

$$\Gamma = \frac{e^2 \omega_0^2}{6\pi\epsilon_0 m_e c^3} \quad (3.21)$$

However if we stick to a semiclassical approach where we consider the two-level system, the damping rate will depend on the dipole matrix element between the two states:

$$\Gamma = \frac{\omega_0^3}{3\pi\epsilon_0 \hbar c^3} |\langle e | \hat{d} | g \rangle|^2 \quad (3.22)$$

Depending on what atoms and thus what exact transitions are used in the trap, 3.21 and 3.22 can agree very well, especially in the case of alkali atoms. But in the case of dipolar lanthanides, the determination of the matrix element can yield very different results. In fact our discussion so far always revolved around isotropic atoms where the oscillating dipole will be induced parallel to the driving field. Ultimately though, we are dealing with dysprosium, a dipolar lanthanide, which in its ground and excited state of the transition we are using has a non-zero orbital momentum and can therefore be considered anisotropic. In this case dipole components perpendicular to the incoming light can also be induced. The anisotropic polarizability becomes a 3x3 tensor with scalar, vectorial and tensorial components. Consequently both the dipole potential and the scattering rate can be decomposed into a sum of the scalar vectorial and tensorial contributions  $U_{dip} = U_s + U_v + U_t$  ( $\Gamma_{sc} = \Gamma_s + \Gamma_v + \Gamma_t$ ) (see also [5]). The contributions of the vectorial and tensorial components depend on the angular momentum quantum number  $J$  of the ground state and its projection  $m_J$  on the quantization axis. The quantization axis is usually set by an external magnetic field. The angles between quantization and propagation axis  $\theta_k$  as well as polarization axis  $\theta_p$  will also determine the amplitude of the contribution[3][41].

$$\alpha_{tot}(\omega_L) = \alpha_s(\omega_L) + |\hat{e}_p^* \times \hat{e}_p| \cos \theta_k \frac{m_J}{2J} \alpha_v(\omega_L) + \frac{3m_J^2 - J(J+1)}{J(2J+1)} \frac{3 \cos^2 \theta_p - 1}{2} \alpha_t(\omega_L) \quad (3.23)$$

The respective real and imaginary parts can be inserted in 3.19 and 3.20 to get the anisotropic optical dipole potential and scattering rate. As already pointed out above the individual components themselves depend on the off-diagonal matrix element  $|\langle e | \hat{d} | g \rangle|$ . We can make a few observations regarding 3.23. In the case of linear polarization, regardless of the layout of polarization and quantization axis,  $\hat{e}_p$  will be real and  $|\hat{e}_p^* \times \hat{e}_p|$  a cross product of two identical vectors which yields zero. Thus there is no vectorial contribution if the driving light field is linearly polarized. The tensorial contribution will vanish if  $J = 1/2$ . This condition is always fulfilled in the case of alkali atoms and reveals an important difference between alkalis like Li, K or Rb and magnetic lanthanides like Er and Dy. As a reminder, in the ground state of Dy we are dealing with  $J = 8$ . Furthermore the total polarizability for erbium and dysprosium is influenced by every single transition, which are many, as we saw in Figure 3. We have to sum over all of the lines in order to calculate the anisotropic polarizability.

### 3.3 Trap shaping

Typically in experiments, optical dipole traps are built using laser beams with a circular or elliptical Gaussian intensity profile. The shape and size of such Gaussian beams can be easily manipulated with standard optical components. In the case of our optical dipole trap, two red-detuned Gaussian beams are overlapped at their waists. This creates a harmonic trap region in which the atoms are captured. The harmonic trap consists as the name suggests of soft-walled potential inhomogeneous potential. The nature of the confined many-body system depends on the interactions of the atoms among each other and with the potential. Thus a harmonic trap with an inhomogeneous potential depth would inevitably lead to inhomogeneous densities within the atomic cloud. The natural and intuitive way to create a homogeneous quantum gas is therefore to try to confine the system in a homogeneous trap geometry such as a box potential. Ideal box traps consist of a flat potential leading to uniform densities and homogenous interaction strength within the atomic system which in turn leads to an enhanced role of quantum fluctuations. This often proves to be useful for a number of reasons. With the density also the local interaction strength becomes more uniform offering more precise global control when varying interaction parameters, which is cru-

cial for experiments investigating homogeneous phase-transitions. Box traps can also more closely resemble conditions which are assumed in many theoretical models and can do so without the need for local density approximation (LDA). This makes a comparison between theoretical and experimental results simpler. Ultimately uniform density distributions within box traps may also improve the signal-to-noise (SNR) ratio for some experiments as all parts of the gas contribute the same amount of signal, other than in harmonic traps where low density regions may contribute less, effectively lowering the SNR. It should however not go unmentioned that once more the peculiarity of dysprosium comes into play when it comes to the ideal trap shape. Other than in a gas where the internal interactions are mostly contact interactions, a dipolar gas with long range interactions requires box potentials with soft walls to become homogeneous. In [35], different grades of wall softness were tested. A power law potential can be defined as:

$$U_{dip}(r, z) = \frac{1}{2} \left( \left( \frac{r}{\gamma} \right)^p + z^2 \right) \quad (3.24)$$

, with  $\gamma$  the aspect ratio of the trap. The ideal parameter  $p^*$  determining the softness of the walls for a homogeneous dipolar gas depends on  $\gamma$  and the chemical potential  $\mu$ :

$$p^* = \frac{\log \mu}{W_0 \left( \frac{\log \mu}{2S^* \gamma} \right)} \quad (3.25)$$

Here  $W_0$  is the Lambert W function and  $S^*$  an empirically determined constant related to the wall steepness.

There are various ways in which box traps can and have been created in 3D [22], 2D [10] and also 1D systems [57] [46]. In the case of repulsive traps, one can often work with hollow laser beams and add two end caps, confining the system in a cylindrical 3D trap. By adjusting the position of the end caps towards each other one can also make this system quasi 2D. For the 1D case one would have to confine movement in two directions, which has also been accomplished on atom chips. The case of attractive potentials can be somewhat more demanding as one needs to shape and cancel out intensity variations on a high-intensity laser beam in order to achieve the desired trap uniformity.

The methods of choice to manipulate laser beams into the various shapes described above are programmable spatial light modulators (SLMs). More specifically in most cases either a liquid crystal SLM, or a digital micromirror device (DMD) will be used. An acousto-optic deflector (AOD) or an acousto-optic modulator (AOM) can also be considered a spatial light modulator and are widely used tools in atomic physics, although generally they are not aimed at creating pixelated phase or intensity patterns, but mainly at beam steering or frequency modulation through the interaction between sound and light waves. This through time averaging is seen by the atoms as a smooth, dynamically controllable potential landscape.

A liquid crystal SLM consists of an array of pixel whose refractive index can be individually controlled. When light shines through or reflects off one of those pixels, its phase will be modulated. Although these phase shifts do not directly affect the amplitude, the intensity pattern can indirectly be altered through interference or by using the Fourier relation through which a phase modulation in real space corresponds to an amplitude and phase modulation in Fourier space (see also 4.1). The DMD on the other hand consists of an array of micromirrors which can be individually turned 'off' or 'on' thus directly modulating the light amplitude. DMDs are therefore more convenient to create box potentials of an arbitrary shape for 2D or 3D traps. Another perk of DMDs is the fast switching rate between patterns enabling dynamic changes of intensity profiles during an

experimental sequence.

Apart from creating uniform box potentials, two more applications of a DMD should also be highlighted here briefly. Although a DMD as mentioned modulates the amplitude of an incoming laser beam, it is also possible to imprint a spatially varying phase on the atomic cloud [14]. The atoms which are exposed to the light and experience a Stark shift  $U_{dip}$  also acquire a phase since the effective energy  $E_{eff}$  of the atomic state is modified and the time dependence of their wavefunction  $\psi(t)$  is related to it ( $\psi(t) = e^{iE_{eff}t}\psi(0)$ ). If the light pulse on the atoms is sufficiently short, the imprinted phase can be written as [15]:

$$\phi(x, y) = \frac{U_{dip}(x, y)T_{pulse}}{\hbar} \quad (3.26)$$

Here  $\phi$  is the phase and  $T_{pulse}$  the time for which the atoms are exposed to light. Now for a spatially varying potential it is clear that the imprinted phase will also be spatially varying and even though we want to focus on box potentials, a DMD can in the same way also produce spatially varying intensity patterns. This method has been experimentally tested and used to create vortices by imprinting a full phase rotation[14].

The second method involves the fast switching abilities of a DMD. By dynamically switching through different patterns one can rapidly alter the shape or position of the beam and thus like in a stop-motion movie have the light potential move through the atomic cloud. With this method one can create two opposing localized vortices [52] or all sorts of other defects for that matter. Typically this stirring method is employed with blue-detuned light pushing the atoms around, but can in principal in the same way be implemented for red-detuned light. This method is an application of the DMD we might want to explore later on 8.

### 3.4 Polarizability calculations

It seems rather intuitive that for a blue-detuned trap it is easier to create flat potentials. One would simply have to create a repulsive boundary out of light while the actual trapping region can be left a dark and typically flat background. If the trap is red-detuned, the light beam creating the potential has to be shaped into a flat top intensity distribution somehow. The upside to red-detuned traps is that traps can be operated at wavelengths very far from transition and easily available through commercial light sources. Furthermore the farther from a transition, the less variation there is in the total polarizability, meaning also light sources with a slightly larger bandwidth can be used to create the trapping potential. In our case we decided to build a red-detuned trap as a blue-detuned trap is especially challenging in the case of dysprosium. As mentioned before to calculate the anisotropic polarizability we need to sum over the contributions from all lines. Yet the polarizability is mainly dominated by the broad transition at 421 nm. This means above this transition the polarizability is positive most of the time as can be seen in Figure 4. We would need to go below the transition or very close to one of the narrow transitions above it. Although since a blue detuned trap might be an option in the future, we will investigate the behaviour of the polarizability of our atoms under blue-detuned light.

As mentioned in section 3.4, in the case of dipolar atoms with a large magnetic moment the polarizability which is ultimately determining our trap depth consists of three components, the scalar, vectorial and tensorial component. In this chapter we will show the results of some calculations conducted in order to estimate the real and imaginary parts of the  $\alpha_{tot}$ , the contributions of the individual components with a focus on the blue-detuned regions near the 530 nm and 684 nm transitions of dysprosium. The aim of our calculations is to find a light configuration near the

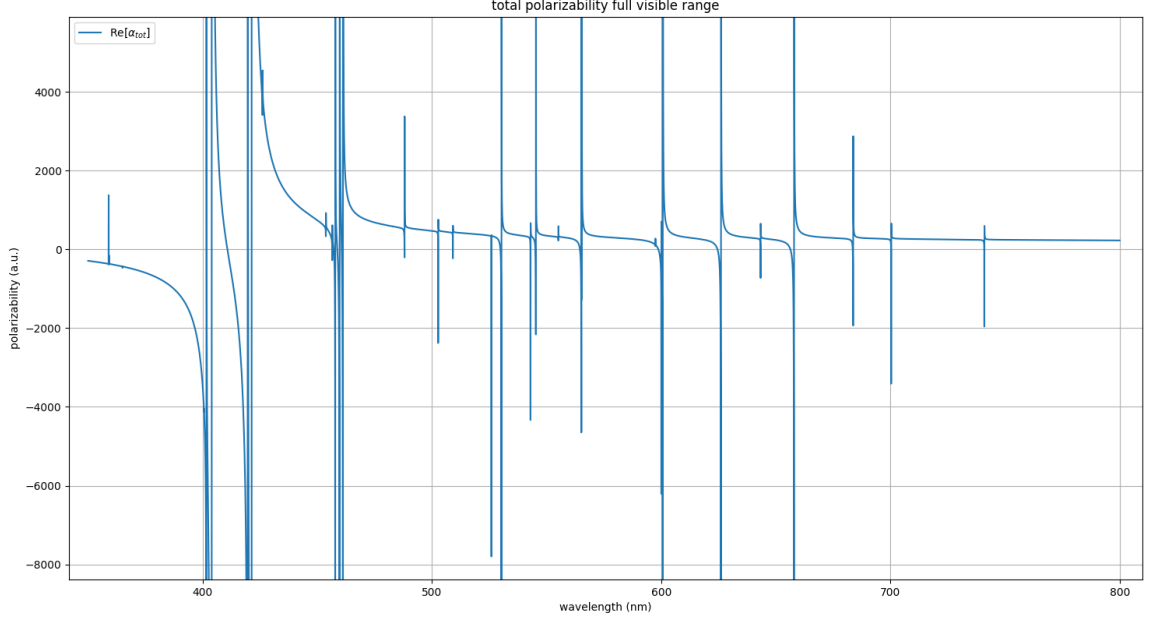


Figure 4: Total polarizability over the full range of the visible spectrum. We can observe many transitions. As expected for most wavelengths above 420 nm the polarizability is positive.

transitions which is suitable for repulsive trapping and there is no dependence on the orientation of the dipoles.

We calculate real and imaginary parts of the polarizability according to [41]. We write the different components of the polarizability as  $\alpha_k(\omega_L)$  with  $k = [0, 1, 2]$  corresponding to the rank of the irreducible tensor. In the context of optical dipole trapping, we consider laser frequencies far from the optical resonance. We can separate real and imaginary parts and can write the polarizability components as a sum over all states.

$$\begin{aligned} \text{Re}(\alpha_k(\omega_L)) &= 2\sqrt{2k+1} \sum_{\beta', J'} (-1)^{J+J'} \begin{Bmatrix} 1 & 1 & k \\ J & J & J' \end{Bmatrix} |\langle \beta' J' | \mathbf{d} | \beta J \rangle|^2 \\ &\quad \times \frac{(E_{\beta' J'} - E_{\beta J}) \delta_{(-1)^k, 1} - \hbar\omega_L \delta_{(-1)^k, -1}}{(E_{\beta' J'} - E_{\beta J})^2 - \hbar^2\omega_L^2} \end{aligned} \quad (3.27)$$

$$\begin{aligned} \text{Im}(\alpha_k(\omega_L)) &= \sqrt{2k+1} \sum_{\beta', J'} (-1)^{J+J'} \begin{Bmatrix} 1 & 1 & k \\ J & J & J' \end{Bmatrix} \hbar\gamma_{\beta' J'} |\langle \beta' J' | \mathbf{d} | \beta J \rangle|^2 \\ &\quad \times \frac{[(E_{\beta' J'} - E_{\beta J})^2 - \hbar^2\omega_L^2] \delta_{(-1)^k, 1} - 2\hbar\omega_L (E_{\beta' J'} - E_{\beta J}) \delta_{(-1)^k, -1}}{[(E_{\beta' J'} - E_{\beta J})^2 - \hbar^2\omega_L^2]^2} \end{aligned} \quad (3.28)$$

Here  $|\beta, J\rangle$  and  $|\beta', J'\rangle$  indicate our ground and excited state quantum numbers respectively with  $E_{\beta J}$  and  $E_{\beta' J'}$  their eigenenergies. The expressions in the curly brackets are the Wigner 6-j symbols and  $\gamma_{\beta' J'}$  is the natural linewidth of the transition. We can write the transition dipole moment as:

$$|\langle \beta' J' | \mathbf{d} | \beta J \rangle|^2 = \frac{3\pi\epsilon_0 \hbar^4 c^3 (2J' + 1) \gamma_{\beta' J'}}{(E_{\beta' J'} - E_{\beta J})^3} \quad (3.29)$$

With  $\epsilon_0$  the vacuum permittivity and  $c$  the speed of light. Note that we still need to sum over all transitions.

### 3.4.1 530 nm transition

With all necessary formulas now at hand we can investigate the total polarizability near the 530 nm transition of dysprosium. This transition goes from the lower  $4f^{10}6s^2$  ( $J=8$ ) level to the higher  $4f^9 5d6s^2$  ( $J=7$ ) level. In vacuum the transition wavelength is 530.306 nm and it has a natural linewidth of 850 kHz. We assume for now light linearly polarized in  $x$  direction and propagating in  $z$  direction while the dipoles of our atoms lie in the  $yz$ -plane. They can be tilted through an external magnetic field. In Figure 5 we can observe the behaviour of the different polarizability components for the case of light linearly polarized in  $x$  direction and the total polarizability for light linearly polarized in  $y$  direction with tilted dipoles. As mentioned above, the vectorial component of the polarizability enters with a prefactor including the cross product of the unit vector of the polarization axis and its complex conjugate, however in the case of linear polarization, there is no complex part to the unit vector, thus its identical to its complex conjugate, thus the cross product yields zero and there is no contribution from the vectorial component in the case of linearly polarized light. We will see later that it does enter for circularly polarized light. The tensorial contribution does enter, note, that since the angle between polarization axis and quantization axis of the atoms  $\theta_p$  is always  $90^\circ$  in this case, no matter how we tilt the dipoles in the  $yz$ -plane, the tensorial polarizability will enter with a small negative prefactor as  $\frac{3 \cos^2 \theta_p - 1}{2} = -\frac{1}{2}$ . This is not the case if the light is polarized in  $y$  direction. As we tilt the dipoles away from a  $90^\circ$  angle with the polarization axis towards a parallel or antiparallel layout (both cases yield the same result due to the symmetry of the  $\cos^2$  term), we observe a shift in polarizability. We do not want the polarizability to depend on the orientation of the dipoles hence this configuration is not a favourable choice. From Figure 5 we can make out that to build a blue-detuned trap we

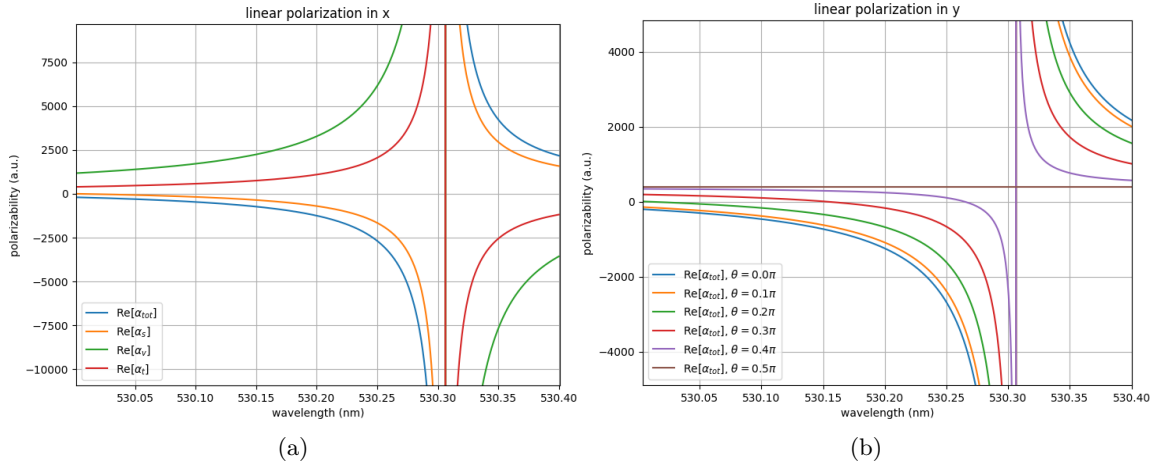


Figure 5: (a) Different components and total weighted polarizability for the case of light linearly polarized in  $x$  direction. (b) Total polarizability for different angles between polarization and quantization axis in the case of light linearly polarized in  $y$  direction.

are interested in linear polarization in  $x$  direction and probably limited to some region between about 530 nm and 530.25 nm. Going too close to the transition may cause large fluctuations in trap depth and light scattering as the total polarizability diverges towards negative infinity. In terms of detuning  $\Delta\omega$  this corresponds to something between 2000 and 500 GHz detuning. Note that here we have adapted the convention that blue-detuned light corresponds to positive detuning while red-detuned light corresponds to negative detuning, even though this means the smaller the wavelength the larger the detuning.

Next we take a closer look at the behaviour of  $\alpha_{tot}$  in the above specified region and try to quantify

the variation we can expect if we manage to lock the wavelength of the laser within a 100 MHz wide region. We also evaluate the lifetime we have to expect if limited by light scattering, although in the case of a blue-detuned trap we will not hopefully have to worry about this too much as atoms will be confined in the low-intensity regions of the trap.

To track the variation, we define a 100 MHz wide box around each grid point and check what other grid points lie within this region. We identify the mean, maximum and minimum value of the polarizability inside the box and calculate  $\frac{|\alpha_{max} - \alpha_{min}|}{|\bar{\alpha}|} = \frac{\delta\alpha}{\bar{\alpha}}$ . The result, shown in Figure 6 (a) was somewhat puzzling at first, since even though the variation quickly decreased as it got further away from the transition, it exhibited a minimum at around 530.07 nm (1570 GHz detuning). This would point towards a saddle point in the total polarizability curve, though one should only appear at much lower wavelength. Likely it is just the case here, that the decrease of  $|\bar{\alpha}|$  at this point overtakes the decrease of  $\delta\alpha$ . We thus also quickly plotted the bare  $\delta\alpha$  which as expected did not show a minimum (see also 6 (a)).

The lifetime  $\tau$  of the atoms is inversely related to the scattering rate  $\Gamma_{sc}$ . With our results from 3.2, specifically 3.19 and 3.20 we can rewrite this relationship in terms of the real and imaginary polarizability and the potential depth  $U_{dip}$ .

$$\tau = \frac{1}{\Gamma_{sc}} = \frac{\hbar}{2U} \frac{|\text{Re}(\alpha_{tot}(\omega_L))|}{\text{Im}(\alpha_{tot}(\omega_L))} \quad (3.30)$$

With  $U$ , a given trap depth. We evaluated the lifetime for trap depths between 100 and

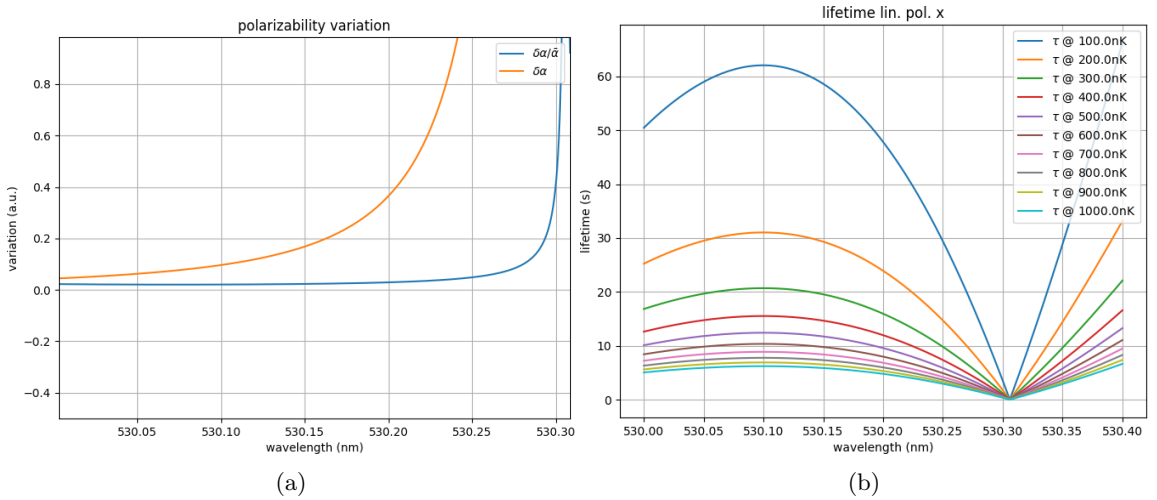


Figure 6: (a) The normalized and the absolute variation of the total polarizability to the left of the 530 nm transition. (b) The lifetime of an atom due to light scattering for the case of trap depths ranging from 100 nK to 1000 nK for the case of light linearly polarized in  $x$  direction.

1000 nK  $\times k_B$  (see Figure 6 (b)). The smaller the imaginary part of the polarizability the longer the lifetime would be, however as the real part of the polarizability would also eventually approach zero from below a larger intensity is required for the same trap depth thus effectively lowering the lifetime according to 3.30, our calculation of the lifetime should thus point us towards a detuning where  $\tau$  is maximized. And indeed we could observe how the lifetime assumed a similar shape as an inverse parabola with a zero crossing at the transition as well as at the wavelength where  $\text{Re}(\alpha_{tot}(\omega_L))$  becomes positive. The maximum lifetime for all trap depths could be achieved for 530.10 nm wavelength (1380 GHz detuning) and varies between 7 and about 63 seconds depending on the specific trap depth. The variation of the total polarizability in this region is very small, in fact less than 0.1 a.u. within a region of 100 MHz. We are confident, that we will be able to employ

a locking scheme producing less frequency noise than that also without a high finesse cavity. The absolute total polarizability at 1380 GHz detuning is around -460 a.u., which is comparable with what we are working with at 532 nm (450 a.u.). Another upside of our designated wavelength being very similar to 532 nm with which we are already working is that we can expect the same behaviour in an optical setup (see also [27]). Overall this choice seems promising for repulsive trapping of dysprosium.

### 3.4.2 684 nm transition

We can investigate the same things for the transition near 684 nm in dysprosium. This transition line goes from the  $4f^{10}6s^2$  ( $J=8$ ) level to the  $4f^95d6s^2$  ( $J=8$ ) level. It sits at 683.732 nm and has a natural linewidth of 95 kHz [54].

Also for this transition we can calculate the anisotropic polarizability in the same way we did before. The plots in Figure 7 are identical with those produced for the 530 nm transition above. However, since  $J$  is the same in both levels of the transition, the tensorial component of the

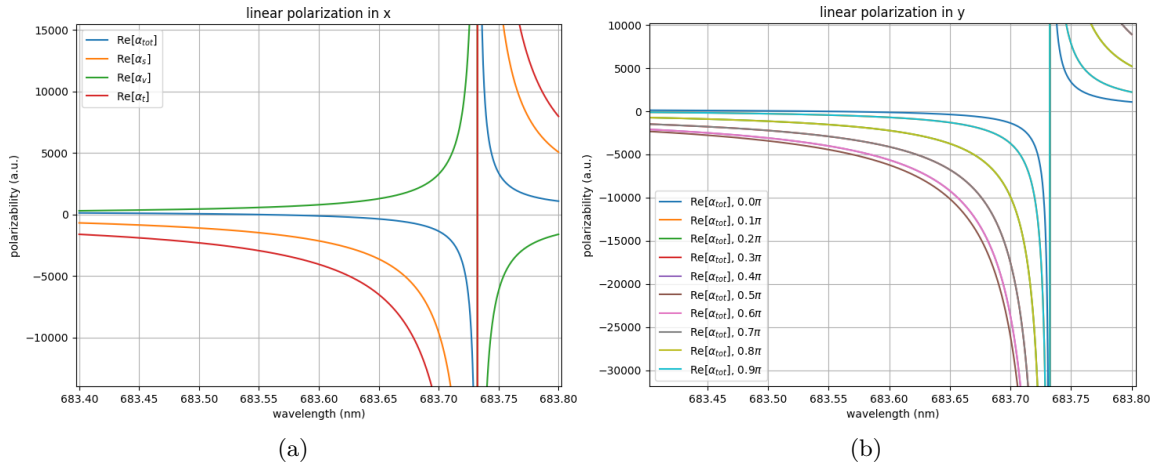


Figure 7: (a) Different components and total weighted polarizability for the case of light linearly polarized in  $x$  direction. (b) Total polarizability for different angles between polarization and quantization axis in the case of light linearly polarized in  $y$  direction.

polarizability is now negative to the left of the transition and thus reduces the absolute value of the total polarizability. The total polarizability therefore approaches zero considerably faster than in the previous case, meaning that we expect to find a good wavelength for repulsive trapping at much smaller detuning.

We once again tried to evaluate where such a good wavelength may be located, however this time we did not pay too much attention to the variation in the total polarizability as it was likely small and exhibited no clear minimum. Instead, we directly evaluated the wavelength with maximum lifetime in the case of linearly polarized light in  $x$  direction. The results can be seen in Figure 8 (a). As before, for all trap depths between 100 nK and 1  $\mu$ K, the maximum lifetime lies at the same position, namely 683.639 nm, corresponding to a detuning of 376 GHz. As expected the detuning is much smaller than in the case of the 530 nm transition. What we observe additionally however is that the absolute lifetime is much smaller than previously. In fact for trap depths of more than 200 nK, the lifetime sinks below 10 s. However, we also conducted some tests on the lifetime for linearly polarized light in  $y$  direction (see Figure 8 (b)) and could observe that even the lifetime at 1  $\mu$ K increases to above 30 s in the case of  $\theta_p = \pi/2$ , so dipoles oriented in the  $xy$  plane. This however in the case of our 2D gas would go in hand with attractive dipole-dipole interactions and

thus likely lead to a collapse of our system.

To sum up, in the case of the 684 nm transition, the ideal wavelength we found for repulsive

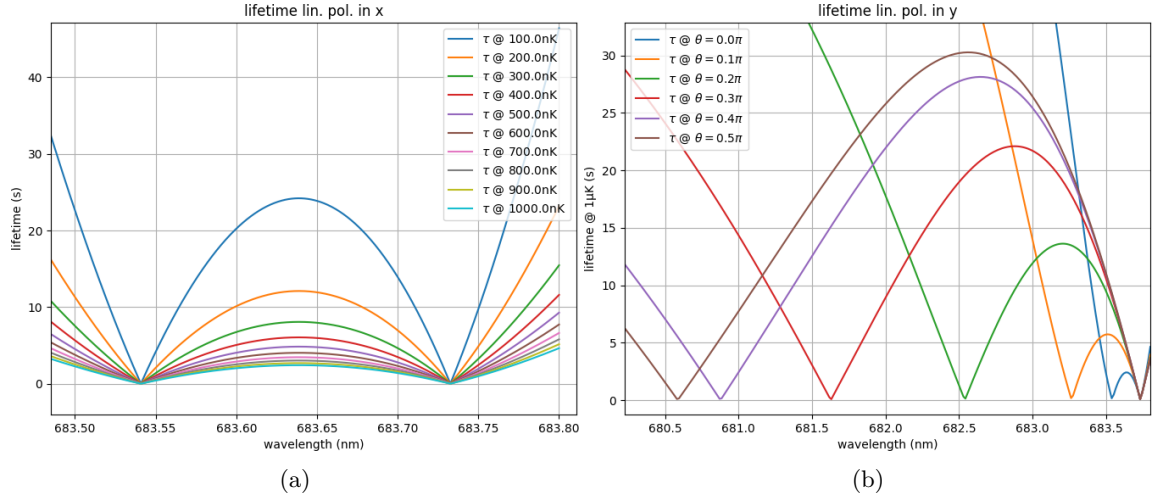


Figure 8: (a) Lifetime in the case of light linearly polarized in  $x$  direction for different trap depths. (b) Lifetime in the case of light linearly polarized in  $y$  direction for different angles between polarization and quantization axis.

trapping sits at 376 GHz detuning. The total polarizability at this position is -293 a.u. and varies by less than 0.2 a.u. within a 100 MHz wide region.

It remains to be seen whether either or both of the transitions are suitable to be employed for repulsive trapping in our setup. For now we will concentrate on an attractive trap at 532 nm, amplitude modulated through a DMD. Lasers at 532 nm are easily commercially available, also with very high power. Matching the power in order to achieve the same trap depth may be challenging and expensive with a custom wavelength laser. If the power can not be matched, the detuning would have to be reduced, to increase the polarizability, introducing larger trap depth variations. What may furthermore reduce the amount of net power available in a repulsive setup is, that when amplitude modulating the beam with a DMD one would dump the centre and highest intensity parts of a beam to create a hollow light cone in which atoms can be repulsively trapped. To counteract this however it is possible to invert the Gaussian beam profile with an optical setup including an axicon lens, such that the high intensity parts of the beam already lie on the outside. With the axicon lens it is possible to directly create a hollow beam for repulsive trapping, or to modulate the inverted Gaussian intensity distribution further with a DMD without dumping an unreasonable amount of power [44][43].

Overall we can conclude though, that the transition near 530 nm is certainly the more suitable choice to employ a repulsive trapping setup. A corresponding laser source has been acquired.

## 4 Beam shaping optics

This chapter is supposed to give an overview over the optical principles and phenomena which we employ or which emerge when we try to produce an arbitrarily shaped laser beam. In particular we go over optical Fourier transforms (4.1) as they play a vital role in our optical setup, before moving on towards topics more specifically linked to light amplitude modulation with a DMD (4.3) such as greyscaling (4.3.2) and dithering (4.3.3).

### 4.1 Fourier optics

Fourier optics enables us to describe light waves propagating through free space either in the real-space domain or the frequency domain. We may look at any arbitrary function depending on real space coordinates as a superposition of harmonic functions depending on the spatial frequency coordinates and vice-versa. The Fourier transform, also sometimes called harmonic analysis enables us to switch seamlessly between real-space and frequency domain. In the following we will introduce the optical Fourier transform and explain how it emerges naturally in many imaging systems. We do this to get a good understanding of the imaging process and of phenomena such as greyscaling or ringing which are linked to Fourier optics. The following sections are based on [51].

#### 4.1.1 Light propagation in free space

We assume the complex amplitude of a laser beam of a fixed wavelength  $\lambda$  in the  $z = 0$  plane perpendicular to the optical axis can be described by an input function  $g_{in}(x, y) = U(x, y, z = 0)$  with  $U(x, y, z)$  the electric field amplitude. Fourier optics allows us to describe the propagation of the light wave in space by making use of harmonic decomposition. In particular, we can compute the resulting wave amplitude  $g_{out}(x, y) = U(x, y, z = d)$  after propagation over a distance  $d$  in free space. For a harmonic function, like a plane wave as our input, we can write  $g_{in}(x, y) = A \exp[-i2\pi(\nu_x x + \nu_y y)]$  with the spatial frequency  $\nu_{x,y}$  in  $x$  and  $y$  direction respectively. Our output function after propagation over a distance  $d$  is then subsequently  $g_{out}(x, y) = A \exp\left[-i2\pi(\nu_x x + \nu_y y + \frac{k_z(\nu_x, \nu_y)}{2\pi}d)\right]$  with  $k_z = 2\pi\sqrt{\lambda^{-2} - \nu_x^2 - \nu_y^2}$ . The propagation corresponds to a transfer function  $H(\nu_x, \nu_y)$  between the two:

$$H(\nu_x, \nu_y) = g_{out}(x, y)/g_{in}(x, y) = \exp(-i2\pi d\sqrt{\lambda^{-2} - \nu_x^2 - \nu_y^2}) \quad (4.31)$$

It is here where we can make a first important approximation. For a harmonic wave whose wavevector has a small angle  $\theta$  with the  $z$ -axis, the transverse spatial frequency  $\nu_{x,y}$  is related to  $\theta$  via  $\nu_{x,y} = \frac{k_{x,y} \sin \theta}{2\pi}$ . If we assume now nearly paraxial rays, we can simply write  $\theta^2 = \theta_x^2 + \theta_y^2 \approx \lambda^2(\nu_x^2 + \nu_y^2)$ . Therefore the phase factor in 4.31 can be written as:

$$2\pi \frac{d}{\lambda} \sqrt{1 - \theta^2} = 2\pi \frac{d}{\lambda} \left(1 - \frac{\theta^2}{2} + \frac{\theta^4}{8} - \dots\right) \quad (4.32)$$

Here we once more assumed small angles and expanded the square root. If we plug this in 4.31, neglecting all higher than quadratic terms, we get:

$$H(\nu_x, \nu_y) \approx H_0 \exp[i\pi \lambda d(\nu_x^2 + \nu_y^2)] \quad (4.33)$$

with  $H_0 = \exp(-ikd)$ . This approximation of the transfer function, where we only leave terms quadratic in  $\nu$  is known as the Fresnel approximation. We will later employ the results of the Fresnel approximation to derive the optical Fourier transform with a thin lens.

The condition for the Fresnel approximation to be valid is that the angle  $\theta$  is small enough that the third term in 4.32 is much smaller than one. If we say the farthest outlying point in the output plane has a distance  $a$  from the centre, we can write the largest possible angle as  $\theta_{max} \approx a/d$  and the condition of validity becomes:

$$N_F \frac{\theta_{max}^2}{4} \ll 1 \quad (4.34)$$

Here we also already defined the so called Fresnel number:

$$N_F = \frac{a^2}{\lambda d} \quad (4.35)$$

Note, we will also use the Fresnel number for the input plane and write it as  $N'_F = \frac{b^2}{\lambda d}$  with  $b$  the radius of an area to which  $g_{in}(x, y)$  is confined. Once we have determined that the Fresnel approximation is valid in our case, we can finally evaluate  $g_{out}(x, y)$ . To do so we can either work in the spatial frequency domain where we would use 4.33, multiply it with the Fourier transform of our input function and transform everything back to real space. Or we can work in the real space domain from the beginning. For this we need the inverse Fourier transform of 4.33, the so called impulse response function

$$h(x, y) \approx h_0 \exp \left[ -ik \frac{x^2 + y^2}{2d} \right] \quad (4.36)$$

with  $h_0 = (i/\lambda d) \exp(-ikd)$ . The complex amplitude at a point  $(x, y)$  in the output plane will be a convolution our input function  $g_{in}(x, y)$  with the impulse response function  $h(x, y)$  over all different points  $(x', y')$  in the input plane. This operation essentially blends the two functions together merging the effect of the free space propagation with the initial 2D electric field amplitude distribution. What we end up with is a third function, namely our output function  $g_{out}(x, y)$ .

$$g_{out}(x, y) = \int \int g_{in}(x', y') h(x - x', y - y') dx' dy' \quad (4.37)$$

Or with the results gathered from the Fresnel approximation:

$$g_{out}(x, y) = h_0 \int \int g_{in}(x', y') \exp \left[ -i\pi \frac{(x - x')^2 + (y - y')^2}{\lambda d} \right] dx' dy' \quad (4.38)$$

#### 4.1.2 Lens in a 2f setup

The present work revolves around an imaging system combining the effect of several lenses and propagation in free space. The lenses are used in a special, so called 2f configuration. In this section, we will here the effect of propagation along this setup and employ the results from the Fresnel approximation.

A separation of the plane wave components propagating at different small angles  $(\theta_x, \theta_y)$  and forming the complex amplitude at a point  $(x, y)$  can be achieved with a thin lens. The lens will transform an incoming plane wave into a paraboloidal wave which is focused to a single point in the focal plane at one focal length  $f$  distance from the lens. The point in the focal plane where the light will be focused can for small angles be written as  $(x, y) = (\theta_x f, \theta_y f) = (\lambda f \nu_x, \lambda f \nu_y)$ . Due to the separation of the plane wave components we can already gather, that the complex amplitude in the focal plane will be depending on the Fourier transform of the input function. In order to calculate the exact form of the complex amplitude we can first use 4.38 to compute the complex amplitude right before the lens. The effect of the lens is added on top of our result so far in the

form of a phase factor  $t(x, y)$  called the complex transmittance.

$$t(x, y) = e^{i\pi \frac{x^2 + y^2}{\lambda f}} \quad (4.39)$$

. We multiply the complex transmittance to our result from the first free space propagation. We take this as our new input function to plug into 4.38 again to compute the complex amplitude after another free space propagation over one focal length. The complex transmittance allows us to break up and partly cancel out the quadratic term in 4.38 such that only the cross terms remain.

$$g_{out}(x, y) \propto \int \int g_{in}(x', y') \exp\left(i2\pi \frac{xx' + yy'}{\lambda f}\right) dx' dy' = F\left(\frac{x}{\lambda f}, \frac{y}{\lambda f}\right) \quad (4.40)$$

Here  $F\left(\frac{x}{\lambda f}, \frac{y}{\lambda f}\right)$  is the Fourier transform of the input function. The full result after the second free space propagation is:

$$g_{out}(x, y) = h_l \exp\left[i\pi \frac{(x^2 + y^2)(d - f)}{\lambda f d}\right] F\left(\frac{x}{\lambda f}, \frac{y}{\lambda f}\right) \quad (4.41)$$

with  $h_l = i/\lambda f \exp[-ik(d + f)]$ . Note that in this case we only made use of the Fresnel approximation and the Fourier transform of our input came out in the end. It is also possible to obtain the Fourier transform through free space propagation only. In that case one can apply the Fraunhofer approximation, whose validity conditions are however much harder to satisfy, one would have to propagate the light field over much larger distance. Since the Fraunhofer approximation does not play a role in our imaging setup, we will not go further into it here.

We can gather from 4.41 that if the input plane is located one focal length from the lens, i.e.  $d = f$ , the exponential term will simply yield one and we can write:

$$g_{out}(x, y) = h_l F\left(\frac{x}{\lambda f}, \frac{y}{\lambda f}\right) \quad (4.42)$$

This configuration is also called a 2f system as the total length the beam travels is two focal lengths. A lens can also perform the inverse Fourier transform. If we have our 2f setup and end up with the image separated into its Fourier components in the output plane, we can add another 2f setup afterwards. The second lens performs an inverse Fourier transform and recombines the spatial frequencies to reconstruct the original image now four focal lengths from the input plane. Such a 4f setup is a widely used tool. For our setup especially it allows us to magnify or demagnify the beam, where the magnification factor  $M$  is determined by the ratio of the focal lengths of the two lenses:

$$M = \frac{f_1}{f_2} \quad (4.43)$$

By inserting an aperture in the Fourier plane between the lenses we can also manipulate the reconstructed image. For example, since sharp intensity edges in the original image correspond to high spatial frequencies, the respective Fourier components will be relatively far outlying in the Fourier plane. Now by inserting an aperture like an iris, we can block these high frequency components and subsequently the edges in the reconstructed image will be blurred.

### 4.1.3 Diffraction

If we want to modulate the amplitude of our laser beam, one method may be to insert an aperture into a beam path blocking parts of the beam. We will now investigate how an aperture of arbitrary geometry will affect the complex amplitude of our beam. The complex amplitude before ( $g(x, y)$ )

and after  $(g'(x, y))$  the aperture will have the following relationship:

$$g'(x, y) = g(x, y)p(x, y) \quad (4.44)$$

with  $p$  the aperture function, which is often times simply zero wherever the aperture is blocking the beam and one where it is not. Now what we will actually observe in the output plane is the intensity distribution  $I(x, y)$ . As we now know, if we propagate our beam through a 2f setup, we can write the output function as:

$$g_{out}(x, y) = \sqrt{I_i} h_l P\left(\frac{x}{\lambda d}, \frac{y}{\lambda d}\right) \quad (4.45)$$

where  $P$  is the Fourier transform of the aperture function. In reality we have no way of directly measuring the complex amplitude. We can only reconstruct it from measurements of the intensity. What we can actually observe and measure in our imaging setup is thus the intensity pattern formed by the aperture:

$$I(x, y) = \frac{I_i}{(\lambda f)^2} \left| P\left(\frac{x}{\lambda f}, \frac{y}{\lambda f}\right) \right|^2 \quad (4.46)$$

So as an example, if we had a circularly symmetric aperture described by

$$p(x, y) = \begin{cases} 1 & \text{for } \sqrt{x^2 + y^2} \leq 1 \\ 0 & \text{otherwise} \end{cases} \quad (4.47)$$

The intensity distribution at a sufficiently large distance after the aperture would be described by the Fourier transform of  $p$  which is again a circularly symmetric function:

$$P(\nu_r) = \frac{J_1(2\pi\nu_r)}{\nu_r} \quad (4.48)$$

with  $\nu_r = \sqrt{\nu_x^2 + \nu_y^2} = \sqrt{x^2 + y^2}/\lambda f$ . In this case  $J_1$  is the Bessel function of the first kind. The intensity pattern which forms circularly symmetric and shows a maximum peak in the centre with rings around it. This pattern is also known as an Airy pattern.

## 4.2 Gibbs-phenomenon

When building up a step-like function from a finite number of Fourier constituents, overshoot and undershoot is to be expected near the discontinuity. Since the flat top pattern we are trying to create with the DMD are nothing else than two-dimensional functions with a sharp step at the boundary, corresponding to our discontinuity, we expect overshoot and undershoot to appear in our patterns manifesting itself as ripples on the flat top. This is known as the Gibbs phenomenon in Fourier analysis, first described by Willard Gibbs in 1898 [23]. Further descriptions can also be found in [8] and [19].

What happens is that when we approximate a sharp jump using a Fourier series, only infinite Fourier sum will approach the function at the discontinuity, while all finite sums will not converge. As we add Fourier constituents to our approximation we observe it oscillating around the functional value near the discontinuity. This overshoot does not disappear as we add more terms, although the oscillations become more localized in a small region around the jump, their amplitude stabilizes at around 9% of the jump height. This is what we can observe in Figure 9

$$\lim_{N \rightarrow \infty} \max |S_N(x) - f(x)| \approx 0.08949 \times \Delta f \quad (4.49)$$

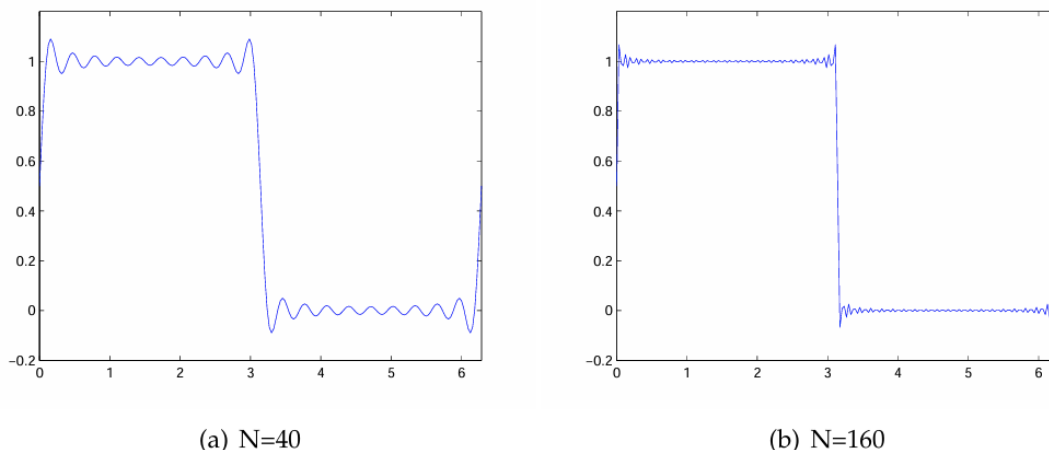


Figure 9: (a) approximation of a step-like function from 40 Fourier constituents, (b) the same with 160 Fourier constituents. Figure from [29]

In this case  $f(x)$  is the function we want to represent with Fourier constituents, including a discontinuity at some point  $x_0$ .  $S_N(x)$  is a sum made up of a finite number  $N$  of constituents and  $\Delta f$  is the jump height of the discontinuity.

The Gibbs phenomenon happens because our Fourier constituents are made up from smooth sine and cosine waves which do not have discontinuities and struggle to represent them by balancing different terms. In the case of our optical setup, we perform optical Fourier transforms of patterns with sharp borders. Sharp borders always correspond to high frequency Fourier components, i.e. far outlying components. Since we can never capture all Fourier components in the next image plane to construct the complete image again, nor do we want to (see 4.3.2). We always expect some oscillations, indicating the Gibbs-phenomenon (later on also called ringing artifacts) to be present when working with patterns that include sharp borders. However since this is not a new problem in the context of signal processing there are also ways to mitigate it, for example smoother functions, which may in fact even be somewhat more beneficial in the context of homogeneous dipolar gases (see 3.3) or applying smoothing filters like Gauss- or low-pass-filters. These are among the methods we tried out ourselves when dealing with ringing artifacts (see 6.2.1 and 6.3), however there are also more complex techniques like applying window functions or using alternative expansions [25].

### 4.3 DMD optics

In the following sections we will make use of the concepts of optical Fourier transforms in the context of our DMD test setup.

In order to create arbitrary light based potentials we use a Digital Micromirror Device (DMD) to modulate a regular Gaussian beam. More specifically we use a V-9001 module from Vialux with a DMD board containing 2560x1600 individual micromirrors. The DMD chip is connected to the control board through a ribbon cable. The DMD is controlled via a Python API Wrapper. Each micromirror is quadratic with a sidelength of 7.6  $\mu\text{m}$ . It may pivot individually along its diagonal axis by  $\pm 12^\circ$ , corresponding to the OFF or ON state of a mirror. A sketch of the functionality of the DMD mirror grid is shown in Figure 10. If the DMD is turned off completely, mirrors typically sit in the 'parked' or 'IDLE' position as indicated in the bottom right of Figure 10.

The DMD is incorporated in an optical system such that if the micromirror array is illuminated, all mirrors in the ON-state will reflect the incoming light further into the setup, while mirrors in

the OFF state reflect the incoming light away or just dump it directly. We image the DMD surface onto the atomic plane via two 4f setups inducing a demagnification factor of 78.

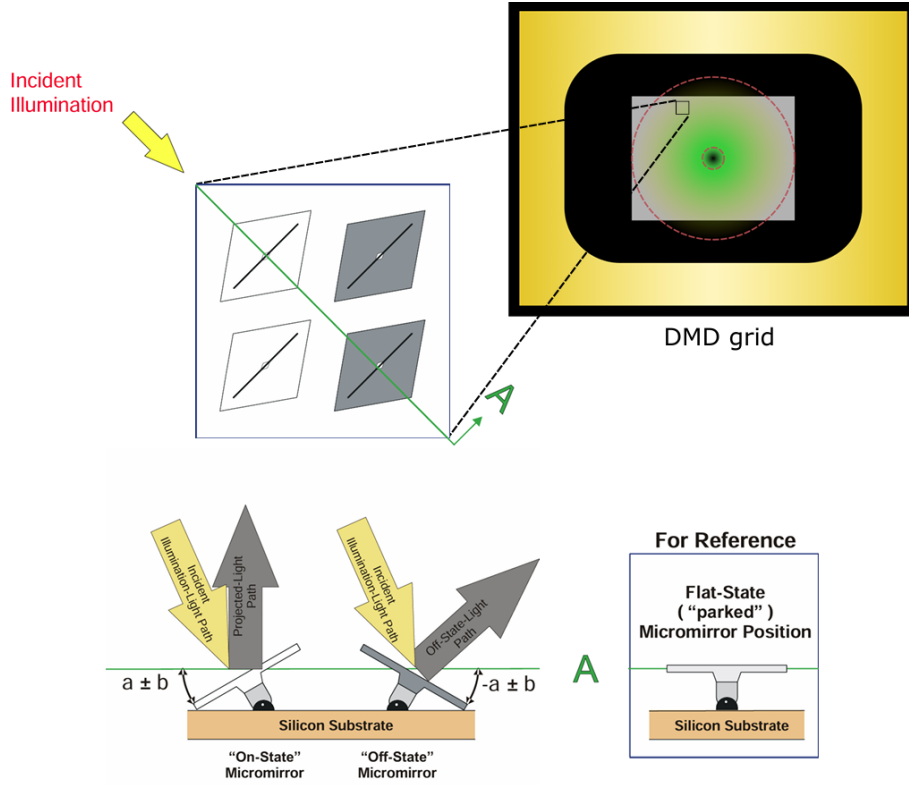


Figure 10: Schematic of the DMD Micromirror grid, illumination by circular beam indicated. Not to scale, adapted from [61]

#### 4.3.1 DMD illumination

Due to the size and arrangement of the more than 4 million individual mirrors, the DMD array effectively acts as a blaze grating. According to the Huygens-Fresnel principle, each point along a wavefront is itself the origin of a spherical wavelet ([51]). From every point of our grating, we get a spherical wave which all interfere with each other. Where they interfere constructively is determined through the path difference of the individual waves, which in turn depends on the grating constant  $d$ , i.e. the distance between the mirrors, the angle of incident light  $\alpha$ , the angle of outgoing light  $\beta$  and the wavelength of the light (see Figure 11). The diffraction of light of a specific wavelength  $\lambda$  is maximized through constructive interference if the following condition also known as the blaze condition is fulfilled (see also [47]):

$$m\lambda = d(\sin \alpha + \sin \beta) \quad (4.50)$$

With  $m \in \mathbb{Z}$ . The incident angle  $\alpha$  is related to the outgoing angle  $\beta$  via the tilt angle  $\theta$ , given by the mechanical design of the chip, in our case  $\theta = 12^\circ$ .

$$\beta = -\alpha + 2\theta \quad (4.51)$$

In order to image the whole DMD as precisely as possible onto our atomic plane and minimize aberration we choose  $\beta = 0$ , i.e. the illuminating beam should be reflected off of the DMD chip

perpendicularly. Via 4.51 this immediately tells us we should have  $\alpha = 24^\circ$ . However if we put this into 4.50, together with the wavelength we will be using,  $\lambda = 532 \text{ nm}$  and the mirror spacing  $d = \sqrt{2} \times 7.6 \text{ }\mu\text{m}$ , we see that the maximum diffraction efficiency will be achieved for order  $m = 5.81$ , thus 4.50 is not fulfilled with our initial choice of angles. Choosing the closest whole number as our diffraction order  $m = 6$  would in turn yield an incident angle of  $24.8^\circ$ . Illuminating the DMD at this angle will give us the best diffraction efficiency, i.e. the highest possible intensity reflected perpendicularly off of the DMD chip towards the atoms.

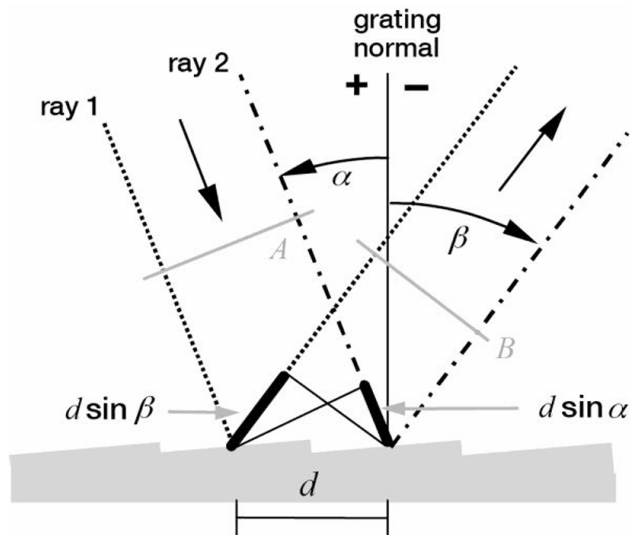


Figure 11: Two incoming rays of light are reflected from a grating. Notation as in text. Figure from [47]

### 4.3.2 Greyscaling

The DMD allows us to control each micromirror individually, thus the images loaded onto the DMD chip always have a bit depth of one, a single pixel being in either the ON or OFF state. The mirror patterns formed on the DMD act as our apertures which are imaged through our setup. As mentioned in 4.3, along our setup, the image is demagnified by a factor of approximately 78. In the demagnified image, individual pixels are no longer distinguishable from their next neighbours since our resolution is limited. This on the other hand allows us to greyscale the image, i.e. access multiple different intensity levels, not only ON or OFF.

A single micromirror acting as a point source of light, reflecting light into the optical setup will form an image well approximated by an Airy disk:

$$I(x) = I_0 \left[ \frac{2J_1(x)}{x} \right]^2 \quad (4.52)$$

Here  $I_0$  is the maximum intensity reached at the centre of the pattern and  $J_1$  is the Bessel function of the first kind of order one. Furthermore  $x = ka \sin \theta$  with  $k = 2\pi/\lambda$  the wavenumber,  $a$  the radius of the aperture we are imaging and  $\theta$  the angle between the optical axis and a line connecting the centre of our aperture with the a point  $x$  in the imaging plane. The intensity distribution imaging a single pixel shows a central peak with a tail containing multiple side minima and maxima. Two neighbouring pixels will have their Airy function overlapping. Whether two pixels are distinguishable from each other depends on the width of the Airy function. In other words: the radial position of the first minimum or dark ring around the central peak will determine

the achievable resolution  $r$ . From the Bessel function we know that the first minimum occurs at  $x \approx 3.83$ , therefore we can write with the above definitions:

$$r_{theo} = \frac{1.22\lambda}{2NA} \quad (4.53)$$

If we plug in the  $NA=0.6$  of our custom designed microscope objective from special optics, we end up with a theoretical resolution of  $r_{theo} = 541$  nm for a wavelength of  $\lambda = 532$  nm. In tests with optical setups involving much less components a resolution of  $r = 573$  nm was reached before [48]. In our setup, the demagnified image of a single micromirror would, in an ideal imaging setup, result in a square with a side length of about 100 nm. This is well below the diffraction limit, thus it assumes the shape of an Airy disk. By fine tuning the tilt of the objective we try to minimize the radius at which the first minimum appears and finally end up with a measured resolution of about  $r = 841$  nm (see also 5.1.2). We calculate the number of greyscales the following way:

$$\text{Number of accessible greyscales} = \left( \frac{\text{Resolution} \times \text{Demagnification}}{\sqrt{2} \times \text{Mirror size}} \right)^2 \quad (4.54)$$

Plugging in our numbers, this means we can only resolve batches of  $6 \times 6$  mirrors, allowing us to access 36 greyscales.

### 4.3.3 Dithering

There are many different but two most common ways in which we can tune our binary image in order to access the different greyscales. We can batch however many neighbouring pixels we are not able to resolve individually together and turn on a certain number of mirrors in this superpixel depending on the desired greyscale [2]. The distribution of 'ON' and 'OFF' mirrors within each superpixel follows a characteristic pattern depending on the greylevel. This method is called ordered dithering or Bayer-dithering and can however lead to unwanted artefacts being visible in the image. Especially in regions where the greylevel is not changing much, straight lines may appear as the individual superpixels become visible, this can be seen in Figure 12 (b) or Figure 13 (a).

The other way to greyscale an image is to employ Floyd-Steinberg dithering [20]. Here we take a

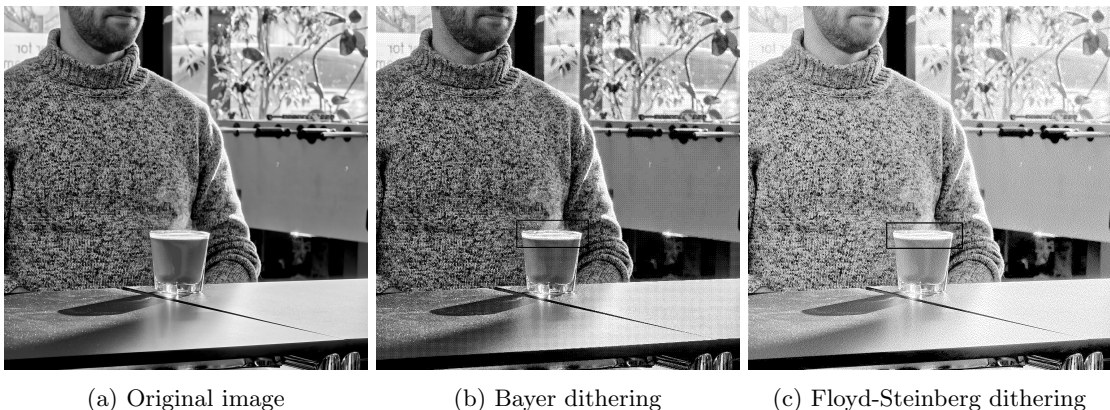
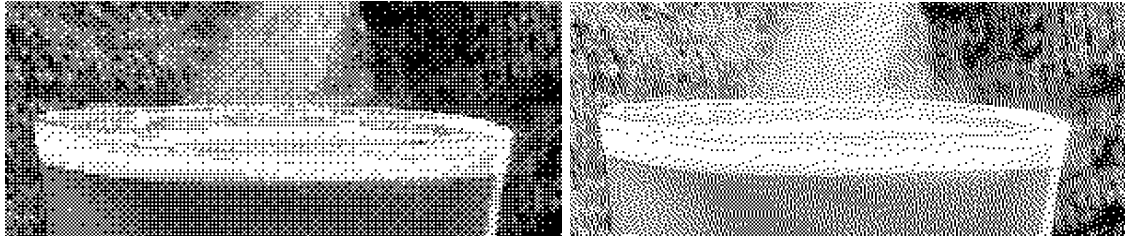


Figure 12: Two different ways to dither (a) an original 8-bit black and white image (b) with Bayer dithering, the size of the superpixel being  $8 \times 8$  in this case, and (c) Floyd-Steinberg dithering. The black frame is zoomed in on in Figure 13. Original image courtesy of Guo-Xian Su; with permission from Wyatt Kirkby.

normalized 8-bit target image we want to dither and starting from the top left pixel, we diffuse the



(a) Bayer dithering

(b) Floyd-Steinberg dithering

Figure 13: Zoom in on the black-framed region in Figure 12 (b) and (c).

error in the image due to the loss of information over the whole image. If the normalized intensity value of the target pixel is below 0.5, the binary pixel will be rounded to 0 or to 1 if the value is above 0.5. The error, i.e. the difference between target pixel and rounded binary pixel is then distributed to the neighbouring pixels following a kernel matrix and added on top of their 8-bit value.

$$\text{Kernel matrix} = \begin{bmatrix} 0 & * & \frac{7}{16} \\ \frac{3}{16} & \frac{5}{16} & \frac{1}{16} \end{bmatrix} \quad (4.55)$$

In this way the state of each micromirror is determined individually and errors are diffused over the whole image while the dithering algorithm works its way from the top left to the bottom right. Thus also the formation of superpixels is prevented, there are none visible in Figure 12 (c) or Figure 13 (b). In our DMD control program, whenever we need to convert an 8-bit image to a 1-bit image, we use Floyd-Steinberg dithering.

## 5 DMD Imaging Setup

In the following chapter we will go in depth through the various components of our imaging setup. The very general purpose of this setup is to image arbitrary geometries displayed on a grid of micromirrors and imprint them on a cloud of atoms through attractive trapping. We translated this purpose in a set of requirements for our setup. In particular we need to:

- Illuminate the full grid of the DMD with 532 nm light under an appropriate incident angle to maximize diffraction efficiency
- Demagnify the beam coming off of the DMD by a factor of about 80 at the position of the atom cloud to make sure the imprinted pattern is smaller than the cloud itself
- Include a part which allows us to perform light-based optimisations of the beam shape through a feedback algorithm
- Include a setup for active power stabilization

During this section we will focus on the first three points. The DMD Imaging Setup was first constructed on a separate customarily designed breadboard in our Preplab. The idea behind this is that the whole setup would be easily accessible during the buildup and testing phases and once that was concluded, the whole breadboard with all necessary components mounted could be moved to its designated position in the main experiment, where accessibility is much more limited. A sketch of the test setup can be seen in Figure 14 and will be described in this chapter.

During all tests we used a 532 nm Laser Diode (*CW532-005* from *Roithner Lasertechnik*). Its light is coupled into a fibre (*PMC-E-530Si-4.0-NA009-3-APC.EC.TI-100-P* from *Schäfter+Kirchhoff*) and coupled out on the breadboard, providing the test setup with 1-2 mW of light depending on the coupling efficiency. We used a shear plate to make sure the beam coming out of the fibre was collimated and cleaned the polarization with a half-waveplate, a PBS cube and another half-waveplate. The initial waist is roughly 1.75 mm and thus has to be expanded in order to illuminate the whole DMD array. We therefore sent the beam through a magnifying telescope before the DMD consisting of a one inch lens with  $f = -60$  mm (E1 in 14) and a two-inch lens with  $f = 200$  mm (E2), together forming a magnifying telescope with a magnification factor of roughly 3.3 such that the resulting beam has a waist of a little less than 6 mm. We put the second lens onto a linear translation stage and again used the shear plate to make sure the now magnified beam is well collimated, moving translation stage until this was the case.

As described above in chapter 4.3.1, we now need to send the beam towards the DMD chip under a specific angle to maximize the power coupled into the diffraction order leading perpendicularly away from the chip. Our DMD itself is embedded in a Digital Light Processing (DLP) chipset (*DLP9000X* & *DLPC910*) from *Texas Instruments* which is in turn embedded in a *V-9001* control module from *Vialux* connected to the chipset through a ribbon cable. Technically speaking the term DMD only corresponds to our array of micromirrors, however in the following the term DMD may also be used in a more general way for the whole amplitude modulation module. More information on our DMD can be found in

Our collimated beam is sent onto the DMD array through two mirrors, one reflecting the beam at  $90^\circ$  the other one at an angle of about  $24^\circ$  to ensure the blaze condition (see 4.50) is fulfilled. To optimise the tilt angle of the second mirror, we turned all micromirrors of the DMD into the ON position and slowly tilted the mirror to find the angle at which the intensity reflected perpendicularly off the DMD reaches its maximum. At the same time we had to make sure, that the beam hits the centre of the DMD. Therefore we displayed a circle with radius of about 500

<i>DLP9000X &amp; DLPC910</i> chipset properties	
DMD array size	2560 × 1600
DMD array area	19.4 × 12.1 mm <sup>2</sup>
Micromirror pitch	7.56 μm
Micromirror tilt angle	±12°
Wavelength range	400 nm-700 nm
Max. switching rate (1-bit)	12 987 Hz
On-board memory (1-bit)	16 777 patterns

Table 3: Overview over some properties of our DMD chipset. More detailed data available in [60] and [62].

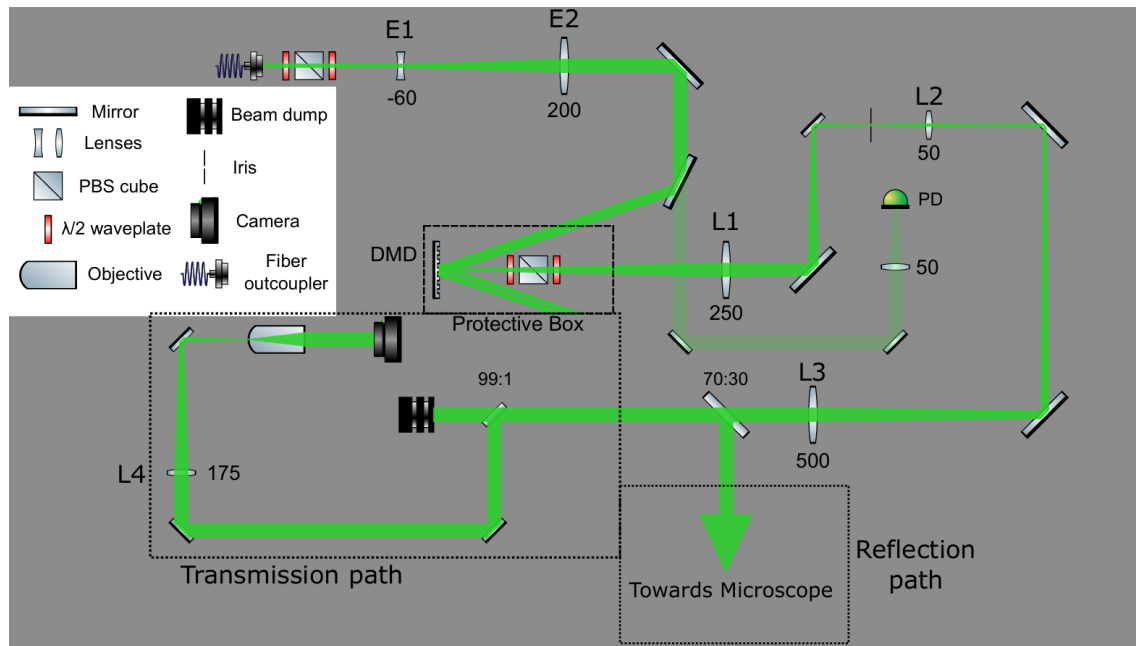


Figure 14: Plan of the full DMD setup as it was finally built into the main experiment. The beam is demagnified over two 4f setups and sampled towards the microscope objective through a 70:30 polarization independent beam sampler. Intensity is stabilized through a feedback loop from the leak light of the last mirror before the DMD.

pixels on the DMD. If the incident Gaussian beam hits the centre of the DMD, the reflected image should have the same intensity along concentric circles.

After the DMD the beam needs to be demagnified again by a factor of about 80. In our case this is achieved with two 4f setups. One that consists of two thin lenses achieving a demagnification of 5, the second one built from a thin lens and completed by our custom made microscope with a demagnification factor of about 16. Together they demagnify the image imprinted into the beam by the DMD by a factor of 80.

The first lens after the DMD, the first lens of the first 4f setup, is a two inch  $f = 250$  mm lens (L1) and it needs to be one focal length distance away from the DMD. To achieve this, we set the DMD into IDLE mode. In this mode all mirrors are in a neutral position, such that the DMD array effectively acts as a regular mirror (see Figure 10). We then sent a collimated beam onto the DMD and made sure overlapped with its backreflection, so it hits the DMD perpendicularly. We mounted the  $f = 250$  mm lens on a translation stage and placed it roughly at the right position one focal length from the DMD. Next we picked up the backreflection with a PBS and checked its collimation again with a shear plate. If the lens is at the

right distance from the DMD the backreflection should be collimated again, so we moved the lens until this was the case (see the alignment setup in Figure 15). Now the main beam coming off of the DMD is focused down one focal length after the first lens of the first 4f setup. Roughly at this position we put an iris, since there the image displayed on the DMD will have undergone an optical Fourier transform and the high frequency components of the Fourier image, which are far outlying from the centre of the beam will be blocked by the iris. This way the reconstructed image after both 4f setups will be slightly smoothed, leading to a lower resolution. Since a lower resolution leads to more accessible greyscales (see 4.3.2), this iris is supposed to act as a tool to manually reduce or increase the number of accessible greyscales by closing or opening the iris, if necessary.

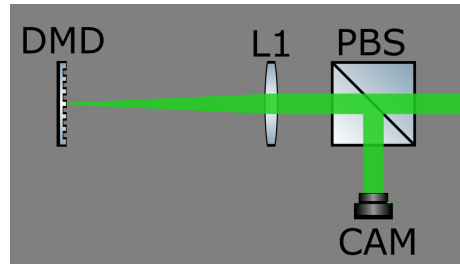


Figure 15: Setup to align L1

We now switched back to the main beam and made sure that it goes through the centre of the first lens and the iris. The second lens of the first 4f setup (L2) is a one inch lens once more mounted on a translation stage and has a focal length of 50 mm. The reconstructed image after this lens and thus after the first 4f setup is demagnified by a factor 5. We positioned a camera near the focal point after the first 4f setup and moved the last lens to different positions as to obtain a relatively aberration free image of a point spread function (see 5.1.2) produced by a single micromirror.

When we display a small Gaussian pattern of less than 100 micromirrors width on the DMD, the beam expands rather quickly due to a very small Rayleigh length after the first 4f setup before being collimated again by the first lens of the second 4f setup (L3). Note that this is not the case for large patterns comparable in size to the illuminating beam. In that case the beam is typically collimated between the two 4f setups and the Rayleigh length after L2 is on the order of a few metres, much longer than the distance between L2 and L3. For now we focused on small images in real space as they give us a good measure as to where to put L3 such that the beam is collimated again afterwards. L3 is a two inch  $f = 500$  mm lens which is also mounted on a translation stage. Just as before it was put at approximately the right position, which was in turn fine tuned with the help of a shear plate. After this lens however the beam will be split in two parts. We do this with a polarization independent beam splitter with a 30:70 ratio. 70% of the light is reflected while 30% is transmitted. The transmitted light is guided towards a camera to perform light based optimisations of the DMD pattern. The reflected light is picked up and led towards our microscope objective and focused on the atomic plane. More on this particular section of the setup can be read in chapter 5.2.3. From now on we will speak of the two paths as the reflection and the transmission part respectively.

On the transmission path, right after L3 setup and after the first beam splitter, the beam intensity is once more reduced through another beam splitter with a 1:99 ratio, 1% being used and 99% being sent directly to a beam dump. We do this since the optimisation routine needs much less light than what we plan to use on the atoms. The intensity-reduced beam is then guided towards the second lens of the second 4f setup (L4), which in the case of the transmission path is a regular one inch  $f = 175$  mm lens mounted on a translation stage. This lens focuses the previously collimated beam and at the same time reconstructs the real space image displayed on the DMD, now with a demagnification factor of roughly 14.3 in the focal plane. The focal plane in this transmission path setup acts as an equivalent to our atom plane in the reflection path. Even though the overall demagnification factor in the transmission path is much smaller than it will be in the reflection path with our microscope, it is still very hard to make out any structures, which form in the focal

plane with a camera placed directly in the focus of the beam. Thus, in order to observe the reconstructed real space image, we place an *Olympus PLN 20X* microscope objective near the focal position to magnify the image again. The overall magnification of the image from the DMD to the camera where it is captured is now roughly 1.4, i.e. the effective size of a  $7.6\ \mu\text{m}$  DMD mirror in the image plane is about  $10.6\ \mu\text{m}$ .

The objective is mounted on a five-axis translation stage and magnifies the image again. Roughly at the effective focal length of the objective, the camera with which we plan to run our light-based optimisation routine is placed. Now we display some image on the DMD that has sharp edges, usually a checkerboard pattern. We move the second lens of the second 4f setup back and forth until we can capture as sharp of an image as possible. Afterwards we again display a single mirror on the DMD and check the PSF on the camera. We use the five-axis stage to tilt the objective and fine tune it such that the PSF is as aberration free as possible. For imaging we always used either a *Mako G-234* or a *Mako G-319* camera or a *WinCamD-LCM* beam profiler camera.

During our tests, before the DMD setup was built into the main experiment, the 'reflection path' was built in different ways either trying to closely match the setup in the main experiment or the setup of the transmission path, depending on what part of the setup we focused on. A more detailed report on probing the comparability of the two paths will also follow in chapter 5.2.3. In the main setup, the 'reflection path' should be guided towards a dichroic mirror. From there it is reflected straight down onto our custom made microscope objective from Special Optics, which in this case acts as the second lens of the second 4f setup with an effective focal length of  $f = 32.2\ \text{mm}$ . The image should reconstruct in the atomic plane just below the microscope objective.

## 5.1 Characterization

We would like to characterize a few key parameters of our DMD setup, including the two 4f-setsups. The last lens on the breadboard before the beam is sent towards the special optics objective and the vacuum chamber is the first lens of the second 4f setup. We need to make sure, that we can produce a broad collimated Gaussian beam after this lens to be focused to a small tweezer beam by the microscope. This tweezer should then help us to align the DMD setup to the atomic plane. The following section (5.1.1) will report on observations made when characterizing the output beam after three lenses, so one and a half 4f setups. We also report on quantitative characterizations of the whole optical system through measurements of the point spread function (PSF) in 5.1.2 and the Modulation transfer function (MTF) in 5.1.3 after the two full 4f setups in transmission as well as in reflection. Ultimately some test results of pointing stability measurements of the laser beam will be presented in 5.1.4. All these characterizations were carried out for the transmission path and the reflection path separately. Finally we will move on to investigate how comparable the two paths are in 5.2.3.

### 5.1.1 Collimation in Fourier-space

In order to verify that the beam propagating towards the special optics objective is well collimated in the case of small DMD patterns, we probed the collimation and defocus of the wavefront by measuring the beam size at different positions, by probing the wavefront with a Shack-Hartmann sensor and by using a shear plate.

During the first rough alignment, we simply measured out the designate positions of the second lens of the first 4f setup and the first lens of the second 4f setup. We then displayed a pattern with the DMD which gives us a small Gaussian beam in the real space domain or a wide Gaussian

beam in Fourier space. Since our atoms lie in the image plane after the second 4f setup, we want a broad beam in the Fourier plane, encompassing the whole width of the special optics objective, which is then being focused to a narrow tweezer. Now the beam illuminating the DMD is itself a Gaussian beam, however it is very broad. This means though around its centre there is a reasonably wide region where the intensity only drops slowly. We display a dithered Gaussian pattern within this region which proved to produce what we wanted, a small, circular Gaussian beam. In Figure 16 we can observe a small sketch indicating the size of the beam illuminating the DMD and the approximate size of the pattern in the centre of the DMD to produce this Gaussian. In the plot on the right side of this figure we see a simulated cross sections of the illuminating beam, the 8-bit DMD pattern, which is later dithered and the resulting beam, which is a convolution of the two. We have to zoom in very far to see the difference between the Gaussian DMD pattern and the resulting beam shape. As mentioned before, the smaller the Gaussian pattern we display on the DMD, the larger the Fourier image. Though if our Gaussian pattern only consists of a few mirrors, it can not be properly greyscaled anymore and the resulting image will shift towards an Airy pattern.

The small Gaussian beam is transformed into a wide Gaussian in the Fourier plane at the output

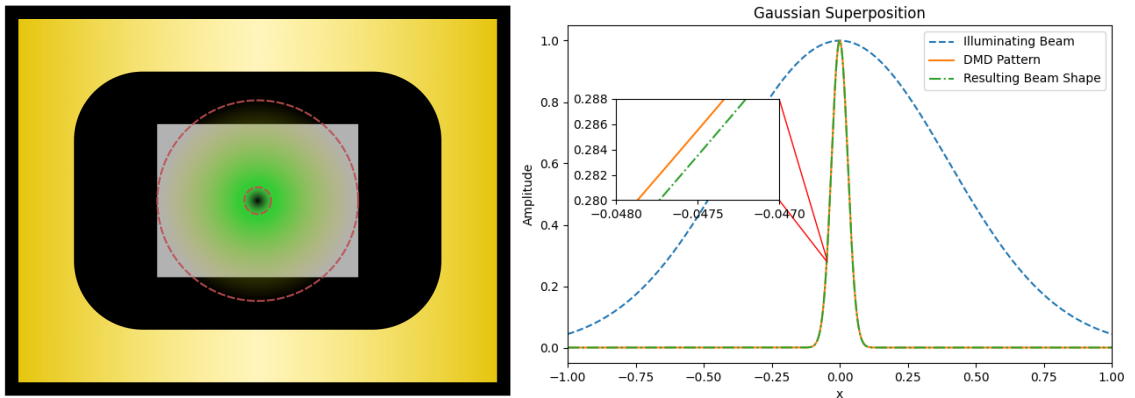


Figure 16: Left: Drawing of the DMD chip with large illuminating beam and small imprinted beam. The dashed lines indicating the circumference of the beams. Right: Simulation of an amplitude cross section of the beams with a small zoom-in region indicating the variation in beam shape resulting from the overlap of the two Gaussians.

of the DMD imaging setup. In order to probe our first rough alignment we measured the beam waist with a beam profiler camera at different positions spread out over in total four metres. The results can be seen in Figure 18. After a measurement we would map out the beam's divergence and move the two lenses mentioned above in order to improve the collimation. It quickly became clear that moving the second lens of the first 4f setup had a much larger effect while moving the first lens of the second 4f setup only very slowly reveals a change in collimation. After few iterations the output beam showed no visible divergence over 4 m anymore. We tested also several differently sized Gaussian profiles. All of them seemed to be collimated well, however we observed that for large profiles displayed on the DMD, i.e. small profiles in the Fourier plane, the beam became more and more elliptic to a point where it seemed to form several individual intensity drops disconnected from each other. This can also be observed in Figure 17. Here four different beam profiles in the Fourier plane are shown. The larger the waist of the beam in real space, the smaller it is in Fourier space, yet at the same time we observe some ellipticity already at  $\sigma = 50$  mirrors, but it increases to a point where we see individual dots instead of a beam at  $\sigma = 200$  mirrors.

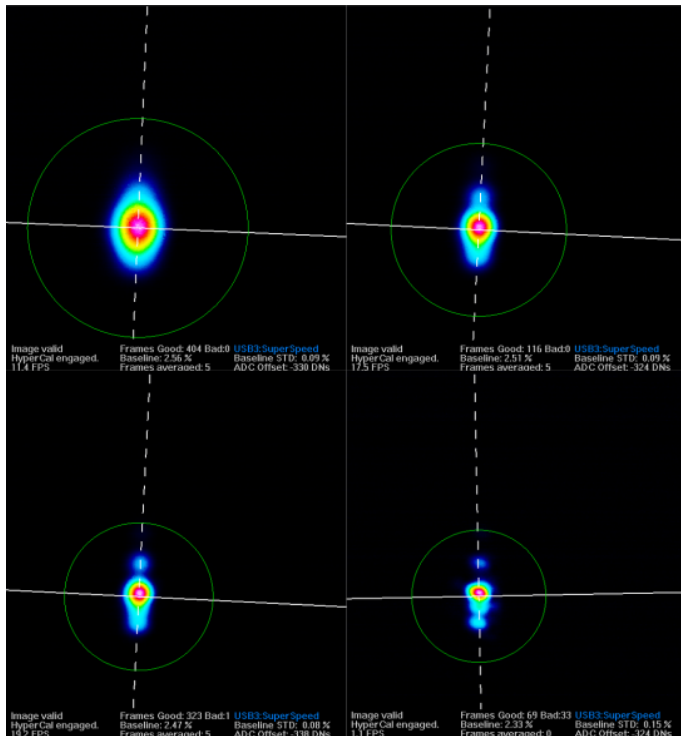


Figure 17: Beam profiles of Gaussian beams the Fourier plane with increasing waist in real space. From left to right and top down:  $\sigma = 50, 75, 100$  and  $200$  mirrors.

to-valley distance of our wavefront, from the centre of the beam to its edge, is given by  $2A$  in units of a wavelength. We once again tried out different beam sizes and could by the cuts of the wavefront confirm that small beams in the Fourier plane grow more and more elliptic. Regarding the wavefront aberration, we measured what seems to be a flip from a convergent to a divergent beam as the waist increased (see Figure 18). However, in the range in which we varied the waist, the Zernike defocus, sometimes simply called the Z5 coefficient remained below an absolute value of 0.02. For our wavelength of 532 nm, this corresponds to a peak-to-valley distance of the wavefront of a little more than 20 nm, which is reasonably small for our purposes. We can therefore confirm that the output beam is well enough collimated. Furthermore we made the observation that moving the first lens of the second 4f setup to different positions on the translation stage barely changes the collimation of the beam. The positioning of the second lens of the first 4f setup is much more sensitive.

What remained was the ellipticity in the patterns which we could not really explain yet. We tried out different patterns to check whether the Fourier image that forms matches what we would expect for the respective patterns. We quickly noticed that this was not the case. Instead we would observe intensity blobs, which in no way seemed to resemble a Fourier transform of the input pattern. The larger the DMD pattern the more distorted the Fourier pattern would be. What was perhaps even stranger was that after the optical inverse transform, i.e. after the second lens of the second 4f setup, the initial image could be recovered with minimal and no unexpected aberrations. After some research we managed to find two references which observed the same thing [16][50]. In both cases the atoms lie in the Fourier plane and in both cases the previously described aberrations were observed and traced back to imperfections of the DMD surface itself, meaning mirrors with a tilt that does not exactly match  $12^\circ$ , perhaps also an uneven mounting surface or dust on the mirrors. As long as these imperfections are distributed sparsely over the whole DMD grid, the resulting

In order to investigate both this and the dependence of the collimation on the beam size a little further we employed our newly bought Shack-Hartmann sensor (*WFS40-5C*). It allows us to probe wavefront aberrations corresponding to a convergent or divergent beam respectively at a single position, thus there is no need to move the sensor over 4 m distance. The wavefront aberration mathematically corresponds to a quadratic variation in the wavefront phase. It is calculated as the defocus term of the Zernike polynomial expansion [64]:

$$Z_2^0(r, \theta) = A(2r^2 - 1) \quad (5.56)$$

Here  $r$  is the normalized radial coordinate and  $A$  is the Zernike defocus coefficient.  $Z_2^0(r, \theta)$  is  $-A$  for  $r = 0$  and  $A$  for  $r = 1$  such that the peak-

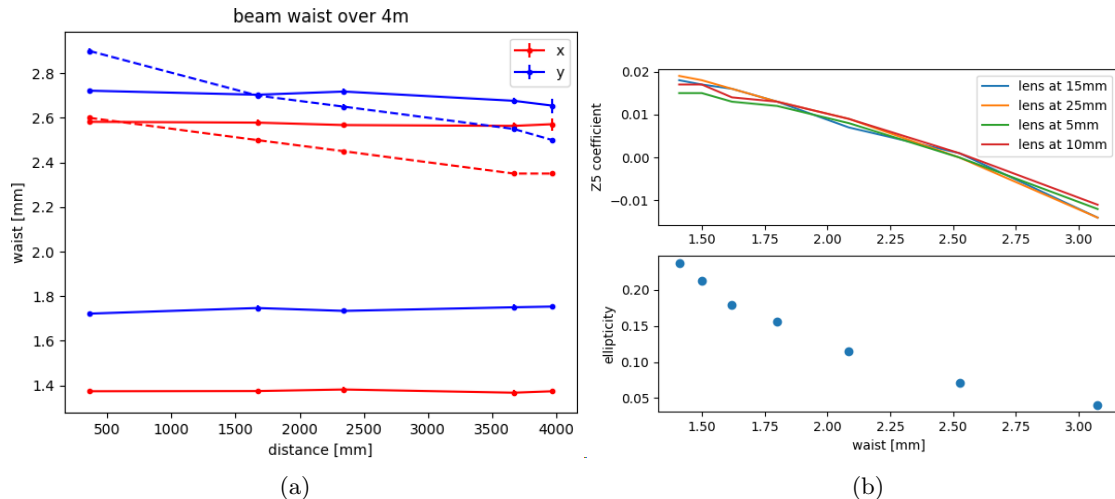


Figure 18: (a) shows the waists in  $x$  and  $y$  direction of a Gaussian beam after the first lens of the second 4f setup over a distance of 4 m. The dotted lines show the initial rough setup, the solid lines show the optimised setup for a broad and a narrow Gaussian beam. The ellipticity increases in the narrow case. The upper plot of (b) shows the Z5 coefficient for different waists and at different lens positions. The lower plot once again shows how the ellipticity increases for small Gaussian beams.

aberrations are unrecognizably small in the real image plane, yet in the Fourier plane when the plane wave components are separated, the image gets distorted. This would also explain why the aberrations grew larger for smaller Fourier images, since in order to produce a small Fourier image we needed to display a large real space image on the DMD which included more micromirrors and more imperfections. In both references the authors report how they manage to optimise the image displayed on the DMD to compensate for the aberrations. Luckily though we plan to have our atoms in the real image plane where we do not need to worry about this as we can well recover the real-space image in which the aberrations are diffused.

### 5.1.2 Point spread function in the image plane

After making sure the output beam after the first lens of the second 4f setup was well collimated we completed the 4f setup in the direction of the reflection path with the special optics objective and in the transmission path with an  $f = 175$  mm lens. In order to characterize the whole optical system further and also improve the alignment, we analysed the point spread function. We would turn on a single micromirror in the middle of the DMD grid. As mentioned before the image forming in the image plane after two 4f setups will be approximated by an Airy disk as can be seen by the 2D intensity profiles in the left part of Figure 19 or also by the 1D cuts through the profiles in the right part of the same Figure. We can determine the radius of the Airy disk through a fit, using the Bessel function as a 1D fit function on the cuts through the profile. The fit is marked by the solid red line in Figure 19.

The smaller the radius and the more intensity is concentrated in the centre peak the closer we can get to our resolution limit. Of course we also need to limit our resolution in order to access enough greyscales however since the limit set by the Rayleigh-criterion (see [48]) already allows for 16 greyscales, we do not need to worry too much about limiting our ability to greyscale. We therefore iteratively tried to minimize the radius of the Airy disk by changing the tilt of our imaging objective.

When we eventually concluded that the radius could no longer be reduced any further we took a

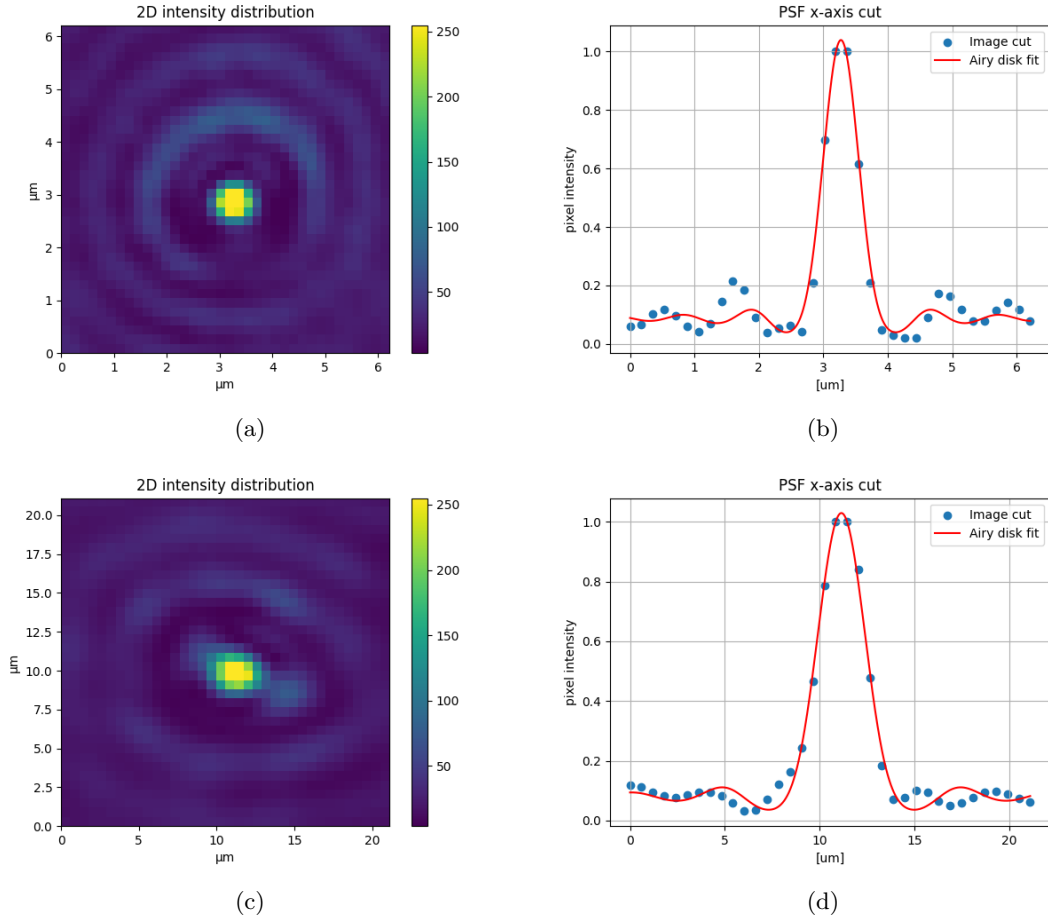


Figure 19: (a) and (c) show the camera image taken in the reflection path and the transmission path respectively. The scales are adjusted in terms of pixel size and magnification. (b) and (d) show one example of the 1D Bessel function fit.

picture of the Airy disk both in the reflection path and in the transmission path. These images are the 2D intensity profiles in the left column of Figure 19. In both cases the image after the two 4f setups had to be magnified with an additional imaging objective. In the case of the reflection path we managed to get an Airy disk radius of 841(26) nm. The error results from averaging as we would perform a 1D fit along multiple different paths through the centre of the Airy disk. In the case of the transmission path we got a radius of 3.49(45)  $\mu\text{m}$ . In previous measurements a resolution of 573 nm was measured for the special optics objective [48]. This was though measured in a much simpler setup containing less optical components which may contribute aberrations to the system. Considering the complexity of the DMD test setup, the achieved resolution is satisfactory and allows for roughly 36 greyscales. In the case of the transmission path the result is a little harder to interpret. On the one hand we observed more aberrations in this path as there was always some degree of ellipticity present. On the other hand, considering the reduced magnification in this path, we can actually resolve individual pixels which lie closer together and access only about 16 greyscales. It remains to be seen how or if this discrepancy manifests itself.

### 5.1.3 Modulation transfer function in the imaging plane

For another quantitative characterization and also as a verification of the recorded PSFs, we tried to determine the modulation transfer function or MTF similar as in [28], even though instead of

imaging the modulations of our density cloud we will for now perform a light-based analysis. The MTF has been proposed as a standard method to determine the resolution in coherent imaging systems [33]. It is defined as the Fourier transform of the PSF. A thorough introduction into optical transfer functions can be found in [63]. The MTF can be determined as follows: We display a Siemens star image on the DMD and record the image in both paths. The Siemens star, as can be seen in Figure 20 is a circular structure consisting of a fixed number of neighbouring light and dark stripes, where one light and one dark stripe is referred to as one cycle. The stripes are narrowing in width as they radially converge towards the centre. At some point along the way, one will no longer be able to distinguish between two neighbouring cycles due to the resolution limit of our setup. During the analysis we determine the average contrast along circular paths around the centre starting from outward going further and further in. Each circular path has a fixed spatial frequency, given in cycles per  $\mu\text{m}$ . We use a logarithmic frequency spacing and map out the contrast over the full size of the Siemens star as can be seen in Figure 21. We observe the contrast decreasing for higher and higher spatial frequencies. This curve, normalized to unity and starting close to one for low frequencies, is commonly known as the Modulation transfer function. It captures how much of the intensity modulations from the object we are imaging, in our case the image in the DMD grid, can be transferred through the optical setup. Eventually, for very high spatial frequencies, the function will approach zero.

We extract the frequency value at which the contrast drops to half its maximum value through a fit and calculate the full width half maximum (FWHM) of the MTF. Since as previously said, MTF and PSF are Fourier transforms of each other, this quantity is related to the FWHM of the PSF [63], [28]:

$$\text{FWHM}_{\text{PSF}} = \frac{4 \ln(2)}{\pi \text{FWHM}_{\text{MTF}}} \quad (5.57)$$

In order to compare both values we therefore also reuse our images of the point-spread-function formed when a single micromirror is displayed from the previous chapter 5.1.2. This time we perform a Gaussian fit and extract the FWHM. In the case of reflection path of the test setup, we found a MTF FWHM of 1.42 cycles/ $\mu\text{m}$ . By using 5.57 we can gather that this corresponds to a PSF FWHM of about 621 nm. Through the Gaussian fit of the actual PSF we got a FWHM of 650(23). Once again with considerable errorbars due to the averaging over a slight ellipticity. The two results seem to match reasonably well. In the case of the transmission path we got a MTF FWHM 0.35 cycles/ $\mu\text{m}$  corresponding to a PSF FWHM of 2.55  $\mu\text{m}$  which also matches the FWHM measured directly on the PSF of 2.72(46)  $\mu\text{m}$ . What was however notable in this path was that the MTF exhibited first a decrease, but then again a sizeable contrast enhancement at about 0.13 cycles/ $\mu\text{m}$ . In the raw image this should manifest itself as perhaps a sort of circular region around the centre where the transition from light to dark stripes is blurred, but becomes sharper again as one goes further inwards. Since we applied a logarithmic scale and the MTF drops rapidly right after the short contrast enhancement, we estimate, that the responsible features in the raw images should be located near the centre. As we zoom in on the centre, we can observe two slightly blurred regions, matching the description from above, see Figure 20 (c). What part of the optical setup introduced the aberrations which lead to the blurring and is thus responsible for the peak in 21 (b) is however not exactly clear. Since we don't see the same effect in the reflection path, the aberrations might perhaps originate from the second lens of the second 4f setup in the transmission path or from the imaging objective.

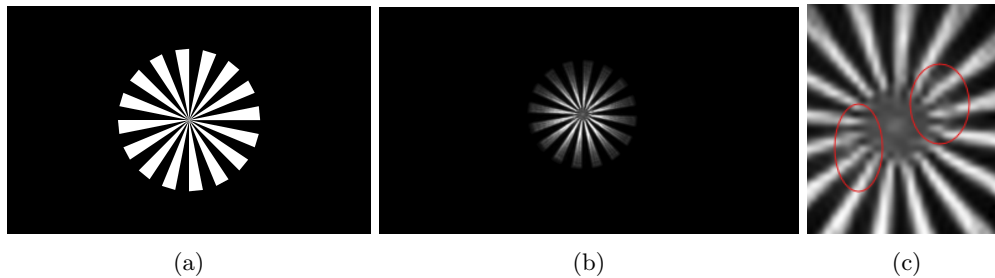


Figure 20: (a), a one-bit image of a Siemens star as it was used in all tests pertaining to the MTF. (b) an exemplary camera image of the Siemens star reconstructed after the two 4f setups and ten times magnified and zoomed in, in this case from the transmission path. (c) a zoom-in on the centre of (b) with the contrast reduced regions circled in red.

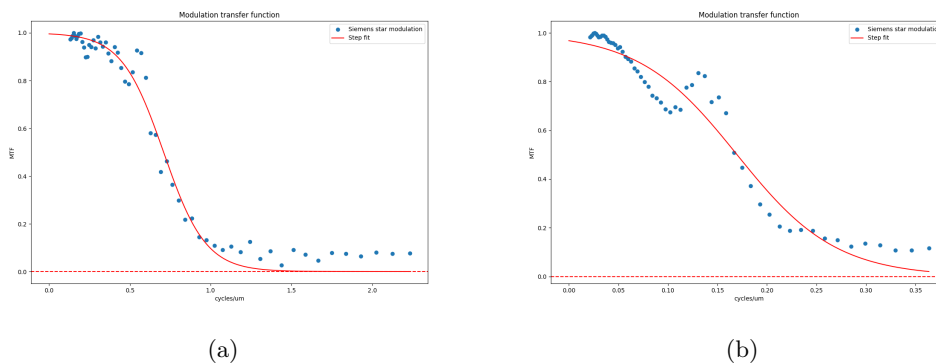


Figure 21: (a) The modulation transfer function of the whole optical setup in the reflection path and (b) in the transmission path.

#### 5.1.4 Pointing stability

In the transmission path we plan to iteratively optimise our DMD images in order to compensate for the Gaussian shape of the incoming beam and also any other aberrations that may be introduced through the DMD grid itself. The images we use for this optimisation are captured in the transmission path in close proximity to the DMD control board. When the DMD is running the chip is at all times air-cooled with a fan, which can not be turned off or in any way controlled remotely. We wanted to probe whether and how the airflow or the vibrations coming off of the fan influences the pointing of the beam of the transmission path. For this we displayed a small Gaussian dot of only about 20 micromirrors width on the DMD. We would then take 100 consecutive images, the time between the images was constrained by the response of the camera and usually amounted to little less than three seconds, but is not exactly constant. This means that unfortunately we can not really probe resonances by simply taking many images one after the other. For now we simply test the drift of our pointing as it might occur when performing multiple experimental sequences with the DMD one after the other, separated by few seconds.

After 100 images have been captured, for each image, we cut out a small region around the Gaussian peak and perform two 1D fits in  $x$  and  $y$  to extract the coordinates of the centre. The average of the  $x$  and  $y$  coordinates was subtracted from the extracted coordinates of each point. The result is shown in Figure 22. We tried this procedure once without any measure to prevent airflow or vibrations from interfering with the beam and once with an aluminium piece between control board and camera acting as a wall and blocking any airflow which might come from the fan. The data from the measurement with the air block corresponds to the orange dots in 22 (a).

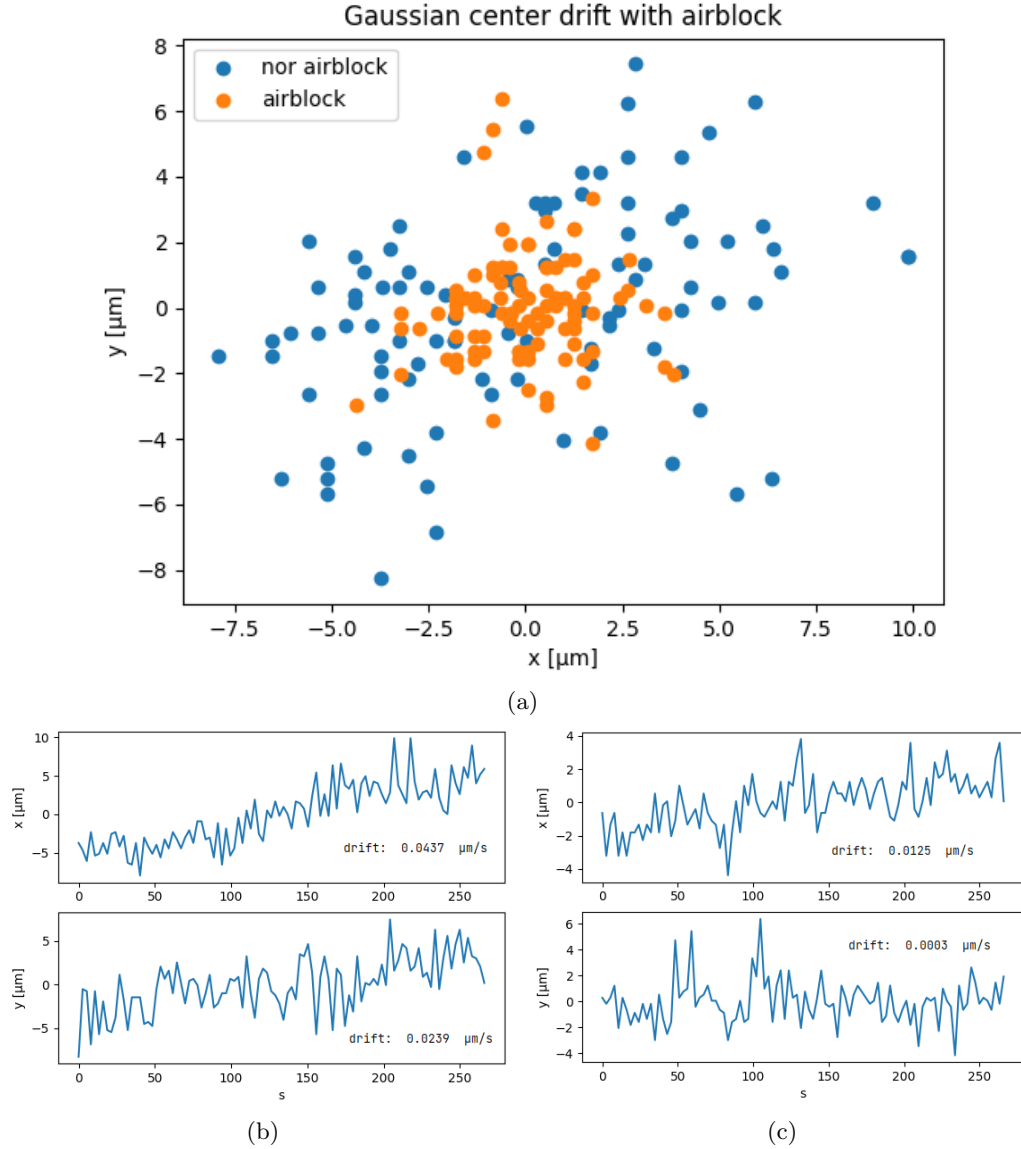


Figure 22: (a) The spread of the recorded and fitted centres of the Gaussian spots on the camera. The measurements with and without an air block are overlaid on top of each other. (b) and (c) show the drift over time in  $x$  and  $y$  with and without an air block respectively. A linear function was fitted to the data points in order to determine and quantify whether there is some systematic drift in one direction.

Already by eye, we can estimate, that the spread of the orange dots is smaller than that of the blue ones, taken without the air block. In both cases we calculated the width of the spread through the standard deviation of the coordinates in  $x$  and  $y$  direction. Without any air block in place the standard deviation of the recorded points was  $\sigma_{x,y} = (4.02, 3.07) \mu\text{m}$ . When the air block was placed between camera and fan, it would shrink to  $\sigma_{x,y} = (1.53, 1.68) \mu\text{m}$ . We also checked if there is some overall drift in one direction over time. The results can be seen in 22 (b) and (c). Note that in this case all quantities correspond to the drift of the Gaussian spot in the camera plane, since that is going to be relevant during the optimisation process when DMD image and camera image are laid on top of each other. No magnification neither from the two 4f setups nor the imaging objective are calculated into the data, only the pixel size of the camera.

We can see that the diffusive variation of the pointing is already quite small without an air block

in place. The standard deviation in both  $x$  and  $y$  direction is smaller than the size of a single camera pixel. However with a metal piece blocking the airflow from the fan towards the beam we can further reduce the deviation by about half of it. This should be sufficiently stable as to not cause any problems during the optimisation. It remains to be seen though if the stability of the pointing changes when the whole setup is moved into the main experiment.

## 5.2 Inclusion of microscope objective

During our efforts of testing and probing as many characteristics of the DMD imaging setup as we could before moving the test setup into the main experiment, we also made use of our spare special optics objective, which should be an exact replica of the objective already installed on the main experimental setup. For the design and tests on the objective see [48]. We built the reflection arm of our imaging setup including the microscope objective as described in 5. This arm should closely replicate the optical path from the DMD towards the atomic plane as it will be in the main experiment.

### 5.2.1 Alignment

The special optics objective completes the second  $4f$  setup in the reflection path (see 5). Figure 23 shows a sketch of the reflection arm including the objective. It connects seamlessly to the path reflecting off of the 70:30 beam sampler from 14.

We thus put it on a five axis translation stage at the approximately right position and fine tune its position and tilt later on. This setup was similar to the one described in [48] for probing the characteristics of the objective itself. In order to align the special optics objective well we tested out several different methods. We can easily unscrew the objective from the test setup. Therefore we first sent medium-sized Gaussian beam through the setup in absence of the objective and made sure it would go straight through the test apparatus at a fixed height. Medium-sized in this case corresponded to a Gaussian pattern of approximately 75-100 mirrors width on the DMD, small enough not to introduce too many aberrations in the Fourier plane (see 5.1.1), but large enough to reflect enough power such that the beam was well visible. This translated to a diameter of around 1.5 mm in the Fourier plane of the second  $4f$  setup, small enough to determine the centre of the beam and thus the beam height by eye. Once we were satisfied with the alignment without the objective we screwed the objective back in and checked that the pointing of the beam was still the same as before, meaning the beam went right through the centre of the objective. In order to fine tune the alignment further we tried to minimize the radius of the point spread function by tilting the objective and evaluating the point spread function as described in sections 5.1.2 and 5.1.3. Though the optimising or minimizing of the PSF radius was rather similar to a random walk across the camera screen by tilting the objective, we managed to bring the PSF FWHM down from between 750 and 800 nm to about 650 nm. These two methods combined already resulted in quite good test images.

In the main experiment setup however we can not simply unscrew the objective and we need some other way to get a rough alignment going before we can try to clear out aberrations by fine tuning. Therefore we tested out differently sized images of a square lattice.

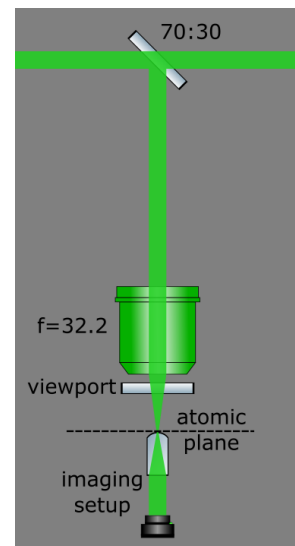


Figure 23: Reflection path with microscope objective

Displaying such an image on the DMD will produce a Fourier image after the first lens of the second 4f setup where there are four outlying spots all at the same distance from the centre corresponding to the lattice frequency or spacing in  $x$  and  $y$ . We only need to find the right spacing such that the outliers overlap with the edge of the objective. We also applied a Gaussian filter to the image to smooth out sharp edges, therewith we prevent the formation of higher frequency components which are not necessary in this case. In Figure 24 (a) a 1-bit image of such a smoothed lattice can be seen, in (b) a simulated Fourier pattern of the same lattice, in (c) a camera image of the laser beam in the Fourier plane when the lattice is displayed on the DMD.

After a few trials we found a small lattice pattern of about  $100 \times 100$  micromirrors which produces the desired Fourier pattern. However since the diameter of the objective is about two inches, so is the Fourier pattern. We therefore need not only a two inch PBS cube but also two two-inch elliptic mirrors to guide the beam towards the objective without cutting any of the outlying spots which should help us align the objective. Thankfully all necessary parts are already in place in the main setup. In the test setup some rebuilding and realigning was required but we ultimately managed to see that our efforts were worthwhile and our chosen method seemed promising.

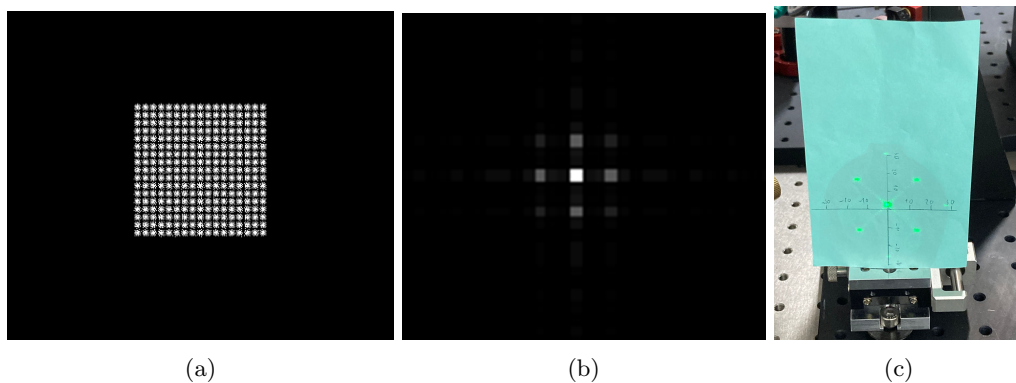


Figure 24: (a) A 1-bit DMD pattern of a smoothed lattice, (b) its simulated Fourier pattern and (c) the actual laser pattern in the Fourier plane when the lattice pattern is displayed on the DMD.

### 5.2.2 Imaging tests

The DMD test setup now included the second special optics objective which completes the second 4f setup in the reflection path. The effective focal length of the objective is 32.2 mm. Over the whole setup we thus now got a demagnification by a factor 78. Right after the objective, we also included a small glass window to mimic the viewport of the main setup (see Figure 23). Our mock atom plane laid a few millimetres behind this viewport. Due to the large demagnification and subsequently small pattern in the atom plane, we used another imaging objective, which would again magnify the image by a factor 20 before the camera would capture it. We could now try out different patterns in an optical setup closely resembling the situation in the main experiment. In Figure 25, some exemplary images that were captured in the setup shown in Figure 23 can be seen, such as (a) a ring, (b) a chequerboard pattern, (c) our group name or (d) just an as small as possible tweezer beam. This tweezer is effectively nothing else than a Gaussian mirror pattern of roughly 25 micromirrors width. This small pattern in the centre of the DMD array produces a wide Gaussian with almost 2.5 mm waist in the Fourier plane before the objective. After the microscope objective it is focused down to a spot with only about  $3 \mu\text{m}$  waist. We can use this pattern to produce a very narrow tweezer in which we can later on load atoms, to act as something like a

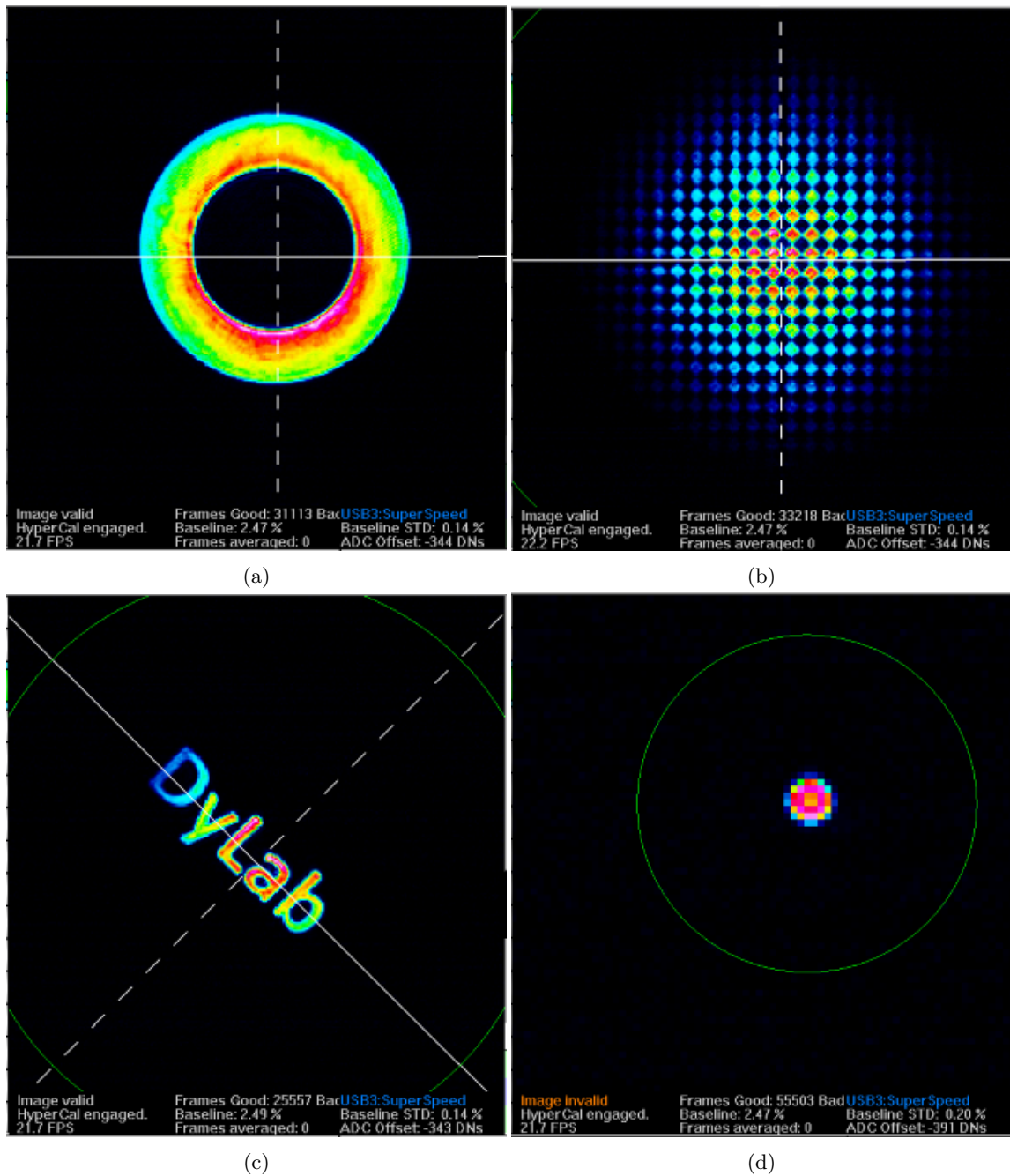


Figure 25: (a)-(c) Exemplary images of more or less complicated DMD patterns captured in the reflection path. (d) An image of a tweezer beam produced with a Gaussian of roughly 25 mirrors width. The camera is having some troubles imaging the profile, since even after the re-magnification, the beam only has a waist of about  $150\ \mu\text{m}$  corresponding to few pixels on this camera.

marker for the DMD position during the alignment. This goes for the position in the horizontal  $xy$ -plane as well as the focus position in  $z$ .

### 5.2.3 Optimisation mismatch in transmission and reflection

Another important thing to test with the objective in place was how a pattern which was iteratively optimised in the transmission path translates into the reflection path. Here we should ideally be able to observe the same pattern. The two optimisation algorithms we used to compensate for

the Gaussian intensity profile of the incoming beam will be the topic of the next chapter and are explained in depth there, as well as in [7] and [37]. For now we will assume, that we managed to produce a flat-top intensity pattern with a RMS error of around two percent of the normalized plateau intensity across the flat top by performing a light based optimisation in the transmission path. For the trials we used a  $400 \times 400$  micromirror square shape pattern with rounded corners. When the DMD pattern which was optimised in the transmission path would be imaged in the mock setup of the reflection path, containing an exact replica of the microscope used in the actual experiment, it quickly became clear that it did not resemble at all the successfully optimised pattern from the transmission path. In fact we would typically observe a drastic increase in intensity on one side of the square. This can clearly be observed in Figure 26. On the left we see an optimised pattern in the transmission path, even though the optimisation result is not perfect, we managed to produce a flat top beam in this path. The same pattern is imaged in the reflection path on the right. The steep spike in intensity on one side of the square is clearly visible. We first briefly

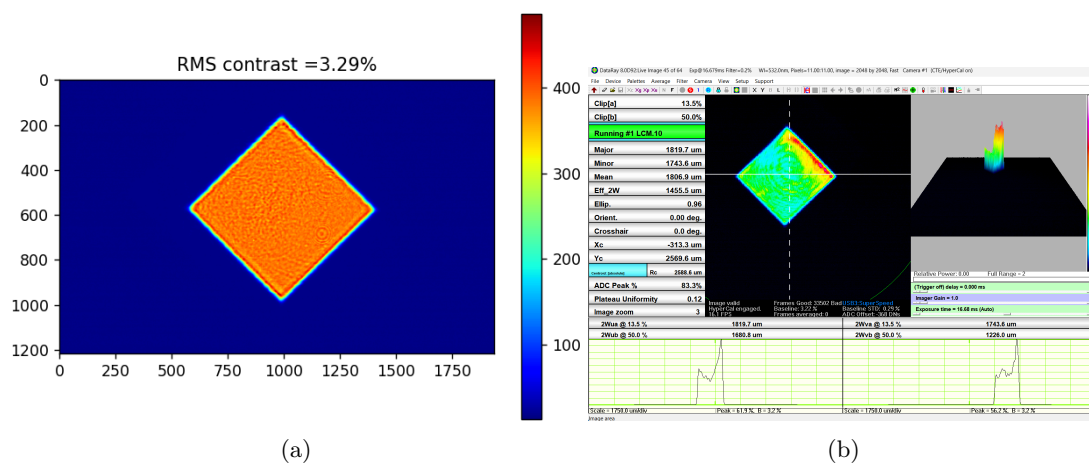


Figure 26: (a) 2D intensity distribution of pattern optimised in transmission path, (b) the same pattern imaged in the reflection path, with a drastic spike of intensity towards one side.

checked the shape of the beam right before the PBS cube and in the transmission and reflection axis right after it. We could once again observe some aberrations in the Fourier plane as described in chapter 5.1.1, however the aberrated shape seemed to match closely in both axes after the cube. Next we built a half-waveplate in front of the cube to turn the polarization axis in front of the light. We did this to investigate whether even though we cleaned the polarization of our beam before the DMD, the DMD perhaps introduces polarization aberrations into the light leading to an uneven polarization distribution in the beam, which in turn leads to an uneven splitting of the beam through the PBS. By turning the waveplate in front of the PBS we should be able to tune the splitting of light and observe a change in the patterns both in the reflection path. We only slightly turned the waveplate by a few degrees and imaged the optimised pattern again with our objective setup. We could observe how the intensity distribution on the image we took in the reflection arm would change when the waveplate was rotated. We could recreate the distribution we initially saw with the sharp intensity peak on one side (Figure 27 (c)), but we could also observe slightly more evened out pattern, though they could not be considered flat by any means (Figure 27 (a) and (b)).

To confirm that this issue came from polarization effects, we removed the PBS cube from the setup and replaced it with a flip mirror. If the flip mirror was flipped down, the beam would be transmitted towards the camera used for the optimisation, if the mirror was flipped up, it was be reflected towards the objective. Once again we ran our optimisation routine. When the

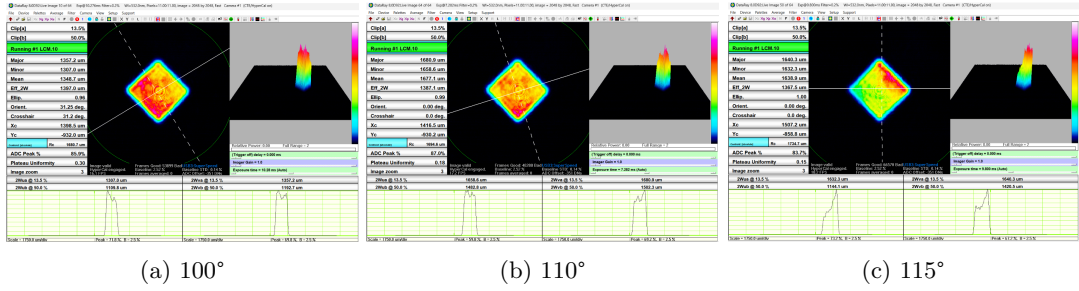


Figure 27: Rounded square pattern optimised in transmission, imaged in reflection. The angle below the individual images corresponds to the absolute reading on the waveplate.

optimised pattern was saved we flipped the mirror up and recorded the image which formed after the objective. The result was once more unsatisfactory and can be observed in Figure 28. The intensity distribution again showed very large and diffuse variations across the square corresponding to roughly ten percent root mean square error (RMSE) (see 6.4.1), even though once the mirror was flipped down again, the two percent RMSE which was achieved in the optimisation could be recovered through the original optimisation camera.

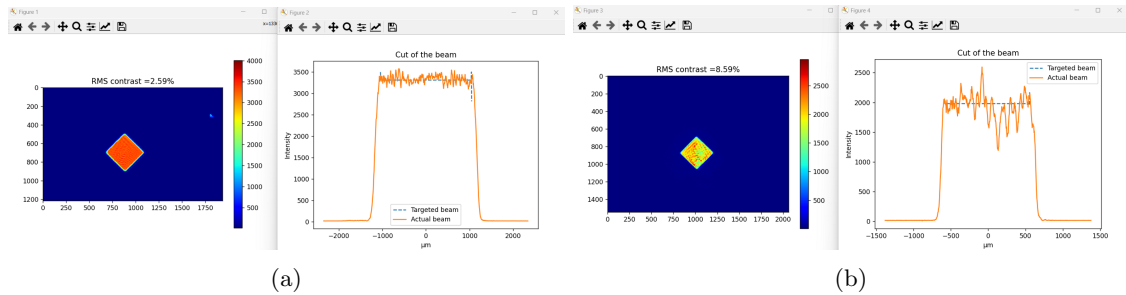


Figure 28: (a) The optimisation result including a 1D cut through the centre of the beam in the transmission arm. (b) The same pattern imaged in the reflection arm.

To investigate this further we built a third path of the optical setup in the reflection direction. This path would exactly mirror the optical setup that existed in the transmission path on the breadboard. We could switch between this setup and the objective setup with another flip mirror (see Figure 29). Yet still the images of the same DMD pattern from this third path and the transmission path did not match, although the RMSE in the third path could be reduced to around seven percent. We tried to fine tune the alignment of the third arm in order to push this value down towards a boundary which would be our target value when the setup was rebuilt such as it was initially intended. We employed similar techniques as were also described above in 5.2.1 and applied them this time to the imaging objective which was set on a five axis translation stage. Additionally we set out systematically rebuild and realign the whole optical path of our DMD setup starting from the fibre output to try to minimize any aberrations which might contribute to the mismatch of the images. These efforts finally proved to be somewhat worthwhile. We managed to run the optimisation routine both in the originally designated path and in the newly build third path. In both cases we could actually achieve RMSE values below two percent, which were among the best we could ever achieve. When we conducted the cross check of the patterns, imaging them in the respective other path, we could reliably achieve a RMSE value between 4.5 and 5.5% in some cases even below 4% (see Figure 30).

Although this is still not a precise match, we took this value as our benchmark which we set out to achieve with the microscope as well. It is entirely possible that even a small deviation in the optical setups of one path compared to the other can cause a RMSE mismatch of a few percent. We concluded thus that to precisely match the optimisation result from the transmission path in the reflection path, it is not as important that the setups are both individually perfectly aligned regarding distance of the components or tilt of the objective, but rather that small deviation in one path are copied in the other to ensure they will yield the same result. This is not feasible nor desirable and thus we took our benchmark and moved on to including the two inch PBS cube with a half waveplate in front of it as well as our microscope back into the setup.

This time we first turned the half waveplate such that maximum intensity is reflected and minimum intensity is transmitted through the cube as it should be in the final setup. We ran the optimisation, saved and checked the optimised DMD pattern in the reflection arm. We once more could observe a steep gradient in intensity across the square amounting to about 15% RMSE. We then turned the waveplate by  $45^\circ$  such that the intensity distribution through the cube was now inverted, while continuing to display the same pattern. The results can be observed in Figure 31. We could observe a decently well optimised pattern in the reflection axis with an RMSE very close to our target value, while in transmission we would observe the gradient distribution.

While the measurements from 27 already indicated it, we could now much more clearly see

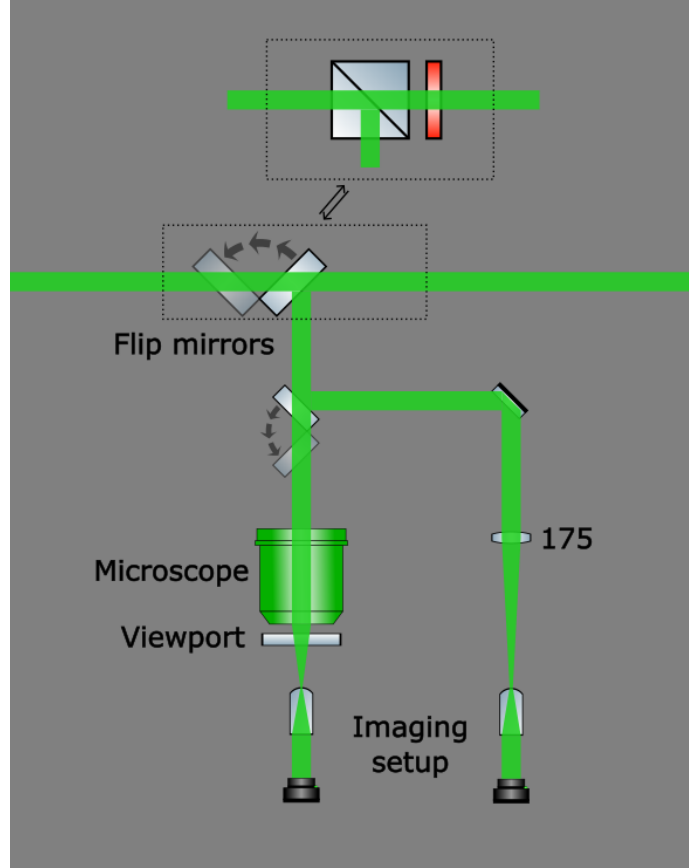


Figure 29: Reflection path with the third arm analogue to transmission path (not to scale).

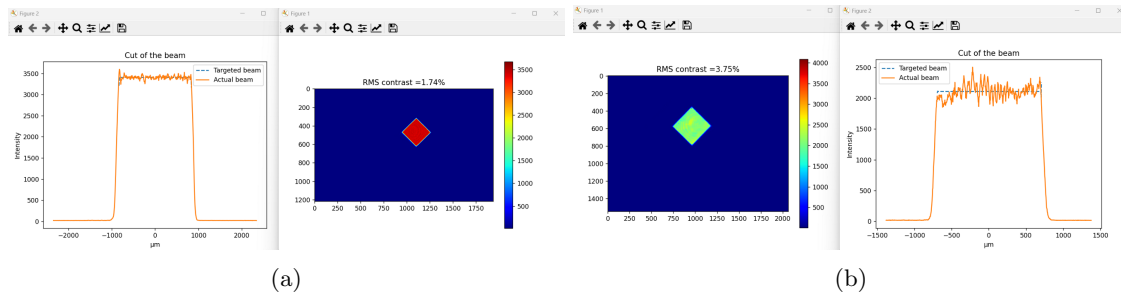


Figure 30: (a) The optimisation result including a 1D cut through the centre of the beam in the transmission arm. (b) The same pattern imaged in the reflection arm mirroring the transmission arm.

how the problem was related to the polarization. Although we cleaned the polarization of our beam right after the fibre, the DMD grid itself probably reintroduces some polarization aberrations into the beam, such that the polarization is not uniform across the beam. Then, when the part which is transmitted through the cube is optimised, the optimisation routine compensates the non-uniformity of the transmitted beam while exalting that of the reflected beam. We concluded that it may be best to pick up our beam for the reflection path in a way that is not polarization dependent. Still we also built in another cube with half-waveplates to clean the polarization right after the DMD.

We eventually decided to use a 90/10 two-inch beam sampler to pick up light for the reflection path. The light on which we run the optimisation passes through another beam sampler where 99% of the light is dumped. This is because the optimisation routine needs only very little power to operate well compared to the amount of power we plan to project onto the atoms. Upon installing the beam sampler at the position previously occupied by the cube, at first the discrepancy between the two arms immediately got worse again. Another round of careful alignment of the objective was necessary. Ultimately though, we managed to get the RMSE from both arms within four, sometimes even three percent of each other. However, it should be noted that the RMSE in reflection does not exactly follow the RMSE achieved during optimisation with a fixed offset.

Ultimately, as can also be seen in Figure 31, we managed to reliably achieve an RMSE of below 2% through our light based optimisation routine in the transmission arm and managed to image the same pattern with an RMSE of around 5% in the reflection path, using beam sampler to pick up part of the beam towards our microscope objective.

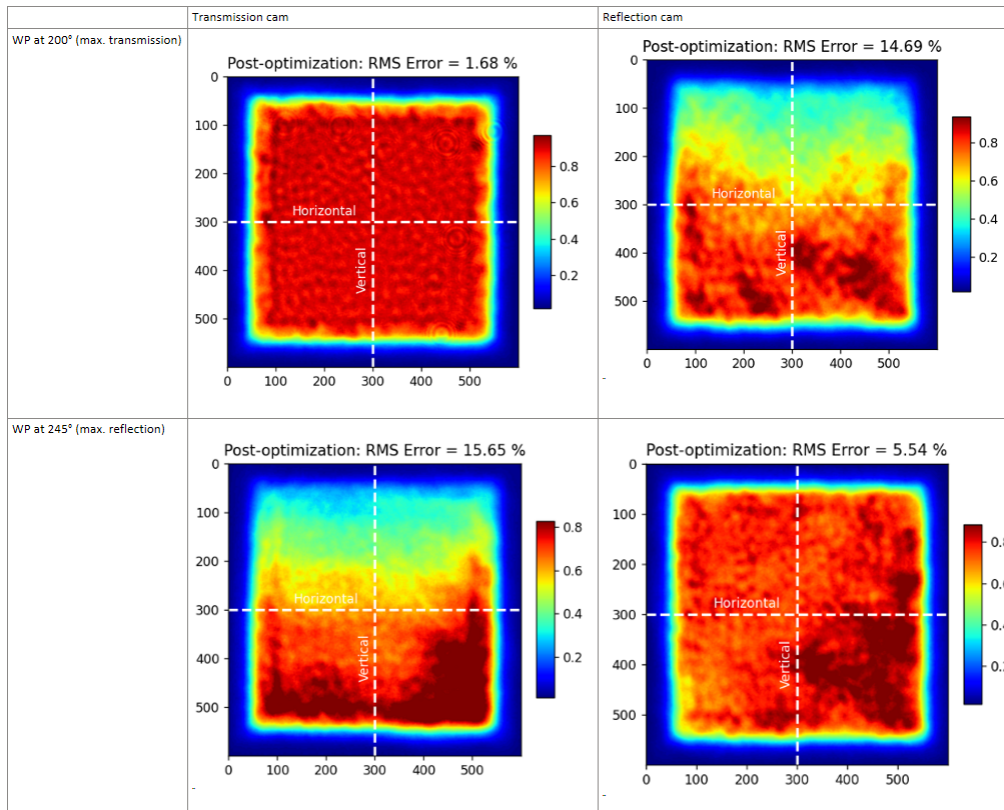


Figure 31: In the top left, the optimisation result from the transmission path, right the same pattern in the reflection path when the waveplate is fixed. In the lower images, the waveplate is turned by 45° degrees. The intensity distributions are now switched. We measure in the reflection path a flatness reasonably close to what we set our target to.

## 6 Optimisation algorithms

Simply displaying the intensity distribution we want our beam to have as a greyscaled pattern on the DMD is unfortunately not sufficient for a variety of reasons. The most obvious one, which was also already mentioned before is that our illuminating beam has an inhomogeneous Gaussian intensity distribution and thus whatever pattern we display will be convolved with this distribution. On top of that imperfections of the DMD grid itself and the optical setup afterwards will introduce aberrations which need to be compensated. To do this, we implement an iterative optimisation routine, aimed at generating a DMD pattern which when displayed produces a beam of the desired shape.

During our efforts to create and optimise arbitrary light-based potentials with the DMD, we employed two optimisation algorithms with different approaches to compensate for the intensity irregularities present in the captured images. The first one we are about to discuss was first developed by Thibault Bourgeois in our own group [7]. It is loosely based on [42], though in the case of ref. [42], there is only one 4f setup and the magnification factor is close to one. The idea of the first algorithm is to filter out high frequency components out of the Fourier transform of a captured image by means of a low pass filter. The filtered image is then transformed back to real space and used to calculate a correction to be applied to the DMD pattern on display. We will call this algorithm the filtering algorithm. The second algorithm we tested out was developed by Marcel Kern from the potassium-BEC group at the Kirchhoff Institute for physics (KIP) [37]. It takes a more local approach, where for each pixel of a captured image it evaluates whether it is too light or too dark and gives it a certain error. Image pixels are mapped to DMD pixels. The larger error of a pixel the more likely it is, that the corresponding micromirror will be flipped for the next iteration of the DMD pattern. We will call the second algorithm the errormap algorithm. In the following chapters we will go more in depth on the operation of both algorithms and their peculiarities. A complete summarizing overview over the optimisation operation for both algorithms is shown in 4.

### 6.1 Filtering optimisation

An overview of the functionality of the filtering algorithm can be found in Thibault's thesis [7]. The following description will include recent changes and adaptations and go a little more in depth on the working principle.

The working principle of our filtering algorithm is schematized in 4. One iteration is also illustrated in Figure 32. In the beginning we define a target image  $T(x, y)$  (Figure 32 (a)). This target image is typically an 8-bit image which is then dithered as described in 4.3.3. The image is then displayed on the DMD grid, we call this initial DMD pattern  $P_0(x, y)$  (Figure 32 (b)). The DMD pattern is then iteratively updated by the algorithm to  $P_n(x, y)$  at the  $n$ th iteration. The iteration works as follows.

Once an image is captured with the camera we use for the optimisation (Figure 32 (c)), the image undergoes the appropriate calibration. The way this calibration works is detailed in section 7.3.2. The calibration maps the captured image onto the displayed DMD pattern. Next we calculate the RMSE value of the image. A detailed report on the calculation can be found in section 6.4.1. The RMSE in this case only serves as our measure to determine whether a newly corrected pattern marks an improvement to the previous one and should be kept or whether it does not show any improvement and should be discarded.

The correction to be applied to the recorded pattern is calculated as follows. The remapped image  $I(x, y)$  is transformed into Fourier space and denoted  $I(k_x, k_y)$  with  $k_x, k_y$  the spatial frequencies.

Then a second order low-pass filter is applied to the Fourier image:

$$I_{\text{lp}}(k_x, k_y) = \frac{I(k_x, k_y)}{1 + \left(\frac{k_x}{f_c}\right)^2 + \left(\frac{k_y}{f_c}\right)^2} \quad (6.58)$$

Here  $f_c$  is the cut-off frequency above which the spatial frequencies are damped by the low-pass

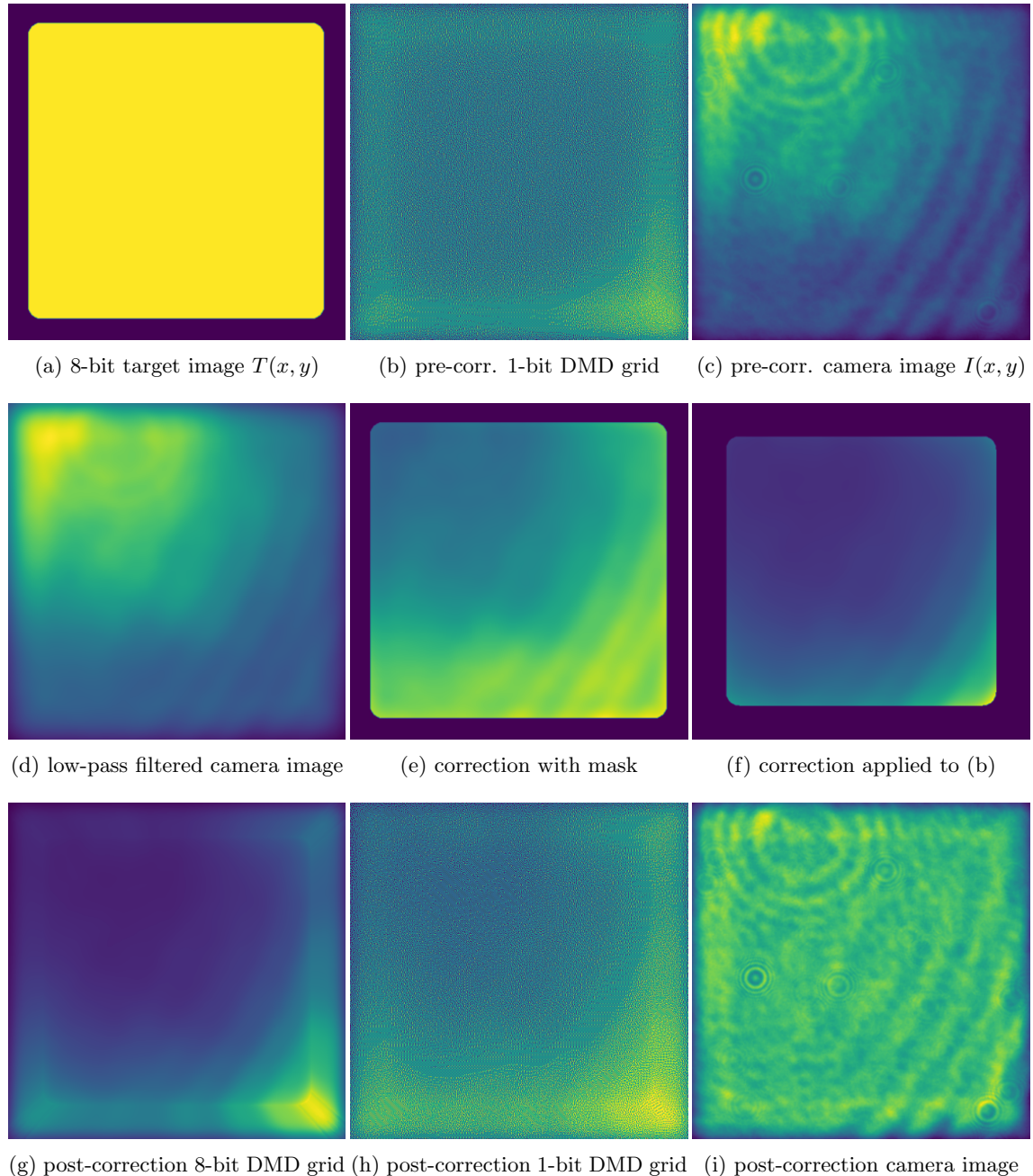


Figure 32: One exemplary iteration of the filtering algorithm. In the top row the starting situation is seen, (a) the target  $T(x, y)$ , (b) the 1-bit grid we display with the DMD  $P_n(x, y)$ , (c) the resulting camera image. (d) The low-pass filtered image  $\tilde{I}_{\text{lp}}(x, y)$ , (e) the correction to be applied to (b), (f) the correction applied. In (g) smooth borders are added, (h) the dithered new DMD pattern  $P_{n+1}(x, y)$ , (i) the camera image is improved regarding its overall flatness. To flatten also the higher frequency fringes visible in (i) the cut-off frequency of the low-pass filter has to be increased which will happen once the algorithm detects no further improvement with the lower cut-off frequency.

filter. The initial value of the cut-off frequency can be adapted depending on the image that should

be optimised. We found that it makes sense to start with a cut-off frequency roughly corresponding to the size of the displayed pattern. The filtered image is transformed back to real space and renormalized ( $\tilde{I}_p(x, y)$  in Figure 32 (d)).

The correction to be applied to the DMD pattern is the target divided by the filtered image 6.59 . In order to avoid dividing by zero the correction is set to zero for pixels with a vanishingly small value after filtering (see Figure 32 (e)).

$$\epsilon(x, y) = \begin{cases} \frac{T(x, y)}{\tilde{I}_p(x, y)} & \text{if } \tilde{I}_p(x, y) \geq 0.1 \\ 0 & \text{if } \tilde{I}_p(x, y) < 0.1 \end{cases} \quad (6.59)$$

The correction is multiplied with the latest DMD pattern. Wherever the correction was set to one the pixel will be filled with the value from the previous DMD pattern  $P_n(x, y)$ . Ultimately the new pattern is once more masked with a mask  $H(x, y)$  typically equivalent to our target pattern, thus all pixels outside of our target pattern are set to zero, while all others are not changed (Figure 32 (f)).

$$P_{n+1}(x, y) = \begin{cases} \epsilon(x, y)H(x, y)P_n(x, y) & \text{for } \epsilon(x, y) > 0 \\ H(x, y)P_n(x, y) & \text{for } \epsilon(x, y) = 0 \end{cases} \quad (6.60)$$

Here  $P_{n+1}(x, y)$  is our new corrected 8-bit DMD pattern, typically before dithering it we introduce a step to smoothen the borders of the pattern (see Figure 32 (g))6.3. The corrected pattern then is dithered with Floyd-Steinberg dithering (Figure 32 (h)) 4.3.3 and the new optimised pattern is displayed on the DMD and imaged again (Figure 32 (i)).

The *RMSE* value from this new camera image created by corrected new pattern compared to the target is calculated. If it is smaller than the value from the previous iteration, the new pattern is accepted as the new 'best' pattern. If the *RMSE* is the same or larger than previously, the pattern is rejected and the old pattern is used again in the next iteration, but the cut-off frequency is doubled ( $f_{c, n+1} = 2f_{c, n}$ ) to allow finer structures to be resolved. The effect is depicted in Figure 33. The images are from the same optimisation run, but a few iterations later, the cutoff frequency was increased in order to compensate more detailed intensity variations corresponding to higher spatial frequencies. As can be seen in 33 (b) and (c), more detailed features are visible in the low-pass filtered camera image and the subsequent corrected DMD pattern. In the resulting camera image (33 (d)) we can see that fine aberrations are compensated compared to 33 (a).

The algorithm only stops (assuming no unexpected software or hardware error) after a fixed amount of iterations to be set in the beginning or when it is manually interrupted. We found that after the 15th iteration there is usually little to no improvement. In fact if we already reached the best achievable *RMSE* mark for this run but we force the algorithm to carry on, it will keep failing and doubling the cut-off frequency every time, leading to a drastic increase in  $f_c$  allowing high frequency intensity noise to enter into the pattern, which in turn leads to a worse *RMSE* value and continues the cycle. The exact amount of iterations necessary to reach the best *RMSE* value achievable in this run is difficult to predict. The way the algorithm is currently operated, the DMD pattern from every iteration is saved. Once the optimisation is finished the lowest achieved *RMSE* value is indicated and the pattern from the corresponding iteration can be selected.

## 6.2 Errormap optimisation

The errormap algorithm was adapted from Marcel Kern and details on its development and functionality can be found in his thesis [37]. It should be noted that in the Potassium BEC experiment

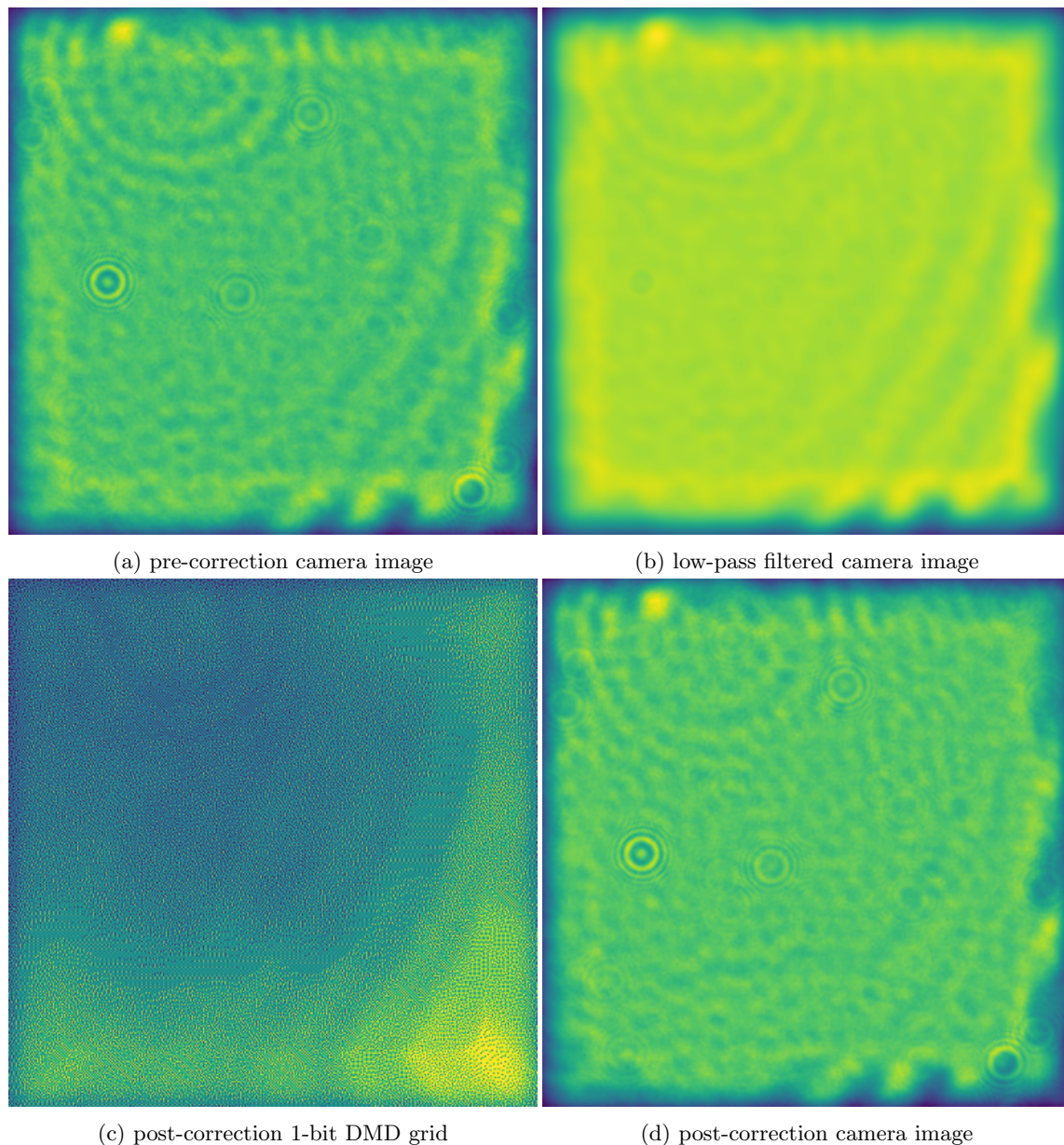


Figure 33: Images from the same optimisation run as Figure 32, but a few iterations later. (a) Camera image before correction, (b) low-pass filtered image, (c) corrected and dithered DMD pattern, (d) camera image after correction.

at the KIP in which this algorithm was developed, the DMD is operated with blue-detuned light, so atoms will be trapped in low intensity regions in contrast to our case (see 3.2. While this might affect the suitability to our case this should not restrict the algorithm's general functionality.

As can be seen in 4 the first few steps of the filtering algorithm and the errormap algorithm are identical or analogue. In the beginning we define a target  $T(x, y)$ , the dithered version of which serves as our initial DMD pattern  $P_0(x, y)$ . This pattern is then again iteratively optimised. The only way the errormap algorithm is really different is the way that  $P_{n+1}(x, y)$  is calculated from  $P_n(x, y)$ .

Like with the filtering algorithm, an image which was formed through the display of a pattern  $P_n(x, y)$  on the DMD (34 (a)) and is captured with the camera undergoes calibration resulting in the image grid  $I(x, y)$  (34 (b)), which can be directly overlaid with a virtual DMD grid. Next the

errormap  $E(x, y)$  is calculated (34 (c)):

$$E(x, y) = \alpha \frac{I(x, y) - T(x, y)}{I_{max}} \quad (6.61)$$

Here  $I_{max}$  is a parameter to set the maximum intensity level of the target image. It is an integer value between 0 and 255 and can be set in the beginning. In the case of a flat top structure, the maximum intensity corresponds to the plateau intensity of the flat top. The target image in this case was already adjusted to  $I_{max}$ . In the calculation of the errormap it serves as a normalization.  $\alpha$  is a parameter also to be set before the optimisation starts. It can adjust the speed of the optimisation process as mirrors will ultimately be flipped with certain probability depending on their error value. An  $\alpha$  value above one will increase this value and increase the probability with which a mirror is flipped, an  $\alpha$  value smaller than one can do the opposite. We have found that  $\alpha > 1$  can also introduce high frequency noise into the pattern. Also if entire regions are too light or too dark, a large  $\alpha$  will lead to a large fraction of this region being flipped which in turn leads to this region being too dark or too light respectively. During an optimisation run with a large  $\alpha$  the pattern therefore may tend to flip flop back and forth for a while before converging [37]. Choosing a smaller alpha leads to a slow but steady one-sided progression towards the target intensity. Depending on the laser power and the exposure time of the camera the ideal  $\alpha$  may also vary. In our case we settled on  $\alpha = 0.6$ .

As a next step in the optimisation routine, a two-dimensional grid  $\eta(x, y)$  with dimensions matching those of the DMD is created and filled with random values drawn from a uniform distribution between 0 and 1.

$$\eta(x, y) \stackrel{\text{dist}}{\sim} \mathcal{U}(0, 1), \forall (x, y) \in \{1, \dots, 2560\} \times \{1, \dots, 1600\} \quad (6.62)$$

Via this grid it is ensured that the algorithm will not try to correct every pixel immediately and thus flip nearly all pixels which would just create the same pattern but inverted. A combination of two conditions in the form of matrices  $C_1(x, y)$  and  $C_2(x, y)$  is applied to determine if a mirror is to be flipped to create the new corrected DMD pattern  $P_{n+1}(x, y)$ . The matrix  $C_1(x, y)$  is defined by comparing the errormap and the random matrix. Each pixel is given a boolean value depending on whether  $\eta(x, y)$  or  $|E(x, y)|$  is greater for this pixel (34 (d)).

$$C_1(x, y) = \begin{cases} 1 & \text{if } |E(x, y)| > \eta(x, y) \\ 0 & \text{if } |E(x, y)| < \eta(x, y) \end{cases} \quad (6.63)$$

$C_1(x, y)$  is supposed to ensure that only pixels with a large error are preferably corrected, but at the same time correction is somewhat randomly diffused over the whole grid. The matrix  $C_2(x, y)$  is constructed by comparing the values of the modified previous DMD pattern,  $P_{n,mod}(x, y)$ , to the errormap value. The previous DMD pattern is slightly modified such that all pixels which are off are assigned the value -1 instead of 0. Now if the error of a pixel  $(x, y)$  is positive (i.e. the pixel is too bright) and the corresponding micromirror was previously on, the check  $C_2(x, y)$  is 1. Reversely, if the error on a pixel is negative (i.e. the pixel is too dark) and the corresponding micromirror was previously off,  $C_2(x, y)$  is also 1. It is 0 in any other case (34 (e)).

$$C_2(x, y) = \begin{cases} 1 & \text{if } \text{sign}(E(x, y))P_{n,mod}(x, y) > 0 \\ 0 & \text{if } \text{sign}(E(x, y))P_{n,mod}(x, y) < 0 \end{cases} \quad (6.64)$$

Note that to modify the algorithm for the case of a repulsive trap, one would only have to reverse the cases of this equation.

Both  $C_1(x, y)$  and  $C_2(x, y)$  and optionally also an additional mask  $H(x, y)$ , typically equivalent to the target  $T(x, y)$ , are combined with a logical "AND" gate and a flip map  $F(x, y)$  is created. A pixel is only selected to be flipped if its value is one or "True" in all of the three grids (34 (f)).

$$F(x, y) = C_1(x, y) * C_2(x, y) * M(x, y) \quad (6.65)$$

This flip map is added to the old DMD pattern in the base-2 numeral system, such that for those pixels selected for flipping a zero in the old DMD pattern is converted to a one and a one to a zero. The result is the new DMD pattern  $P_{n+1}(x, y)$ .

$$P_{n+1}(x, y) = P_n(x, y) + F(x, y) \quad (6.66)$$

The process is repeated for a fixed number of iterations set in the beginning. Like the filtering algorithm, it will not stop before this number is reached unless it is manually interrupted.

At every iteration the overall number of flipped mirrors, the average error and the standard deviation of the error are calculated and tracked. Average and standard deviation are directly calculated from the errormap as  $\mu(E(x, y)/\alpha)$  and  $\sigma(E(x, y)/\alpha)$ . After the optimisation is finished the RMSE for every single iteration can also be calculated separately in the same way as for the filtering algorithm.

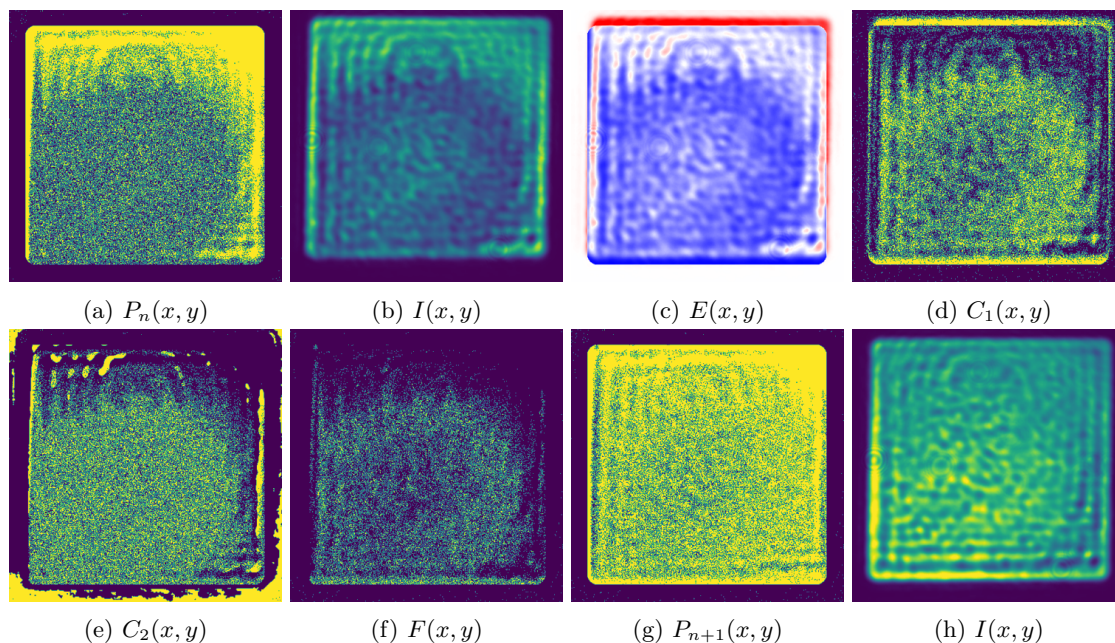


Figure 34: One exemplary iteration of the errormap algorithm (with the same target as in Figure 32 (a)). (a) 1-bit DMD grid which was used to produce the pattern captured in (b). (c) errormap calculated from the camera image, blue means 'too dark' and red means 'too light'. (d)  $C_1(x, y)$  grid, (e)  $C_2(x, y)$  grid, (f)  $F(x, y)$ . (g) Shows the new 1-bit DMD grid  $P_{n+1}(x, y)$  and (h) the respective camera image.

	Step	Filtering Algorithm	Errormap Algorithm	
Preparation	<b>Initialization</b>	Set Parameters and create Directories $f_c$ , border parameters	$\alpha$ , $I_{max}$ , border parameters	
	<b>Calibration sequence (optional)</b>	Load Calibration Pattern Capture Image Extract Transformation Parameters		
	<b>Target selection</b>	Load latest Calibration Parameters		
		Select 8-bit reference image		
Select custom mask (optional)				
Iteration	<b>Image acquisition</b>	Calculate initial 1-bit DMD pattern		
		Display latest DMD pattern Capture image Apply affine transformation		
	<b>optimisation</b>	Calculate RMSE and adapt $f_c$	Create errormap	
		Calculate low-pass image and correction	Determine mirrors to be flipped	
		Calculate new corrected DMD pattern	Create new DMD Pattern	
	Add smooth borders and dither			

Table 4: A flow diagram of the full optimisation routine. As can be seen for most steps, filtering and errormap algorithm are identical. It is only during the actual iteration loop that the two approaches differ in the way the next iteration is calculated. During the optimisation sequence, the lower section labelled 'Iteration' is the part which loops for a fixed number of times.

### 6.2.1 Implementation and adaptation

During the development of the errormap algorithm by Marcel and during the light-based trials, the progress and quality of the optimisation was tracked mainly by average and standard deviation of  $E(x, y)$  and number of flipped mirrors among other things. In the tests at the KIP, the number of mirrors flipped would usually start at around 110000 in the first iteration and would rather quickly converge towards 20000 while the average converged towards an absolute value of 0.004 and the standard deviation towards 0.05. All these numbers were achieved with a gradient annulus as the target pattern. The gradient annulus is a slightly more complex pattern than the flat top square we used during tests of the filtering algorithm. It is a ring of variable size and width and an intensity gradient around its circumference as it is shown in Figure 35. The maximum intensity can be set by  $I_{max}$ . The intensity will gradually decrease along the circumference.

When trying to implement the errormap algorithm with our own DMD setup, we also tried out the gradient annulus as well as flat top patterns (e.g. in Figure 37. The first results though left us rather confused. We tried out a gradient annulus with an outer diameter of 400 pixels, an inner diameter of 200 pixels and for now  $I_{max} = 255$ . During the optimisation one could observe the

average, the standard deviation and the number of flipped mirrors in real time. We observed how the algorithm quickly achieved an average value of  $\mu < 0.001$  and  $\sigma < 0.02$  with around 30000-40000 flipped mirrors per iteration (see Figure 36 (b)).

However as the optimisation progressed the number of flipped mirrors decreased further while average and standard deviation tended to rise again, which seemed strange to say the least and was not observed during trials at the KIP. Still at first glance, the numbers seemed to speak for a very good result, however the actual camera images of the gradient annulus showed some high frequency ripples, mainly parallel to the border. They were present in every iteration and did not visibly move around (see Figure 37, centre row). Additionally there were some even higher frequency ripples with seemingly random orientation, which did move around, change direction and shape and also appear and disappear randomly. We also tried the errormap optimisation for our square pattern. Also here we achieved decent and this time more linearly progressing values for average and standard deviation (see Figure 36 (a)), but we could also observe the same strange phenomenon as just described and in addition some flip-flopping behaviour of a large region of the pattern as described in 6.2 (see Figure 37, top row).



Figure 35: Gradient annulus 8-bit image

From [37] we know of a phenomenon that fits the description of the latter rather well. So-called

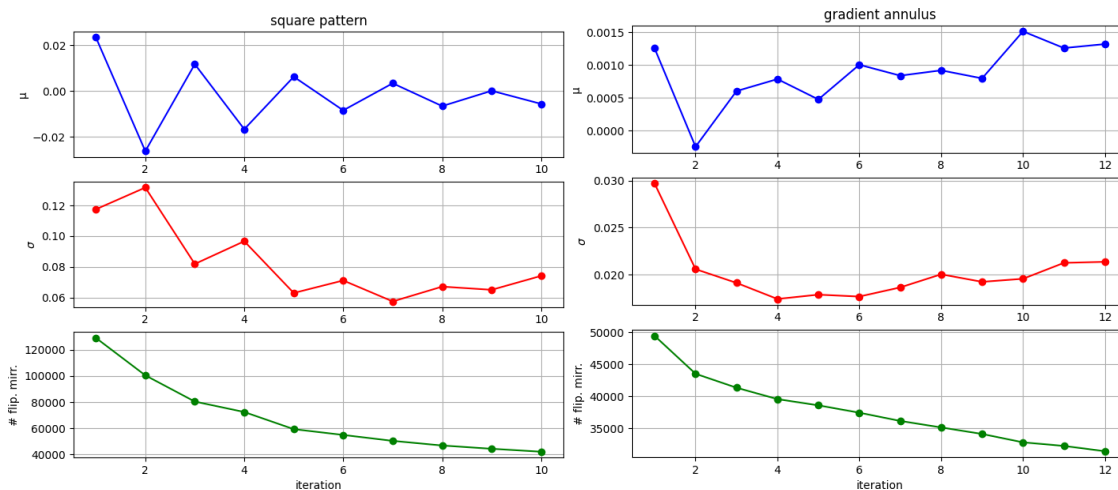


Figure 36: (a) development of average, standard deviation and number of flipped mirrors over little more than 10 iterations in the case of a square pattern. (b) the same in the case of a gradient annulus

'Dunes' may appear in the DMD pattern if the pointing of the laser beam shifts from one image to the next. If this happens, the calibration transforms the image such that it does not exactly overlap with the DMD pattern and the algorithm tries to correct an error detected in the image by flipping pixels at the same position in the pattern, although the position in the pattern is not actually the

same as the error's position in the image. This not only leaves the error still present in the next image but also creates new errors. However we had no explanation for the first kind of ripples. We carried on to try out different patterns such as flat top circles or squares. The stationary kind of ripples would continuously appear. They would always appear parallel to the border, similar to the kind of ripples expected from the Gibbs-phenomenon [8] but with every iteration they would also advance further into the shape and even increase in contrast. This could not be explained by random shifts of the laser pointing alone. However to confidently exclude this, we made a test run where we would artificially introduce a random shift in  $x$  and  $y$  direction at every iteration (37, bottom row). As a result we could clearly observe that this shift introduced 'Dunes' into the pattern exactly as described in Marcel's thesis [37]. The dunes in the images would, similar to sand dunes, wander around, change shape, appear and disappear randomly and not be parallel to the border. The camera images from two exemplary optimisation runs exhibiting the described phenomena can be seen in 37.

We then continued to analyse the stationary ripples further and made two more observations.

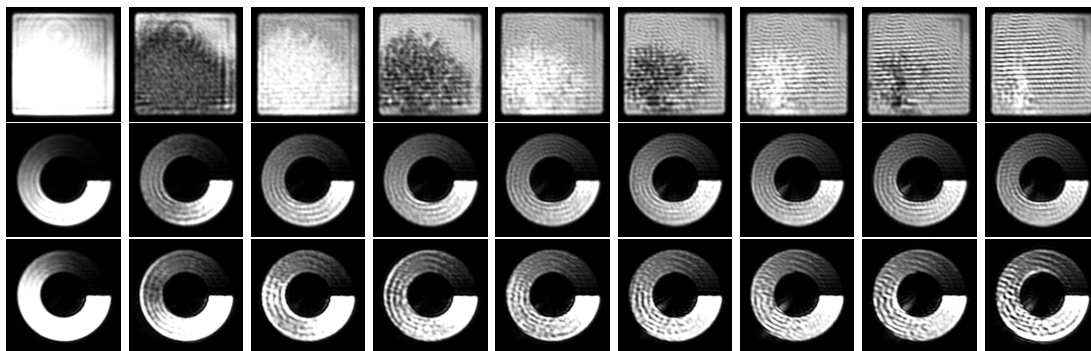


Figure 37: Camera images of the first 10 iterations from different runs using the errormap algorithm. Top row: a run with a flat top square pattern. One can observe the previously described flip-flop phenomenon, which occurs when  $\alpha$  is a little too high. Centre row, optimisation on a gradient annulus. The stationary fringes which form parallel to the border, in this case horizontally, are clearly visible in the first to rows. Bottom row: optimisation on a gradient annulus, but in this case the calibration was artificially manipulated to add random deviations in the  $x$  and  $y$  position of the image, producing a different kind of ripples which appeared in random orientations and moved around. A superposition of the two kinds of ripples can be observed.

When overlaying the camera image and the DMD pattern for the case of a square where the stationary ripples had already filled nearly the whole area of the square, we observed, that the light and dark stripes of the image  $I(x, y)$  and the DMD pattern  $P_n(x, y)$  did not match. The light part of the image laid in a dark part of the pattern and vice-versa as can be seen in Figure 39. We additionally observed, that in some camera images there would be a bright stripe right next and parallel to the border. This bright stripe appeared since in the previous errormap the region was marked as much too dark which is in turn likely due to a random shift of the laser pointing in the direction perpendicular to the border (see Figure 40). Thus when image and pattern were overlaid one edge would reach out of the target mask and this part would be detected as too bright as it was much brighter than the background while the opposite edge was too dark. The compensation efforts of the algorithm then created a bright border wall on one side, which in the following iterations would not slowly be smoothed out but rather contribute to forming the stationary ripples. This effect together with ringing effects due to the Gibbs-phenomenon (4.2) probably explains the why the stripes we observe are oriented parallel to the border. The fact that the stripes in the image and on the virtual DMD grid do not overlap even after calibration explains why they are not

compensated but manifest themselves over time. If  $I(x, y)$  and  $P_n(x, y)$  overlapped perfectly, the algorithm should have no problem in compensating stripes no matter where they originate from. The offset between  $I(x, y)$  and  $P_n(x, y)$  we see in Figure 39 might hint to a global systematic drift of the laser pointing in one direction over time, however in that case we should be able to observe the width of the stripes change after a while or they should disappear after we run the calibration again and update the transformation parameters. Neither is the case. We concluded that it is more likely that a batch of light in one area of the image can simply not be traced back to exactly the same area on the DMD surface. In the case of ringing for example stripes appear parallel to the border, even though there are no stripes present in the DMD pattern, since the ringing is caused by the sharp border. If the algorithm now tries to compensate this in the pattern, areas of the pattern will be modified which are however not responsible for the ringing in the first place, potentially leading to a continuation of ringing further into the pattern. In addition over the whole optical setup, there are plenty of possibilities where aberrations may distort the pattern or real space images are constructed from a finite number of Fourier constituents. Furthermore in addition to a translation or a rotation this may perhaps also manifest itself in an inhomogeneous shearing of the pattern, which is technically possible to track with the calibration, but may also be picked up as a rotation in the 2D projection of the wavefront. According to the calibration parameters there was little to no shear present at any times.

We tried to separate the problems we encountered and described above with regard to their source and came up with the following list and possible solutions:

- 1. Ringing: Due to the Gibbs phenomenon 4.2 in Fourier analysis, some ripples are created near and parallel to the border. It is most prominent in the first image of an iteration run for a uniform potential when all mirrors inside the shape are switched on and the contrast from dark to light patches is maximum (see Figure 38). To solve this we could implement some smooth borders in the errormap optimisation as well.
- 2. Systematic spatial offset: As described above, we observed an offset of the dark and light stripes position in the camera image compared to the DMD pattern. Either this is due to some shift in the pointing of the laser beam, or it has to do with the way the light is diffracted and refracted through the setup (see Figure 39). As running the calibration more frequently does not seem to solve this issue, to counteract this effect we could think of about applying a smoothening filter to the DMD pattern to counteract stripe formations.
- 3. Random spatial shifts: While we can not observe systematic shifts of the beam pointing in one direction, the errormaps for some iterations suggest, that there may be random shifts of the laser pointing in between iterations. They can be the source of stripes forming near the edges of a pattern which in turn contributes to development of stripes all over (see Figure 40). Additionally random shifts can produce 'Dunes'. We will have to find out what is the cause for these shifts in the main experimental setup environment. Though also here a combination of smooth borders and an overall smoothening filter could potentially reduce the impact of random shifts.
- 4.  $I_{max}$  settings: Although this is only a minor problem and easy to fix, it may contribute to stripe formation. The  $I_{max}$  setting or the exposure time of the camera has to be adjusted accordingly, so that the algorithm has some space to try to clear the pattern of intensity variations. Otherwise, if the whole pattern is too dark from the beginning, a uniform pattern will simply not change and maintain the ringing effect from point 1.) and a gradient pattern will slowly become more uniform, while also carrying ringing artifacts with it (see Figure 41).

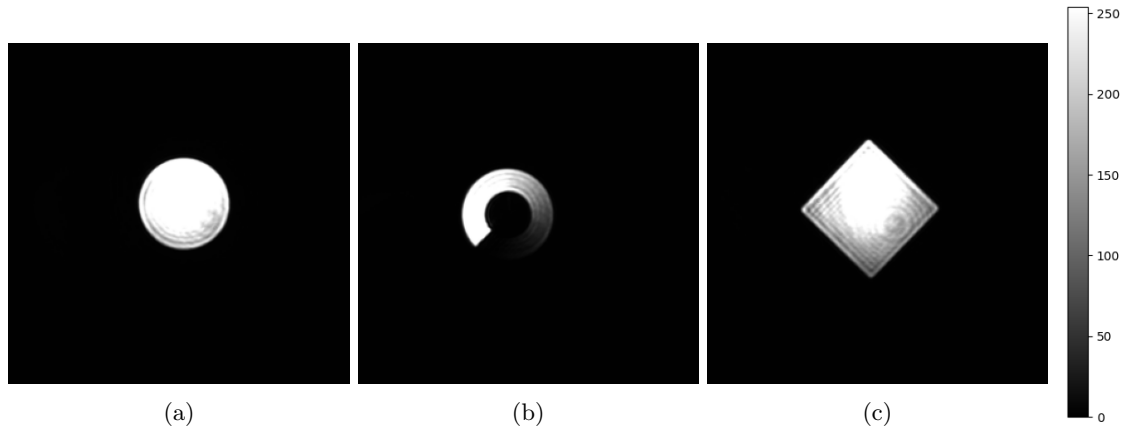


Figure 38: Ringing: Different shapes, where the ringing effect near the edges is visible. (a) circle, (b) gradient annulus, (c) square.

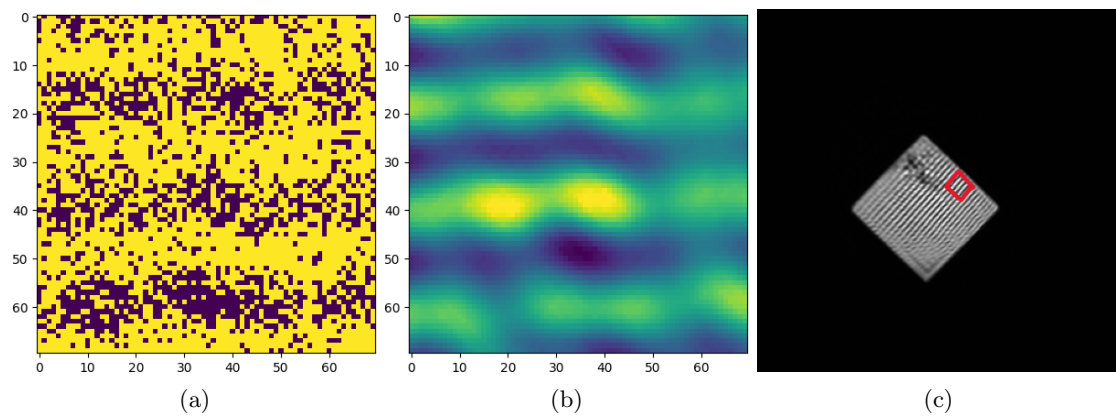


Figure 39: Systematic spatial offset: (a), A cutout of the DMD pattern, centre, the same cutout from the camera image. Bright yellow correspond to bright and 'on' pixels respectively, dark blue to dark or 'off' pixels. (c), The full camera image with stripes on the pattern and a red square to indicate the approximate region from where (a) and (b) are taken.

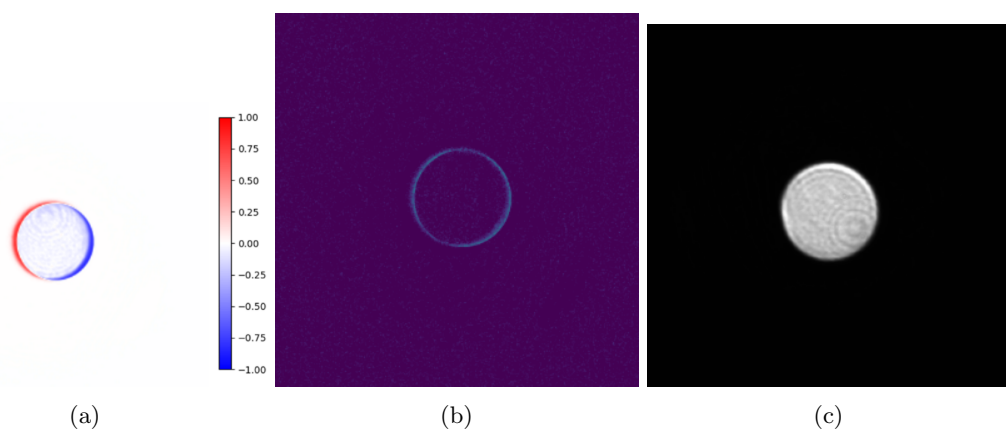


Figure 40: Random spatial shift: (a), an error map  $E(x, y)$  of a uniform circle indicating a shift to the left (red means too bright, blue too dark in reference to the target), (b), the mirror flip map  $F(x, y)$  indicating that almost exclusively mirrors on the edge are flipped in this iteration, (c) the camera image  $I(x, y)$  of the resulting pattern

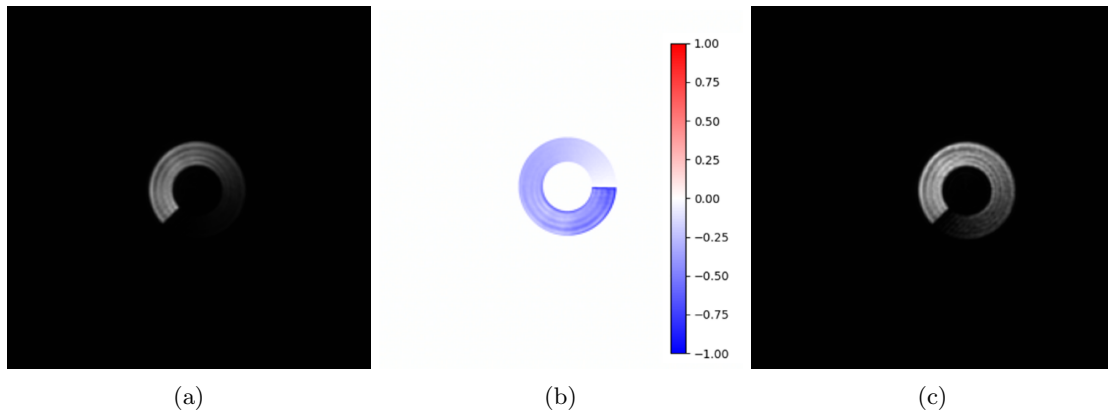


Figure 41:  $I_{max}$  settings: (a), Initial image of a gradient annulus, (b), the corresponding errormap indicating the image is overall too dark, (c), the optimised image with ringing artifacts from the first image still present. Note that in the calibration, the camera image is always rotated by  $135^\circ$  counter-clockwise.

Ultimately, what we observe is probably a combination of all four. Though it is probably a good idea to try to implement smooth borders for the errormap algorithm as well as a global filter to diffuse the correctional mirror flip map to prevent stripe formation.

### 6.3 Smooth borders

In the previous section we concluded, that a way to counter many of the issues we described by manipulating the algorithm software only may be to include a step to add smooth borders around patterns with sharp edges and maybe also add a step in which the correction itself, i.e. the flip map is a little more diffused across the whole pattern. In this section we will present a few different approaches on doing that. On the one hand we can manipulate the target pattern itself, such that sharp edges and ringing does not appear in the first place, on the other hand we may introduce a smoothing step during the errormap algorithm.

#### 6.3.1 Target manipulation

A way of adding smooth border to the corrected pattern  $P_{n+1}(x, y)$  during one iteration was already implemented in the filtering algorithm with the aim of counteracting the ringing effect resulting from the Gibbs phenomenon. In that case, a padding with a fixed width framing the shape of the uniform pattern was created. The intensity within the frame should smoothly fall off from the uniform intensity level of the pattern to the dark background. The smooth intensity transition should follow the following distribution[7]:

$$I = \frac{I_0}{1 + \left(\frac{r}{r_0}\right)^\beta} \quad (6.67)$$

Here  $I_0$  is the plateau intensity,  $r$  is the distance from the plateau in micromirrors and  $\beta$  and  $r_0$  are tunable parameters determining the shape of the function. While  $r_0$  is the characteristic border width and thus a large  $r_0$  will expand the border region and the length of the tails,  $\beta$  is the exponent of the border function and determines the steepness of the intensity descent. The larger  $\beta$  the steeper the descent. Additionally to these parameters, there is also a hard restriction to the

border size, which is the previously mentioned fixed width setting of the padding. Outside of the padding area, the previous shape will be maintained, even if this means that there will be hard cut-off of a tail which would expand further. This border smoothing routine has been applied to every corrected pattern in the filtering algorithm. During tests of the algorithm, the best *RMSE* values have been reached for  $(\alpha, r_0) = (6, 50)$ . We kept this setting throughout our tests also in the revised setup and could reach similar RMSE values.

It is important to note that in the filtering optimisation algorithm, the border smoothing is applied to and on the basis of the corrected pattern every iteration. This means that if the corrected pattern contains fringes near the border to compensate for aberrations, so will the border function. Also the border function is never a part of the target pattern. When optimised camera image and target pattern are compared to calculate the RMSE, the border region is disregarded.

Since we know that the shape of the border of an optical dipole potential plays a role in the degree of homogeneity of a dipolar Bose gas [35], we tried whether we could expand our level of control over the border shape a little further by implementing it already in the target image. Another problem of the smooth border function in the filtering algorithm is, that it has to be redefined for every shape, whether we work with a circle, a square or anything else, or even only adjust the size of our shape, the border parameters have to be rewritten to clip the padding to the shape at the right position.

We tried two new ways to implement a smooth border function in the errormap algorithm.

- Gaussian broadening** We dilate the shape of the target image and simply add a Gaussian blur to the border region only. Next the border and the initial image are recombined and weighted accordingly such that the two merged seamlessly with each other. The newly created image could now serve as the new target image. The intensity distribution at the border would follow a Gaussian distribution, the width of which can be controlled the input parameter  $\sigma$  which in this case serves as one of two control parameters setting the shape of the border. By changing  $\sigma$  the width of the region which is added in the dilation is adjusted automatically to prevent hard cut-offs. The second control parameter is only a quasi boolean entry to determine whether the kernel shape which is used to dilate the original shape is circular or rectangular. Depending on the pattern shape, one or the other will produce a more natural transition from background to shape (see Figure 42). This method is comparable to a simple Gaussian convolution of the target pattern, yet the border is clipped to the original structure in this intricate way to ensure that the original pattern remains completely intact for any chosen  $\sigma$ . This is not the case in the next method.

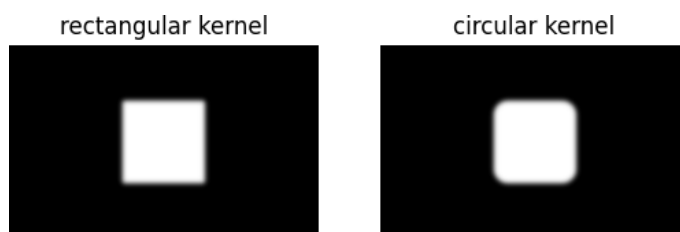


Figure 42: Comparison between a circular and rectangular kernel

- Sigmoid broadening** We tried is an adjustment of the original routine from the filtering algorithm described above, but applicable to any shape without the need to change parameters. The border function itself is very similar though (comp. 6.67). In this case the hard

borders in an image with arbitrary shapes are detected automatically. Once the border is detected, two new masks are created, one smoothly sculpting an increasing intensity distribution from the background up, the other one doing the opposite from the flat-top down. The exact shape of these distributions could technically be set to any arbitrary function. In our case we modelled the borders after a sigmoid:

$$I = \frac{I_0}{1 + e^{-kr}} \quad (6.68)$$

As in 6.67  $I_0$  is the uniform intensity level and  $r$  is the distance to the hard border in micromirrors.  $k$  in this case is the sharpness parameter, one of only two input parameters together with the border width. The routine will stretch or quench the sigmoid curve such that always the full border width is used without hard cut-offs. Other than the original filtering algorithm method and like the Gaussian broadening method the manipulated pattern will be used as a new target pattern. What is different in this case is, that typically also the original pattern will be modified during the addition of the smooth borders (see Figure 43). Furthermore as already mentioned, the border function can easily be modified to any arbitrary shape, for example also a Gaussian or a polynomial.

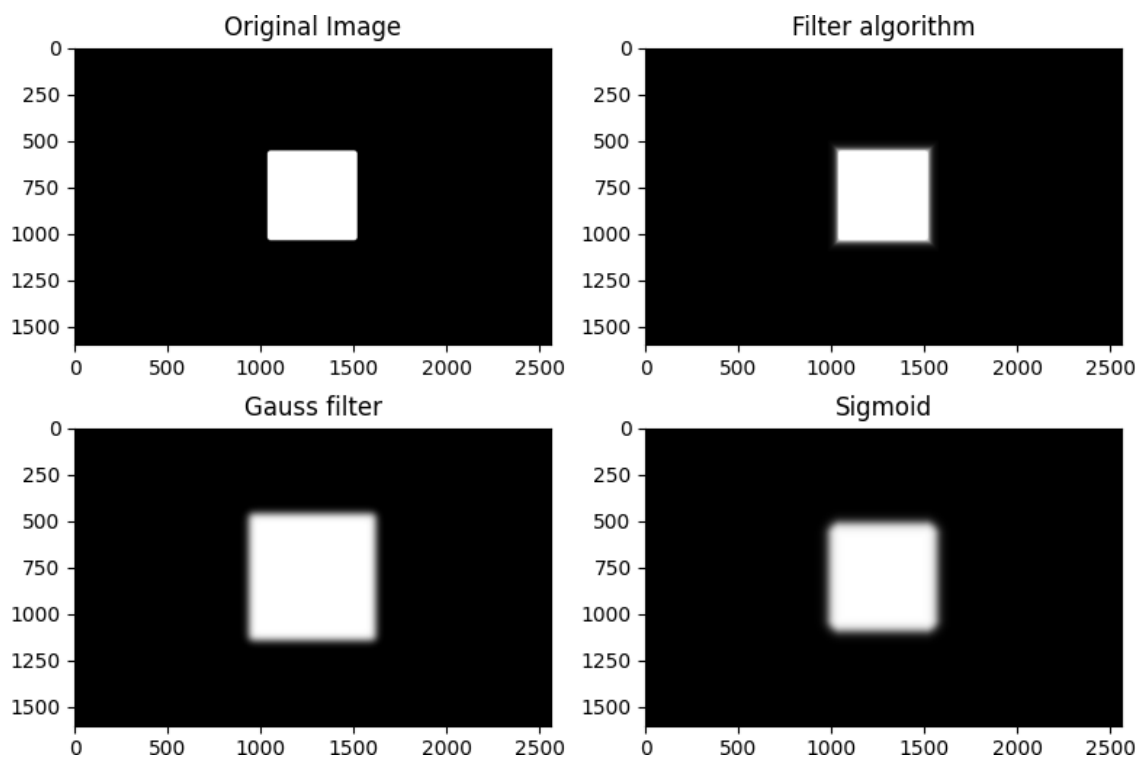


Figure 43: Comparison of the different border smoothing methods applied to a square pattern. Original image in the top left. Bottom left: Gaussian broadening, top right: Original border function from filtering algorithm, bottom right: Sigmoid broadening.

In the next step we applied our two different broadening methods to the target and ran the errormap optimisation routine on the modified target. Only the target image was modified and the rest of the optimisation remained the same. We tried out Gaussian broadening first.

We could quickly observed how the stationary fringes disappeared and the dunes dominated. This meant that the stationary fringes indeed originated from the border, through ringing and random

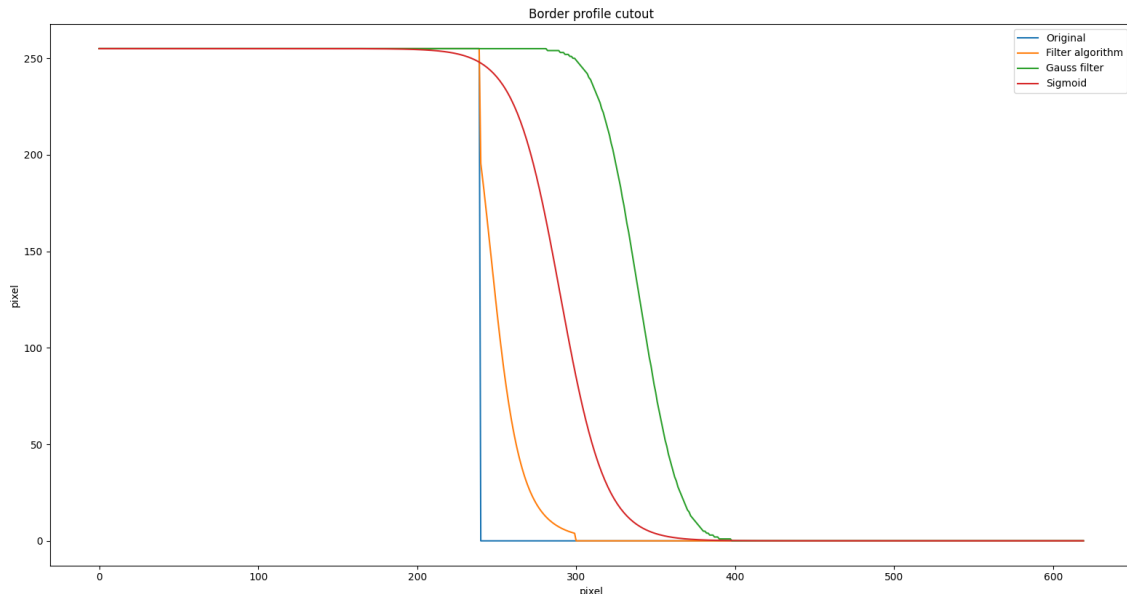


Figure 44: A cut through the middle of the smoothed patterns from 43. The border added in the filter algorithm has the parameters  $\beta = 6$ ,  $r_0 = 50$  and an overall border size limit of 50 pixels. The Gauss filtered border was constructed with a rectangular kernel and  $\sigma = 20$ . The sigmoid border has the sharpness parameter  $k = 0.07$  and a border size of 100 pixels.

shifts. Due to the smooth Gaussian borders, the formation could be prevented not only because they suppressed the Gibbs-phenomenon, but also because the effects of lower intensity regions on the outskirts of the border region would not be so severe on the errormap if random shifts occurred. That random shifts occurred could clearly be observed as dunes, the indicator for shifts, wandered around the pattern. We tried the same now with the sigmoid broadening and the result was the same. Also in this case stationary stripes were eliminated while dunes persisted both in the pattern  $P_n(x, y)$  and subsequently the image  $I(x, y)$ . Some tests with different parameters for both methods yielded the same result.

### 6.3.2 Corrected pattern manipulation

Based on the results of the target manipulation, we implemented another stage in the optimisation algorithm right after the calculation of the corrected pattern  $P_{n+1}(x, y)$ , in which a Gaussian filter is applied to  $P_{n+1}(x, y)$ , smoothening out the dunes. This technique was already tested during the development of the errormap algorithm at the KIP [37] and yielded positive results. Also in our case, we managed to get rid of the dunes by adding this additional filtering step. The optimised intensity distributions  $I(x, y)$  for both methods can be seen in Figure 45.

With both new border function methods we managed to reduce the RMSE value by about 10% during an optimisation run. In the case of the Gauss-filtered border to 4.22%, in the case of the sigmoid border to 5.13%. This is quite a bit more than what we could achieve with the filtering algorithm (see 6.1), however it for now proved that we could successfully optimise uniform patterns with two different approaches and the optimisation parameters could still be tuned to reach better results. Furthermore from the optimised patterns it seemed obvious that the reason for the comparably worse results likely did not originate from anything to do with the algorithm itself, but rather the optical setup, as we noticed that the pointing of the beam illuminating the DMD had apparently drifted, under-illuminating one corner of the square pattern as can be seen on the in Figure 45 both (a) and (b). The lower corner seems to be slightly under-illuminated both times.

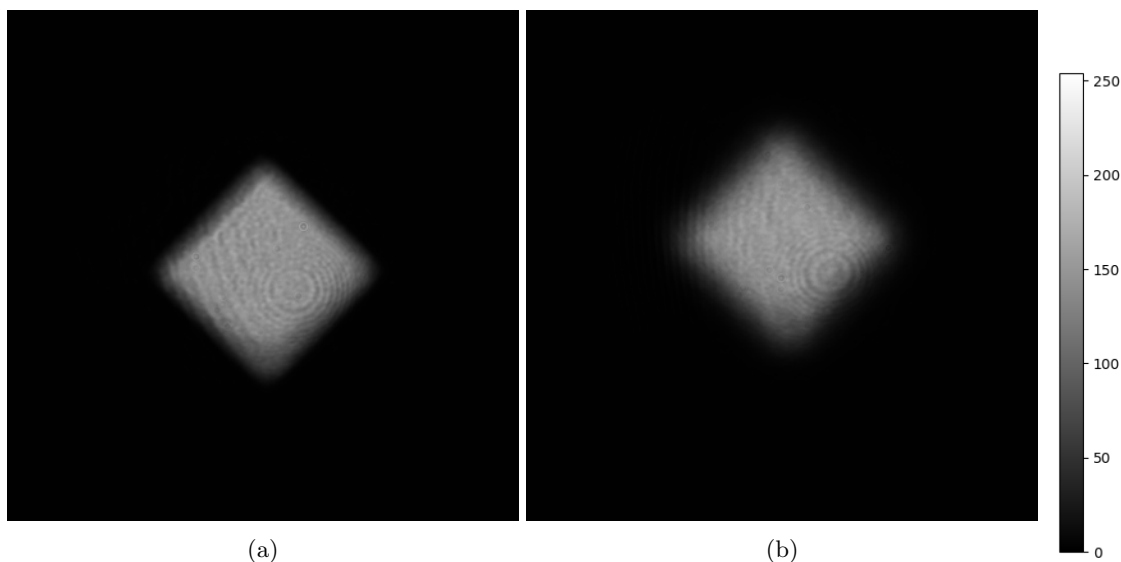


Figure 45: 8-bit camera images  $I(x, y)$  with (a) Gaussian border and (b) Sigmoid border.

Also some aberrations and fringes unrelated to any of the problems described above had appeared likely coming from either dust and perhaps strange aberrations caused by the bandpass filter in front of the camera.

### 6.3.3 Gradient pattern manipulation

In the case of a gradient pattern it is not as easy to define a border function that not only maintains a specific intensity gradient in the radial direction away from the pattern and at the same time also preserves the intensity gradient of the pattern itself. Though the Gaussian filter is very easily applicable to this case, a result can be seen in 46. Here we illustrate how the Gaussian filter managed to improve an optimisation run on a gradient annulus. In 46 (a) and (b) we see the first camera image of the optimisation run  $I(x, y)$  produced by  $P_0(x, y)$ . We can see stationary fringes due to ringing on the camera image (a). (b) depicts an illustrative evaluation method adapted from [37]. Here we probe the greylevel along radial cuts of the annulus, going around the full rotation. One black dot marks the greylevel of a single pixel. Ideally the distribution should closely follow the dotted red line indicating a linear gradient of the greylevel along the rotation. This is clearly not the case in 46 (b). The bottom two images of Figure 46 show the result of the optimisation run with Gaussian smoothing applied to the corrected pattern  $P_{n+1}(x, y)$  at every iteration. We can see how the distribution of black dots now much more closely follows the linear gradient of the red dotted line.

## 6.4 Evaluation

To determine the quality of our optimised patterns, we most of the time relied on the RMSE value or the average and standard deviation in case of the errormap algorithm. However, since both of these methods also have their flaws, as we will elaborate in 6.4, we tried a few other methods as well. In particular, we analysed the optimised patterns by calculating the grey level co-occurrence matrix (GLCM) in 6.4.2 and by probing the density perturbations to be expected when the patterns are projected onto an atom cloud 6.4.3.

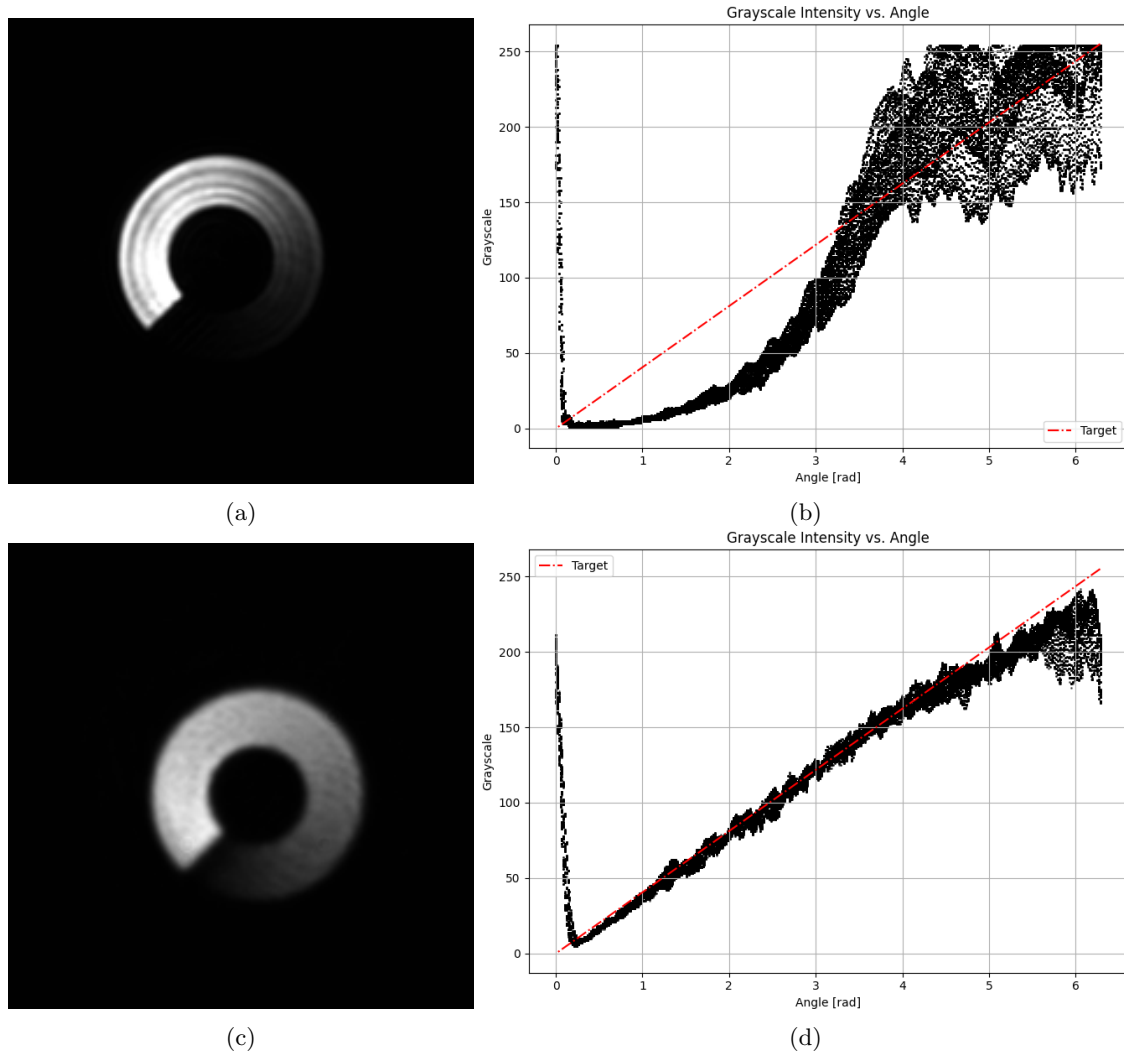


Figure 46: (a) the initial image of a gradient annulus before optimisation, (b) after optimisation. On the right an analysis method as in [37]. The greylevel is tracked along a line extending radially outward from the centre of the image and around the full  $2\pi$  rotation. The red dotted line marks the ideal case in which the intensity increases linearly around the annulus and drops instantaneously after a full rotation.

#### 6.4.1 Root Mean Square Error

For nearly all tests, the root-mean-square-error (RMSE) was the primary indicator to determine the quality or success rate of an optimisation run. To calculate the RMSE of a camera image, it first needed to undergo the proper calibration. Once this step was completed, we could overlay target  $T(x, y)$  and image  $I(x, y)$  and calculate the deviation of the image from the target. This is in principle also a kind of errormap, although the exact calculation differs from that of the errormap in the respective algorithm. To calculate the deviation  $\Delta(x, y)$ , we first normalize both target and image to unity. We indicate this by writing  $\hat{T}(x, y)$  and  $\hat{I}(x, y)$ . Next, we have to make sure the target is rescaled with the mean of the image. This may lead to some relative information on absolute brightness and contrast difference being lost or distorted, but we need to adjust the average greylevel of the target to that of the image to measure the flat top surface variations of the image and not a greylevel offset between image and target. We chose the normalization to the mean over the normalization to the maximum since the maximum pixel value of the image may

fluctuate quite a bit which may provoke problems or unreasonable results when almost the whole array is deemed too dark due to a single outlier. Both image and target are masked, such that the dark background and also the border area is excluded from the calculation of the mean or the deviation. We are primarily interested in uniform box potentials and herein mostly concerned with the homogeneity and flatness of the plateau.

$$\Delta(x, y) = \hat{I}(x, y) - \frac{\mu(\hat{I}(x, y))}{\mu(\hat{T}(x, y))} \hat{T}(x, y) \quad (6.69)$$

Here  $\Delta(x, y)$  is the deviation between the two-dimensional grids of the image  $\hat{I}(x, y)$  and the rescaled target  $\hat{T}(x, y)$ . The means of camera image and target as well as the mean of  $\Delta$  in the next step is always calculated by summing up all pixels of the 2D grid and dividing by the number of pixels. Now we can directly calculate the *RMSE* value.

$$\text{RMSE} = \sqrt{\mu(\Delta^2(x, y))} \quad (6.70)$$

For better readability, the RMSE is ultimately multiplied by 100 to assume a percentage. In this case 0 % would stand for a perfectly flat pattern. Note that in this specific context the RMS error and RMS contrast (RMSC) are yielding the same results. The RMS contrast of an image measures the variation of an image around its own mean and is thus also nothing else than the standard deviation of the image:

$$\text{RMSC} = \sqrt{\mu[I(x, y) - \mu(I(x, y))]^2} \quad (6.71)$$

However since we adjusted the mean of the target to be the same as the one of the image, RMSE and RMSC are identical in this setting. Note that this is only true for uniform targets.

One problem of the way the RMSE is calculated is, that if the determination on the success of a single iteration is based on it alone, the overall intensity level is not taken into account. In the case of the filtering algorithm, this sometimes leads to very flat, but overall also very dark optimisation results. In that case we could in principle just ramp up the power of the illuminating beam, however it is likely that this will at least to some degree higher amplitude variations in a uniform pattern, since as we are ramping up the absolute power, we are also ramping up the contrast between slightly lighter and darker patches. Potentially also non-linear effects in optical elements or the DMD itself, possibly aided by heating may introduce new aberrations. Nonetheless, the calculation of the RMSE remained our method of choice to quickly estimate the quality of an optimised image. A typical result as it pops up after every optimisation run can be seen in 47. We can see multiple panels depicting the target pattern (top left), the first camera image (top centre) and the last camera image (top right) along with two orthogonal cuts through the centre of the optimised image (bottom right and centre) and a 2D grid showing the deviation between the optimised camera image and the target pattern (bottom left). Note the saturated region in the first camera image (top centre). We typically adjusted the power such that the first camera image is slightly oversaturated on purpose. The first camera image of a uniform target is created with a DMD pattern where all mirrors within the target shape are on, thus the next iterations will always be darker.

#### 6.4.2 Grey Level Co-occurrence Matrix

The grey level co-occurrence matrix (GLCM) is a widely used tool in image analysis. We used this tool to get another perspective on what we until now deemed good or bad purely on the basis of its RMSE value. It was developed in the 1970s by Robert Haralick and colleagues [31]. Nowadays



and  $i, j \in [0, p]$  are computed in the following way:

$$C_{\Delta_x, \Delta_y}(i, j) = \sum_{x=1}^n \sum_{y=1}^m \begin{cases} 1, & \text{if } I(x, y) = i \text{ and } I(x + \Delta_x, y + \Delta_y) = j \\ 0, & \text{otherwise} \end{cases} \quad (6.72)$$

Here the translation  $(\Delta_x, \Delta_y)$  from one pixel to the next is determined through the predefined angle and distance.  $x$  and  $y$  are the coordinates of a pixel in the  $n \times m$  sized image and  $I(x, y)$  is the intensity or greylevel of the pixel. A perhaps more intuitive image of how the construction works from [32] is shown in 48

Once the GLCM is computed we can extract a number of different features pertaining to the image from it. A list of overall 14 textural features for image classification which are accessible through the GLCM can be found in [31]. In the following we picked out only one feature which is relevant especially for uniform images, namely the contrast.

We already mentioned in 6.4.1, that for uniform images the RMS contrast (RMSC) is equivalent to the RMSE. The contrast we extract from the GLCM  $C_{GLCM}$  is related to, but different from to the RMSC and the RMSE. As one would expect,  $C_{GLCM}$  quantifies the difference in intensity between pixels, which can be neighbouring but may also be separated by a chosen distance. The distance is given in an integer number of pixels indicating the separation of the two pair pixels. It is calculated the following way:

$$C_{GLCM} = \frac{1}{2} \sum_{i=0}^p \sum_{j=0}^p (i - j)^2 C(i, j) \quad (6.73)$$

The prefactor  $\frac{1}{2}$  only accounts for the fact, that we are summing over all intensity pairings twice. Here  $C(i, j)$  represents the entries of the GLCM, which are nothing more than the number of instances that the pair of intensities  $i$  and  $j$  were detected in the image. It thus acts as a probability distribution, which in turn makes  $C_{GLCM}$  an expectation value for  $(i - j)^2$ , which we will write as  $\mathbb{E}[(i - j)^2]$ . We can expand the expectation value.

$$\mathbb{E}[(i - j)^2] = \mathbb{E}(i^2) - 2\mathbb{E}(ij) + \mathbb{E}(j^2) \quad (6.74)$$

We will now make the assumption that  $i$  and  $j$  are uncorrelated, essentially assuming, that the remaining variations in our optimised pattern resemble Gaussian white noise. In this case  $\mathbb{E}(i^2)$  and  $\mathbb{E}(j^2)$  are equivalent and we can separate  $\mathbb{E}(ij)$ :

$$\mathbb{E}(ij) \approx \mathbb{E}(i)\mathbb{E}(j) = \mathbb{E}(i)^2 = \mathbb{E}(j)^2 \quad (6.75)$$

This allows us to write:

$$C_{GLCM} = \mathbb{E}[(i - j)^2] \approx 2(\mathbb{E}(i^2) - \mathbb{E}(i)^2) = 2\text{Var}(i) = 2\text{Var}(j) \quad (6.76)$$

We can express  $C_{GLCM}$  in terms of the variance. We also know from 6.4.1, that we can write  $\text{RMSC} = \sqrt{\text{Var}(i)}$ . Thus we can relate RMSC to  $C_{GLCM}$ .

$$C_{GLCM} \approx 2(\text{RMSC})^2 \quad (6.77)$$

Note again, that this is only the case, if  $i$  and  $j$  are uncorrelated. Otherwise, the prefactor will be different from two. On the other hand, this may also serve as a measure of how correlated the

noise of our pattern is. Note also, that this relation holds only if  $C_{GLCM}$  is constructed with a distance setting comparable in length to the diameter of the area over which RMSC is calculated and we ideally average over different angles. This on the other hand allows us to rescale  $C_{GLCM}$  for long distances if we already know RMSC and then the rescaled  $C_{GLCM}$  at small distances can serve as an extrapolated RMSC without the need to adjusting the size of or selecting the region on which we calculate it. By selecting only one specific angle, we could also investigate, whether the noise in our patterns more correlated in a certain direction. Last but not least, note once more, that we showed in 6.4.1, that the RMSC and RMSE are equivalent in our case, but only for flat uniform patterns.

In the next step, we applied the GLCM routine and feature extraction to our case. We chose three different optimisation results, two with the errormap algorithm and one from the filtering algorithm and tested them, additionally we tested also a perfectly flat target image for comparison. For the pattern optimised with the filtering algorithm we calculated an RMSE value of 1.89 %. An errormap pattern that was optimised with padded and Gauss-filtered borders reached 4.22 %, the other pattern with sigmoid borders reached 5.13 %. To calculate the GLCM we cut out the uniform flat-top regions of the patterns as we are interested in the level of homogeneity there. For each pattern we calculated the GLCM at  $0^\circ$ ,  $45^\circ$ ,  $90^\circ$  and  $135^\circ$  angle and a fixed distance, thus half-circling around the nearest neighbours of a pixel. We figured that it would not be necessary to complete the full circle as the pairs of pixels in any direction would be identical with those for the case of the opposite direction. For every direction the listed features were calculated and the average out of the four values was taken. This process was repeated for distances from 1 up to 100 or 400 pixels separation respectively. The results are shown below<sup>49</sup>. Here the distance in pixels is

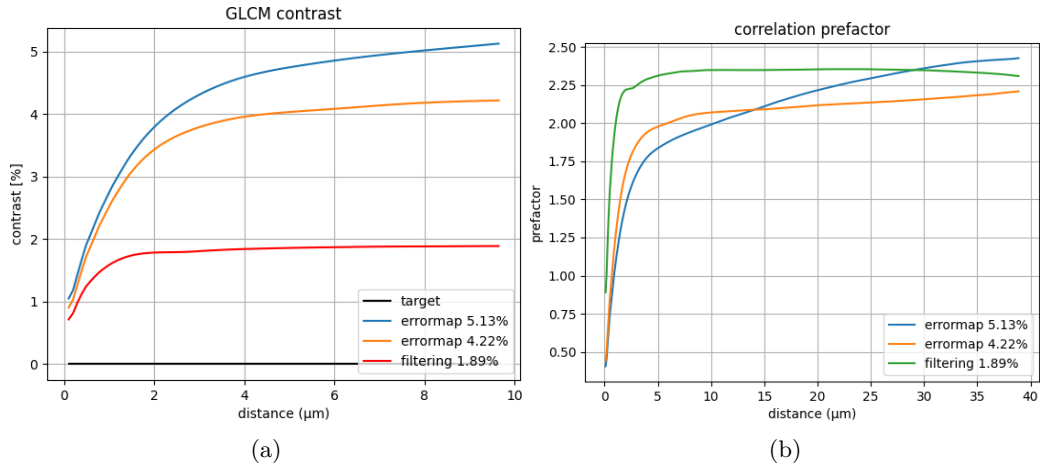


Figure 49: The results of the feature extraction from the GLCM. (a) The contrast, (b) prefactor indicating the correlation of the image

rescaled with the pixel size to represent the distance in  $\mu\text{m}$  in the atom plane. The values for the contrast are also rescaled to extrapolate the RMSC and with that also the RMSE of for arbitrarily sized patches in the pattern.

$$\tilde{C}_{GLCM} = \text{RMSC} \sqrt{\frac{C_{GLCM}}{C_{GLCM}(\text{dist.} = 100 \text{ pixels})}} \quad (6.78)$$

We can observe in 49, that the contrast rather quickly, within few  $\mu\text{m}$  approaches the RMSC or RMSE level we calculated before. This means, that the characteristic size of intensity variations is in the  $\mu\text{m}$  range. While if we look at the contrast of pixels further away from each other,

we not much more increase in contrast, meaning there seems to be little to no overall gradient within the pattern. In the case of the two errormap patterns, the contrast seems to slowly increase further for large distances hinting towards some intensity gradient across the pattern. In 49 (b), we can observe how the correlation prefactor is varying for different distances. It is calculated as  $k = \frac{C_{GLCM}}{RMSC^2}$  and should approach two for large distance in the case of fully uncorrelated patterns. As expected, for all patterns we observe that it is close to two at large distances, but a little larger, hinting towards some degree of correlation in all patterns. We expected this from the errormap patterns, since we know from 49 (b), that there is some smooth intensity gradient in the image, why the prefactor for the filtering algorithm pattern however is even higher most of the time is somewhat puzzling though. It may have to do with edge effects, because the border in this pattern is much sharper than in the two errormap patterns (see 6.3).

The GLCM is certainly a powerful tool in image analysis, allowing access to the above described features and also many more. We can gain more detailed insight in the nature, size and orientation of our intensity variations compared to reducing them to a single number in the case of the RMSE. On the other hand on a very general level, we could also confirm the original classification of patterns into good and bad results that was done on the basis of the RMSE, which is why on a daily basis we will continue to rely on the RMSE as the main indicator to determine the success rate of an optimisation in real time. The GLCM may however be useful in for improving the optimisation algorithms.

### 6.4.3 Density perturbation

To get a more quantitative insight how the grade of flatness achieved in optimisation runs translates onto the grade of homogeneity of density in the atomic gas, we tried to evaluate the kind of density perturbation to be expected if atoms are exposed to a potential of the shape of our optimised patterns. To calculate this we closely follow the calculations in [7] and [6] where a full and detailed report on all the steps can be found.

We assume our atoms are confined in a quasi-2D trap squeezed in  $z$  direction and with dipoles oriented within the  $(x, z)$  plane. We will describe our gas through ground state wavefunction  $\psi(r)$ . The density  $n(r)$  of the gas is simply  $|\psi(r)|^2$ . The wavefunction is a solution for the generalized stationary quasi-2D Gross-Pitaevskii equation:

$$\mu\psi(r) = \left[ \frac{-\hbar^2}{2m}\Delta + V(r) + \int d^3r' U(r-r')|\psi(r')|^2 \right] \psi(r) \quad (6.79)$$

Here  $\mu$  is the chemical potential. The first term with the Laplace operator is the kinetic term, the second one involves the external potential confining the gas, here our optimised patterns will come into play, and the last term describes the interatomic interactions between the atoms, in our case both contact and dipole-dipole interactions. We now perturb the confining potential  $V(r) = V_0(r) + \delta V(r)$  and consider the effect on the wavefunction  $\psi(r) = \psi_0 + \psi^{(1)}(r)$  to first order. We assume that  $\int \delta V(r)dr = 0$  and subsequently  $\int \psi^{(1)}(r)dr = 0$ . The perturbed density will be of the form:

$$n(r) = |\psi(r)|^2 = n_0 + 2\sqrt{n_0}\psi^{(1)}(r) + |\psi^{(1)}(r)|^2 \quad (6.80)$$

With  $n_0 = \psi_0^2$ . We will disregard the term quadratic in  $\psi^{(1)}(r)$  and worry only about the first order density perturbation. Solving the expanded GPE in Fourier space gives us:

$$\tilde{\psi}^{(1)}(k) = \frac{-\sqrt{n_0}\tilde{\delta V}(k)}{\frac{\hbar^2 k^2}{2m} + 2n_0\tilde{U}(k)} \quad (6.81)$$

Therefore for the density perturbation to first order in Fourier space we can write:

$$\tilde{n}^{(1)}(k) = \frac{-2n_0\delta\tilde{V}(k)}{\frac{\hbar^2k^2}{2m} + 2n_0\tilde{U}(k)} \quad (6.82)$$

The interatomic interaction term  $\tilde{U}(k)$  depends on the angle of the dipoles with respect to the  $z$ -axis  $\gamma$ , on the angle of the spatial momenta with respect to the  $y$ -axis  $\phi$  and the ratio between contact and dipolar scattering length  $\epsilon_{dd}$  through:

$$\tilde{U}(k) = \frac{g}{\sqrt{2\pi}l_z} [1 + \epsilon_{dd}([-1 + f(q)\sin^2\phi] + \cos^2\gamma(3 - f(q)[\sin^2\phi + 1]))] \quad (6.83)$$

Here  $g$  is the 2D interaction parameter and  $l_z = \sqrt{\hbar/m\nu_z}/2\pi$  is the harmonic characteristic length scale with  $\nu_z$  the trapping frequency in  $z$  direction. The dependence on  $k$  enters through  $f(q)$  with  $q = kl_z/\sqrt{2}$ :

$$f(q) = 3\sqrt{\pi}qe^{q^2}\text{erfc}(q) \quad (6.84)$$

with  $\text{erfc}$  the complementary error function.

We can treat the intensity variations in our optimised patterns as a perturbation  $\delta V$  of the external potential  $V(r)$ . From our optimised pattern we need to calculate the Fourier transform and also subtract the mean, such that we are only dealing with the perturbation  $\delta\tilde{V}(k)$ . We ensure that the condition  $\int \delta V(r)dr = 0$  is fulfilled. We can insert  $\delta\tilde{V}(k)$  into 6.82 and get a two-dimensional grid of density values. To extract the density variations we calculate the standard deviation of the density perturbation and plot it as fraction of the zero-order density  $\langle\sigma(\tilde{n}^{(1)}(k))\rangle/n_0$ . The tests conducted in [7] and [6] used potential perturbations which were created artificially. Either some defects of fixed momenta and amplitude of the form  $\delta V = \delta V_0 \cos(kr)$  would be introduced into the potential or just some stochastic white noise of variable amplitude. The simulations were realized with quantum gas parameters typical for experiments with ultracold dysprosium. With  $m = 164a.u.$  and  $a_{dd} \approx a_s \approx 130a_0$ , this corresponds to  $\epsilon_{dd} \approx 1$ , though the scattering length of the contact interactions  $a_s$  would be varied throughout the calculations. For our trap geometry we chose a box size of  $L = 20\mu\text{m}$  and a trapping frequency in  $z$  direction between 1 and 16 kHz corresponding to  $l_z \approx 0.25\mu\text{m}$  and  $l_z \approx 0.06\mu\text{m}$  respectively. Assuming roughly  $5 \times 10^4$  trapped in this box, this corresponds to  $n_0 = 125\mu\text{m}^{-2}$ . With  $V_0 = \hbar\nu_z$  we assumed trap depths between  $k_B \times 100\text{ nK}$  and  $k_B \times 1\mu\text{K}$ . When evaluating the potential defects we furthermore set some limits on the wavelengths of the defects or the spatial frequencies in Fourier space in which we are interested. As a lower bound we chose  $k_{min} = 2\pi/L$ , which is a few times the box size and  $k_{max} = 2\pi/\lambda$  so defects of wavelength shorter than the laser wavelength with which the potential is created will be excluded. In absolute numbers this translated to  $[k_{min}, k_{max}] = [0.06, 12.6]\mu\text{m}^{-1}$ .

As shown in Figure 50 in the upper row, we first also evaluated an artificially created white noise potential. If the result matched the results in [6], we could be sure that everything was setup in the right way and could continue. We created a flat potential, added some random noise with a fixed amplitude corresponding to 1% RMSE when the flatness of the pattern was analyzed, and transformed to Fourier space. Here we imposed the limits to the pattern and cut out all defects of higher or lower frequency and then employed 6.82 to calculate the density perturbation and also calculated  $\langle\sigma(\tilde{n}^{(1)}(k))\rangle/n_0$  which in the case of no perturbation, i.e. a perfectly flat pattern would be zero. This was repeated for different orientations of the dipoles ( $\alpha \in [0, \pi/2]$ ) and different scattering lengths ( $\epsilon_{dd} = [0.5, 0.9]$ ). Note that with the white noise pattern we also include all possible directions of  $\phi$  as defects. The results are shown below. They match the results of the paper [6] exactly. At this point we moved on to evaluate some of the optimised patterns. We

chose the same patterns already evaluated in the previous section on the GLCM. Once again we focused on the flat section of the optimised patterns only and disregarded the exact shape of the border region. For now we were only interested in what perturbations are to be expected from imperfections of the uniform part alone. Thus as in the previous section, a  $400 \times 400$  pixel wide square was cut out from all optimised patterns and the same routine as with the white noise pattern was repeated. All results are shown in Figure 50 for the case of  $\nu_z = 1$  kHz.

In the left and the central column we can see the potential perturbation in real and in Fourier

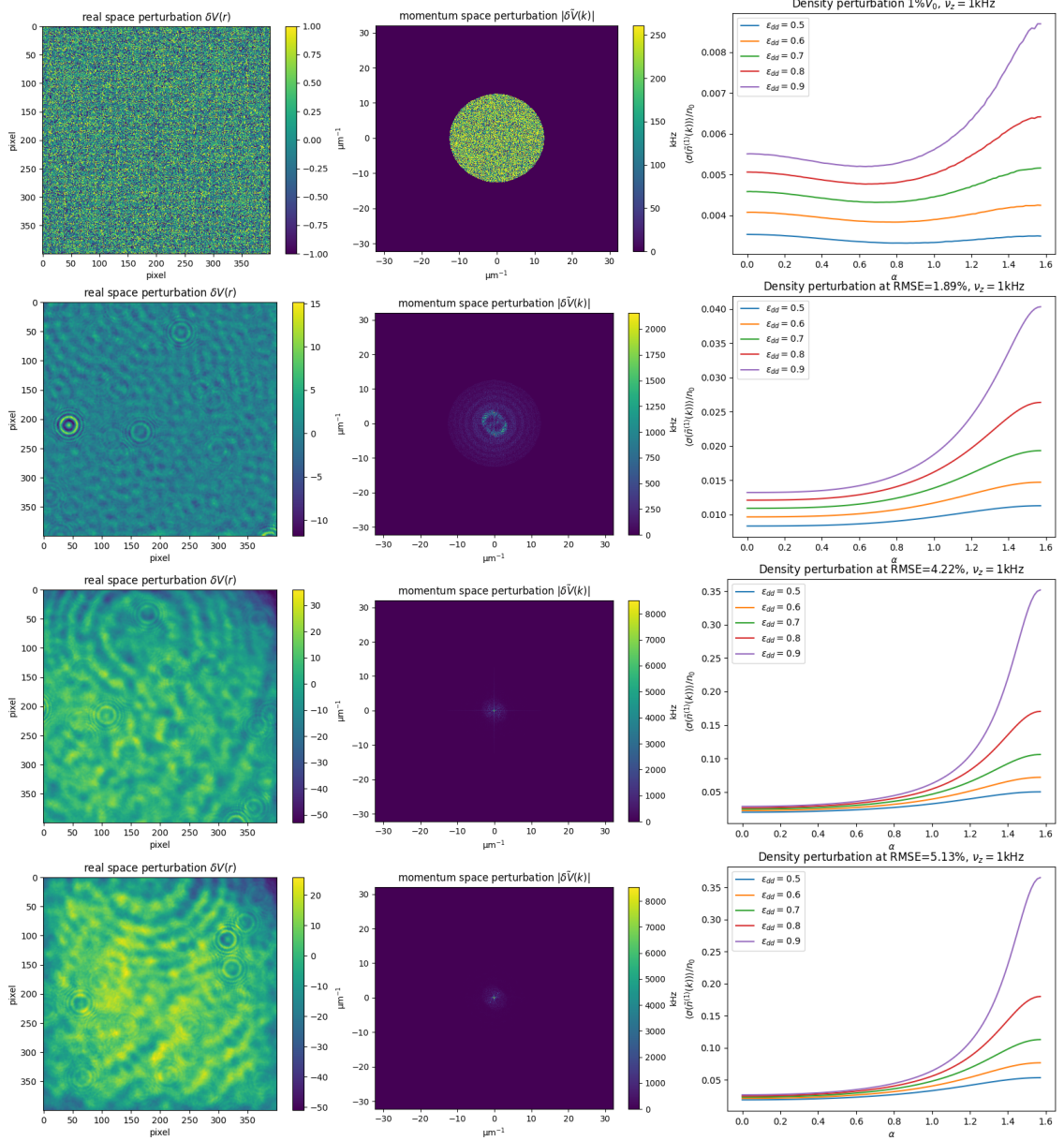


Figure 50: In the left column the real space perturbations, in the middle the pattern transformed in momentum space with the upper and lower limit for momenta applied. On the right the behaviour of  $\langle \sigma(\tilde{n}^{(1)}(k)) \rangle / n_0$  for  $\alpha \in [0, \pi/2]$  and  $\epsilon_{dd} = 0.5, 0.6, 0.7, 0.8$  and  $0.9$ . In the case of white noise, for each point 20 patterns were created and the density perturbation averaged.

space respectively. In Fourier space the frequency filter accounting for the box size is already applied. In 51 we furthermore see a cut through the centre of the potential perturbation in Fourier space, this time without any filters. The perturbation for all patterns is laid on top of each other

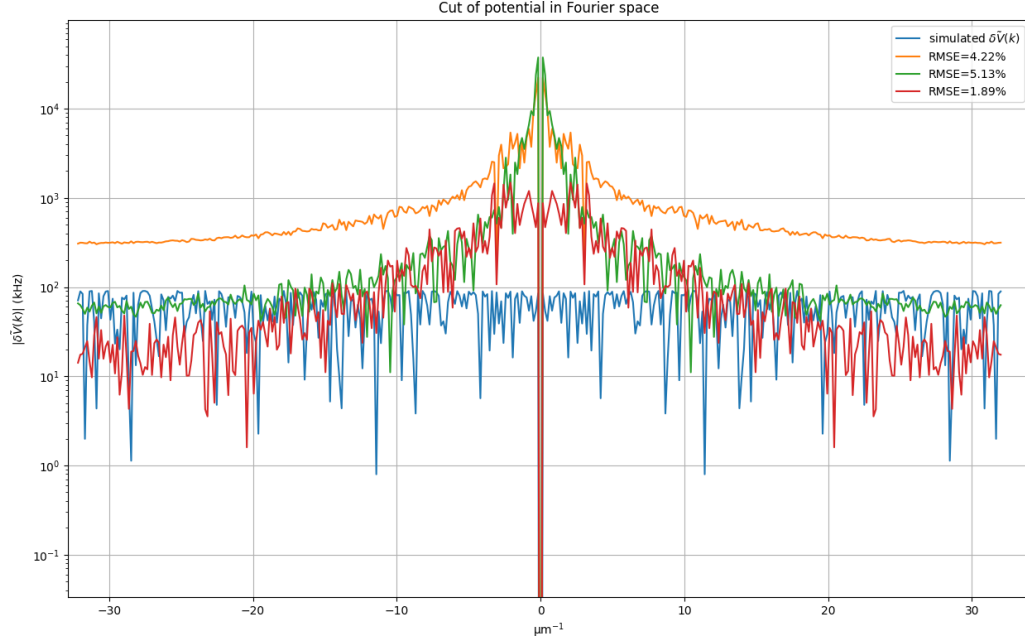


Figure 51: Cut through the centre of the momentum space perturbation for all patterns overlaid on top of each other (unfiltered). Logarithmic scale for better readability, otherwise increase around the centre would dominate.

and plotted on a logarithmic scale. We can observe that compared to the optimised patterns, the perturbations from the simulated pattern maintain a relatively constant level for all frequencies while at least in the pattern which was optimised with the filtering algorithm, high frequency perturbations are suppressed below those of the white noise pattern. Note that the central peak in all spectra is missing since they only represent the variation  $\delta\tilde{V}(k)$  and were thus normalized with their respective mean. What is perhaps most puzzling is the clear discrepancy between the two errormap patterns, especially the significant difference at high frequencies and the fact that the pattern with the lower RMSE actually exhibits larger variations in Fourier space seems counter-intuitive. We can not observe this discrepancy in  $\langle\sigma(\tilde{n}^{(1)}(k))\rangle/n_0$  in 50. One possible explanation may be, that the pattern with a higher RMSE has a small smooth gradient or a curvature across its grid and less high frequency variations from its mean, while the pattern with lower RMSE is flatter overall but has more variations across its flat surface. We saw evidence of some sort of gradient also when we analysed the patterns with the GLCM (see 6.4.2). The only difference regarding the parameters of the optimisation run in which the two errormap patterns were created is the border function. As mentioned in 6.3, the sigmoid border function which was applied to the pattern with higher RMSE also modulates a small region within the original flat target. This may be a source of the curvature we now seem to observe.

We observe in 50 that the  $\langle\sigma(\tilde{n}^{(1)}(k))\rangle/n_0$  that is to be expected even from the pattern that was optimised down to 1.89% RMSE is substantially higher than the one of the white noise pattern scaled such that  $\delta V$  was equivalent to 1%  $V_0$ . When we go to even higher RMSE the increase in density perturbations is also drastic, although the two patterns from the errormap algorithm seem to provoke relatively similar perturbation even though there is still almost one percent RMSE difference between them. What is also noteworthy is that while in the white noise image the spatial components are evenly distributed, they are much more concentrated around the centre. The low spatial frequency components strongly dominate the Fourier pattern. For the case of the white noise pattern this is expected, since it is not smoothed in any way, high amplitude positive and

negative deviations may lie right next to each other in real space, corresponding to an extreme jump in intensity, in turn corresponding high frequency Fourier components. For the filtering algorithm, we would expect that high frequencies are filtered out (see 6.1). Although we have also observed before, that if during the filtering optimisation, the correction is unsuccessful too many times, the cut-off frequency of the low-pass filter will increase more and more, eventually allowing higher and higher frequencies to enter. This is not necessarily a bad thing as high frequency components are also necessary to compensate high frequency aberrations, but at some point it may become a problem. That the error map pattern seem almost depleted of high frequency components may be a result of the Gaussian filter, that is applied during the optimisation process, see chapter 6.3

All in all our evaluation of the density perturbation seems to suggest that for dipoles oriented along the  $z$  direction an RMSE of little less than 5% is sufficient to only expect perturbations on the order of a few percent of  $n_0$ . If dipoles are tilted into the  $xy$ -plane though this number might quickly up to a third for large  $\epsilon_{dd}$ . If we increase the trapping frequency  $\nu_z$  further up to 16 kHz,  $\langle \sigma(\tilde{n}^{(1)}(k)) \rangle$  even approaches the same order of magnitude as  $n_0$  if the flatness of the images corresponds to an RMSE of around 2% or more.

## 7 Integration into DyLab setup

As described in 5, the DMD imaging setup was first built on a separate breadboard, which was then transported as a whole to the main experiment and incorporated into it. Before moving we had to make sure that everything was bolted down tightly and all translation stages were locked. It was screwed down on the highest (the 3rd) breadboard level of our experiment. The position of the outgoing (reflection) beam after the first lens of the second 4f setup is adjusted such, that it is aligned with an existing imaging setup. There the green DMD beam is overlapped with a blue imaging beam through a dichroic mirror and they are guided towards a hole in the breadboard layer, which sits straight above the microscope objective and the centre of the main chamber. As the control board of the DMD stands slightly elevated on two posts and is encased in an aluminium box, it is the highest part of the setup and would only just fit below the light panels on the hood of the optical table. As the breadboard sits roughly on eye level, it is not only physically challenging to work on the setup, but the laser beams coming off of the various PBS cubes and the DMD grid itself may pose a safety hazard. Though most of the light leaking from the DMD through higher diffraction orders and the 'OFF' components is blocked with a protective box, this box also has two holes for in- and outgoing beams through which some light can escape. Some preliminary beam blocks for PBS leak light were also installed on the edge of the breadboard.

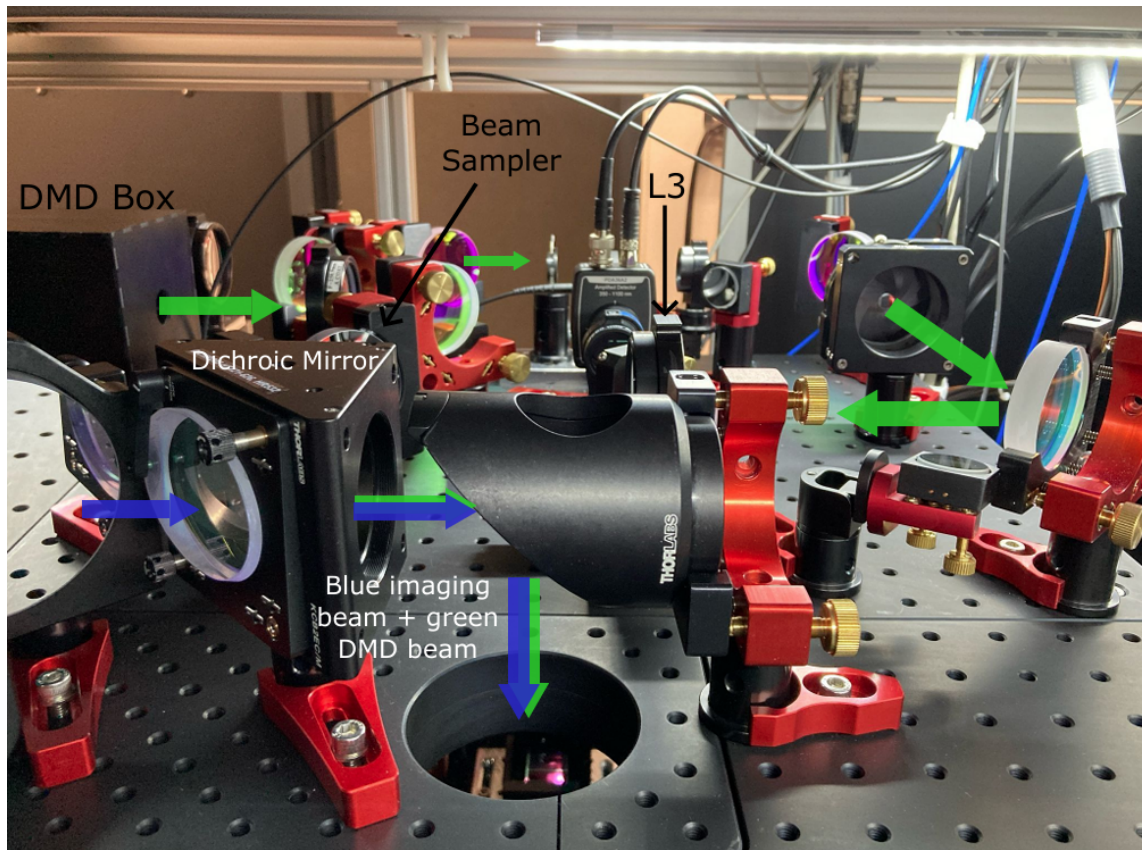
### 7.1 Laser setup

The laser light for the DMD is delivered by a *GLR-532-20-SF* laser from IPG. It can produce up to 20 W CW light at 532 nm. Usually though we have it running at 18 W output power. This laser is distributing light to our accordion lattice and the DMD. The laser head is mounted on a separate breadboard on which the outgoing beam is split for the different distributions. The output power distributed to the DMD arm can be controllably attenuated through an acousto-optic modulator (AOM). We can tune the diffraction efficiency of the AOM by varying its RF power. After the AOM, light is coupled into a fibre and supplied to the DMD imaging setup. By calibrating the RF power for the AOM against the output power after the fibre, we can precisely tune the amount of power we couple into our DMD setup, as the RF power can be controlled through our labscript suite used for controlling the experiment. To ensure the input power of light remains constant even if there are small variations for example in the coupling efficiency, the power level in the imaging setup is constantly monitored with a photodiode measuring the intensity of the leak light of the last mirror before the DMD. A PID module (*SIM960* from *Scientific Instruments*) is connected to this photodiode and to the AOM driver with PID parameters optimised to help quickly and smoothly compensating for variations which may occur and also maintain a fast switching time when light into the DMD setup is ramped up or down. We can usually provide a stable level of laser power of up to 1.2 W to the DMD.

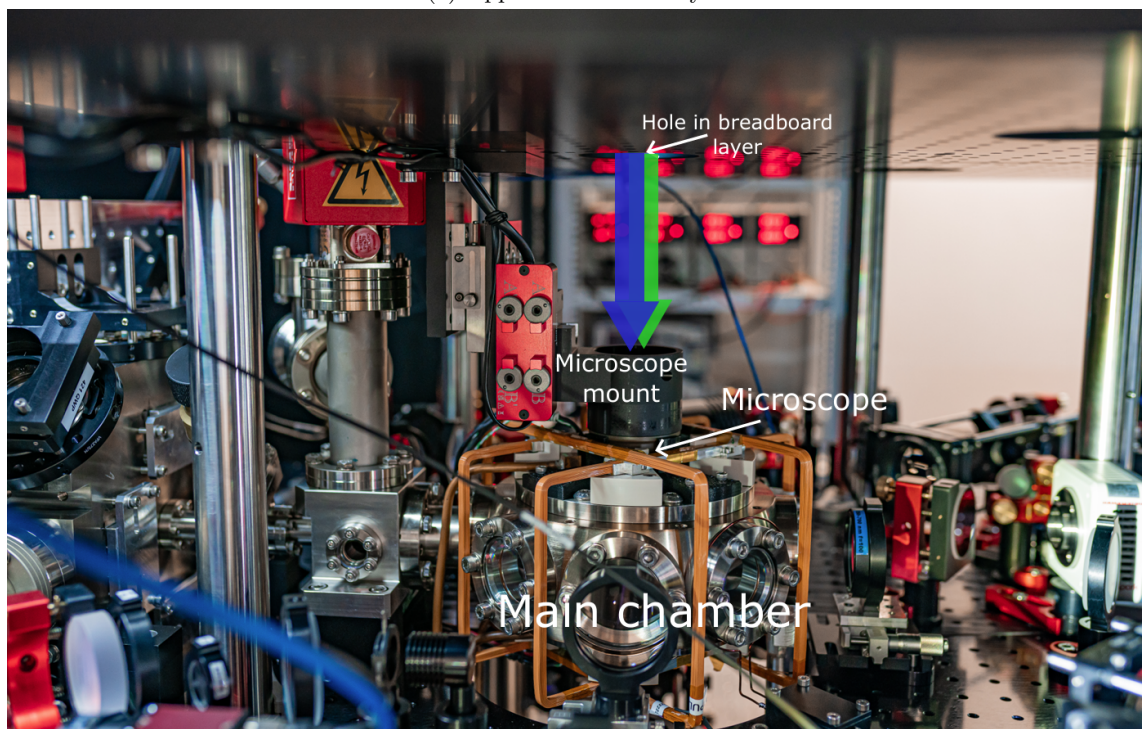
### 7.2 Alignment

Once we had physically implemented the DMD imaging setup into the main experiment and stabilized the laser power supply, we could start to align the DMD output beam with our microscope and our atom cloud.

In a first step, we displayed the lattice pattern shown in Figure 24 on the DMD. In the Fourier plane just before the microscope we could observe a central spot and four outlying spots along the  $\pm x$  and  $\pm y$  direction. With the help of a 3D printed mask matching the diameter of our microscope and with a 2 mm diameter hole in the centre, we tried to carefully align the pattern



(a) Upper breadboard layer



(b) Lower breadboard layer

Figure 52: (a) Picture of DMD setup on the upper breadboard layer. Beam is redirected through hole in the breadboard to (b) lower breadboard layer and into microscope and main chamber. (b) Courtesy of Maurice Rieger

such that the central maximum went through the centre of the mask and the outlying light spots lined up with the edge of it. We did this at two positions along the vertical axis above the main chamber, namely at the hole in the upper breadboard layer and at the microscope mount (see Figure 52) to make sure the DMD beam goes straight through the centre of our microscope.

With this rough alignment in place we moved on to fine tune the alignment with the atoms. For this we changed the DMD pattern to only a narrow Gaussian spot of approximately 25 pixels width. This produced a very wide beam with a diameter of almost 5 mm and with nearly Gaussian shape (see Figure 16) in the Fourier plane before the microscope. In the atom plane (i.e. the imaging plane of our setup) it resulted again in a very narrowly focused spot, due to the demagnification now only with a diameter of roughly  $5\ \mu\text{m}$  and subsequently a Rayleigh range of about  $37\ \mu\text{m}$ . If the beam was close enough to our atom cloud, atoms should accumulate in the waist of the tweezer like beam and thus indicate which way we had to move the microscope such that the waist overlaps even better with the position of our atomic cloud.

At our first try, it turned out that we had to lower the microscope by about  $96\ \mu\text{m}$ . However we could only lower it by  $15\ \mu\text{m}$  before hitting the edge of the translation stage. Subsequently we raised the position of the atom cloud. After this was done though, the cloud could no longer be imaged through the vertical imaging setup, whose imaging beam also goes through the microscope. This was likely due the cloud previously not forming at the centre of the chamber. To compensate

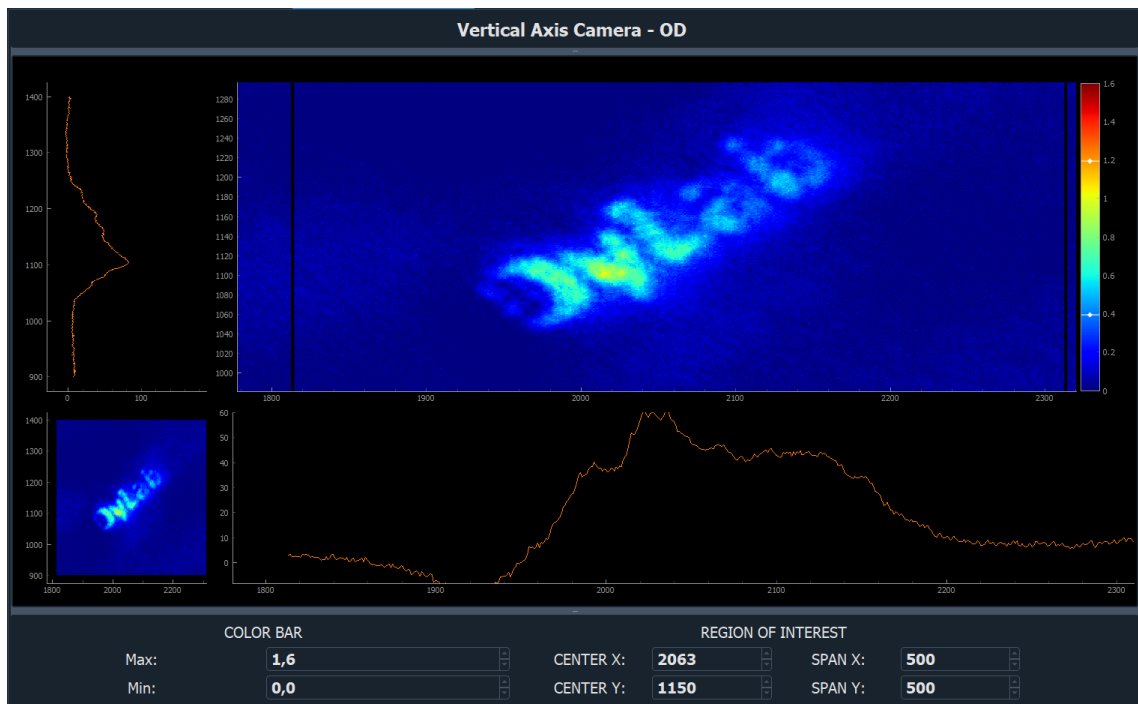


Figure 53: Signal of our DMD beam on the atoms

that, a small tilt in the microscope was previously introduced to line the imaging beam up with the cloud. This was now problematic as the cloud formed at a different vertical position.

To correct the misalignment, we translated the microscope objective again towards the horizontal position of the atom cloud. We carefully tried to centre the imaging beam on the objective also visually ensuring that there is no tilt of the objective and that the imaging and DMD beams are going in a straight vertical line through the centre of the main chamber. Eventually the atom cloud was once more visible through the vertical imaging setup. We then moved the position of the cloud in the horizontal plane to where we suspected our DMD beam would be. This whole process of

translating the objective, centring the imaging beam and DMD beam with our alignment tools and translating the atom cloud was iterated until we converged on an arrangement where the beams overlapped with the atom cloud and no tilt of the objective was apparent.

In this configuration we managed to produce the first clear signal of a rather complicated DMD pattern on the atoms. As can be seen in Figure 53 we displayed the name of our laboratory on the DMD and we were able to write it with atoms. We can also see, that the quality of the signal can still be improved, also the DMD grid seems to be not exactly evenly illuminated. However we can continue now to optimise these things while directly monitoring the effects of our efforts on the atoms.

### 7.3 Pattern Generation and Optimisation Tool

When the DMD is used during an experimental sequence, i.e. a pattern is loaded to it, displayed and the laser beam is turned on, illuminating the DMD grid and being sculpted into the desired shape to be imprinted on the atoms, all this is controlled through our labscrip-suite. The DMD is registered as a labscrip device and patterns saved on our control computer can be loaded to the DMD and displayed through the grid upon trigger. Also multiple patterns can be loaded to the chip and displayed in a fast switching sequence. With the restriction that there is a maximum number of patterns that can be loaded to the DMD chip at once. All of this including for how long and at what intensity the DMD should be illuminated can be defined in a labscrip sequence which when engaged will send out all necessary signals to the various control units of the experimental setup.

In addition, we have created an external dedicated tool to deal with the generation of 8-bit and 1-bit DMD patterns, with the calibration of the pointing of the transmission arm and the light-based optimisation of DMD patterns. We named it the Pattern Generation and Optimisation Tool (PGOT). This is not part of the labscrip-suite. We control the DMD using the same Python API that was used in the tests outside the main experiment. However all laser distribution systems are controlled through labscrip. The illumination of the DMD during an optimisation run is set manually. As of now there is no block or any aperture to prevent light from entering the microscope apparatus during an optimisation run. It is thus not possible to run an experimental sequence while the optimisation is running. Even though the software is decoupled, there will always be some light randomly blinking into the main chamber.

As mentioned above, the PGOT has three main features, which are all accessible through a graphical user interface (GUI). Each feature and the structure of the GUI will be explained in the following sections.

#### 7.3.1 Generation

The generation of a wide variety of patterns is greatly simplified through the PGOT. One can just select what general shape one wants to create. For now the familiar shapes from the tests above like the square, a circle, a gradient annulus, a Gaussian pattern or also a Siemens star with an arbitrary number of cycles can be created. But also some others, such as a ring, an ellipse with variable proportions and also orientations, a lattice or a chequerboard are available.

For each shape one or more parameters have to be defined determining the exact size and proportions. A screenshot of this part in the GUI is shown in Figure 54. In the GUI if a shape is selected, the necessary definitions can be highlighted through the 'show attributes' button. By default the desired pattern will be created within a bounding box of  $1600 \times 1600$  pixels in the centre of the DMD grid, but this can also be changed. For the case of a circle we have for now additionally

added the feature that one can impose a potential on the shape. This can be just a linear gradient from one side to the other or a harmonic, cubic or quartic potential. It is also possible to enter an arbitrary potential depending on the radius  $r$  of the circle and thus forming a circularly symmetric potential which is then imposed on the circle. To implement the stirring technique mentioned way back in 3.3, we need to have a series of slightly varying images similar to a stop-motion movie. This is also possible to generate in the PGOT.

We can define a sequence by fixing the kind of variation we want, either scale, rotation or translation, then we need to define a start and stop value, this can be a characteristic size parameter, like the radius for a circle or the side length for a square, an angle value or a pixel value and finally we need to state how many steps we want. The sequence according to our needs can then be created by one click. One pattern which is also included in the list of possible shapes is a comb consisting of some number of dots with variable size spread out along a line. This shape is specifically meant to be used as a sequence in which the comb is translated across the DMD grid, and thus stirring through the atomic cloud.

As long as we do not check either the 1-bit or 8-bit box in the GUI, the image we are trying to create will not be saved, it will only be displayed in the GUI. This gives us the opportunity to play around with all the parameters until we are satisfied with the result. Only once we click one of the boxes, or both of them, the image will be saved in the selected format. The folder where it is saved is by default a folder called 'DMD\_images' on our control computer (as can be seen in 54), but this of course can also be changed.

The image shows a settings panel for a shape generator. At the top, 'Shape' is set to 'Ellipse'. Below this are two buttons: 'Settings' (highlighted) and 'Show attributes'. A list of parameters follows: 'Radius' (highlighted), 'Length', 'Outer Radius', 'Inner Radius', 'Minor Axis' (highlighted), 'Major Axis' (highlighted), 'Square Size', 'Sigma', 'Cycles', 'Lattice X', 'Lattice Y', and 'Rotation'. Below these is 'Impose potential' set to 'None', and two unchecked checkboxes for '8-bit' and '1-bit'. At the bottom, 'Save Directory' is set to 'DMD\_images', and there are two buttons: 'GENERATE SINGLE' and 'GENERATE SEQUENCE'.

Figure 54: Generator settings with the necessary parameters for an ellipse highlighted

### 7.3.2 Calibration

The calibration routine is an integral part of both optimisation algorithms. Without a proper calibration, we quickly encounter problems both for the filtering and the errormap algorithm. Though it was mentioned many times before, it was never properly explained as other aspects stood more in the focus. This will be done now in this subsection.

In the PGOT GUI, there is only a simple ON/OFF switch for the calibration. If it is engaged, the calibration routine will be added to the beginning of the optimisation sequence.

At the beginning of the calibration sequence itself, the calibration pattern is created. It consists of a rectangular box with three seemingly arbitrarily placed dots inside it as can be seen in Figure 55. This image is then displayed on the DMD and the intensity pattern which forms is recorded with the camera that is used the optimisation sequence (see Figure 55). The positions of the dots in both the calibration pattern, from now on called the target coordinates, and the recorded image, now

called the source coordinates, are then calculated. An initial guess for the affine transformation matrix is applied to the source coordinates. For our case of 2D images, the affine transformation matrix is a  $3 \times 3$  matrix of the following form:

$$A = \begin{bmatrix} a & b & t_x \\ c & d & t_y \\ 0 & 0 & 1 \end{bmatrix} \quad (7.85)$$

Here  $a$  and  $d$  determine the rescaling of the source image in  $x$  and  $y$  direction respectively, while  $a$ ,  $b$ ,  $c$  and  $d$  together are the constituents of a regular 2D rotation matrix and determine the rotation of the pattern by an angle  $\xi$  around the centre. In principle a shear to the pattern can also be computed and introduced by the off-diagonal elements  $b$  and  $c$ , though for our case this is usually not necessary. The translation of the image is determined by  $t_x$  and  $t_y$ . The third row of the matrix only maintains the in-plane  $z$  coordinate for the 2D case. In the beginning an initial guess for the necessary rotation, scale and translation of the image has to be given. When the source coordinates are transformed with this initial guess matrix, it should be possible to correctly attribute the dots of the target and source image to each other by sorting the source coordinates to the closest target coordinates. From the remaining distances between source and target coordinates, the correct affine transformation matrix is calculated. If the initial guess is

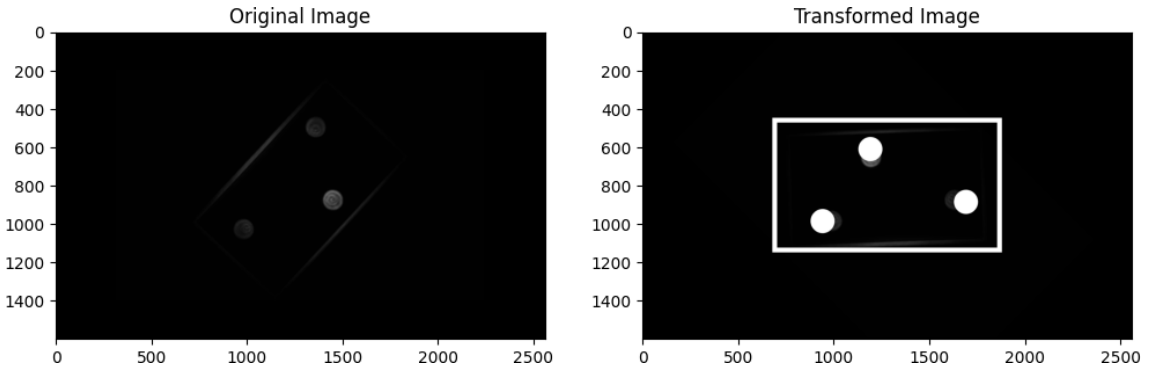


Figure 55: Left: source image, right: target image overlapped with source image transformed with initial guess.

not good, it could be that source and target coordinates from different dots are matched together and the resulting transformation matrix is wrong. A good indicator for us to determine whether this is the case is the rotation angle which can be extracted from the transformation matrix. It should always be near  $\xi = 135$ , which can be understood by tracing the rays of our laser beam all the way through the DMD setup. When the correct transformation matrix is computed, all its parameters are saved into a pickle file. This file is always saved or copied into the folder for the current optimisation run. The affine transformation matrix can easily be constructed by accessing the file and extracting the parameters whenever a mapping of the camera image onto the target image is necessary during the run.

Usually it is not necessary to perform the calibration routine for every optimisation, only if it has been some time since the latest calibration or if something on the setup was changed of course one should renew the calibration to ensure a good optimisation result.

### 7.3.3 Optimisation

As a final feature, we can start an optimisation run directly from the GUI. For this there is a designated optimisation panel below the generation panel in the GUI (see Figure 56).

We can first select what algorithm we want to use, the errormap algorithm or the filtering algorithm. In the selection menu there is also the possibility for 'Display only'. When this option is selected the DMD will just continuously display a pattern of our choice. Once we have selected the algorithm we can define the relevant optimisation parameters which are specific for the selected algorithm. In the case of the filtering algorithm these include things like the initial cut-off frequency, a safety factor by which the RMSE has to be improved to be considered lower than in the previous iteration and a variety of border parameters.

For the case of the errormap algorithm it includes the  $I_{max}$  setting and the error scaling factor  $\alpha$ . All parameters pertaining to the new border function we discussed in the previous chapter can also be changed, however unlike the border function from the filtering algorithm they are technically not part of the optimisation routine itself, instead they simply modify the target image. Some general, not algorithm-specific parameters can also be set in the optimisation settings, such as the exposure time of the camera or the analysis region. Ultimately we can define how many iterations we want. For all these parameters there are default values to which the program will fall back if nothing new is defined. The defaults have been determined during many trials over course of all modifications mentioned in chapter 6. Finally as mentioned in the previous subsection, we can switch on or off the calibration routine. Once we engage the RUN button, the optimisation sequence as described in 4 will begin. There is also a 'STOP' button which will immediately interrupt an optimisation run.

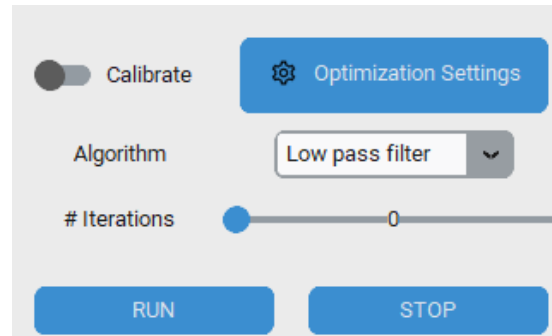


Figure 56: Optimiser settings

## 8 Outlook

Over the course of this thesis, we reported on the planning, development and implementation of an optical setup allowing us to imprint tailored attractive potentials onto a quasi-2D dipolar quantum gas. We achieved this through a setup in which we image a DMD grid on which we can display any binary pattern (4.3 and 5). This pattern acts as an aperture modulating the intensity distribution of our laser beam. We demagnify the initial modulated intensity distribution through two 4f setups with which we achieve a demagnification factor of 78. The resolution of our imaging setup was measured to be 841 nm (5.1.2). We have shown that this limited resolution allows us to greyscale an image (4.3.2) and thus produce not only binary potentials but also include smooth gradients in a potential.

Since we are initially most interested in creating flat top potentials to produce homogeneous quantum gases, we developed and implemented a light-based algorithm aimed at compensating the inhomogeneity of the incoming beam by iteratively modifying the DMD pattern. This optimisation was conducted in a separate part of our optical setup which included an imaging setup with a smaller demagnification. Ultimately we managed to produce a beam with a uniform intensity distribution both with a global optimisation approach (6.1) as well as through a local pixel based approach (6.2). In the two approaches reached an RMSE of around 2% and around 4% respectively across the flat top.

We implemented our optical setup into the main experiment and aligned it such that the amplitude modulated laser beam is focused onto the atom cloud (5.2.1). In order to simplify the generation of DMD patterns and the control of the optimisation we also implemented a program which allows us to do just that externally, removed from the main experimental sequence (7.3).

As this thesis project came to a close, we managed to get a relatively clear signal of an arbitrary DMD pattern on the atoms (see Figure 53). One logical next step could be to implement a density based optimisation routine. Instead of optimising the DMD pattern based on images of the intensity distribution of our beam, we would do exactly the same only with images of the density distribution of the atomic cloud. Also when it comes to the optimisation routine itself, there is probably still room for improvement. The search for the optimal parameters to conduct the optimisation can and should certainly be more systematized to produce better results, especially for the case of patterns with a smooth gradient. Overall it seemed like the errormap algorithm is able to deal with gradient patterns better, while the filtering algorithm is better with uniform patterns. A next step could therefore also be to combine the two and have them act on different parts of a pattern. For example if we want to design a potential which is flat but falls off at the edge according to a specific function one could have the errormap algorithm act on the edge while the filtering algorithm acts on the flat part.

With flat uniform patterns either produced with light-based or density based optimisation, we can probe properties of our dipolar gas in modulated or unmodulated density phases in different arbitrary geometries.

Another possible future project to expand the applicability of the DMD imaging setup is to implement a repulsive trap. We already discussed the possibility of repulsive trapping which would otherwise work completely analogously to the described attractive trap setup. We found possible wavelengths to operate a repulsive trap at near the 684 nm but more suitably near the 530 nm transition of dysprosium (3.4). As mentioned the advantage of a repulsive trap for uniform patterns is, that since atoms are seeking the low intensity regions of the trap the optimisation can potentially be simplified. In principle our optical setup should work equally well no matter whether we are imaging repulsive or attractive potentials, especially since the suitable wavelength we determined

in 3.4 for repulsive trapping is close to the wavelength the setup was originally designed for. Aside from implementing box traps with the DMD we also only briefly touched on the possibility of exciting dynamics in the atom cloud by moving a potential barrier or through it (3.3). This can be achieved by rapidly displaying a sequence of DMD patterns where the barrier moves slightly from one pattern to the next. The fast switching time of the DMD (see Tab. 3) allows us to display the patterns in quick succession. This technique can in general be used to disturb the system, introduce disorder and drive it away from equilibrium. One exemplary application is the excitation of vortices in the atomic cloud which can be interesting in particular in dipolar systems as the interplay between conventional interactions and the dipolar interactions can lead to exotic new vortex phases and behaviour. For the implementation of the stirring technique as touched on in 3.3 and described in [52] and [37] a repulsive trap is advantageous as we need a depletion of density where we stir. This can in the case of repulsive trapping be achieved by a light cone moving through the cloud. For attractive trapping one would need a hole within a trapping potential. All in all with the DMD setup we managed to implement is an important and versatile component into our experiment which opens up new possibilities to alter the geometry as well as the phase and density distribution of our atomic gas and also to induce dynamics within it paving the way for a variety of future research projects.

## References

- [1] M. H. Anderson, J. R. Ensher, M. R. Matthews, C. E. Wieman, and E. A. Cornell. Observation of Bose-Einstein Condensation in a Dilute Atomic Vapor. *Science*, 269(5221), 1995.
- [2] B. Bayer. An optimum method for two-level rendition of continuous-tone pictures. *IEEE International Conference on Communications*, 1(1-15), 1973.
- [3] J.H. Becher, S. Baier, K. Aikawa, M. Lepers, J.-F. Wyart, O. Dulieu, and F. Ferlaino. Anisotropic polarizability of erbium atoms. *Physical Review A*, 97(012509), 2018.
- [4] R. N. Bisset, D. Baillie, and P. B. Blakie. Roton excitations in a trapped dipolar Bose-Einstein condensate. *Physical Review A*, 88(043606), 2013.
- [5] D. Bloch, B. Hofer, S.R. Cohen, M. Lepers, A. Browaeys, and I. Ferrier-Barbut. Anisotropic polarizability of Dy at 532nm on the intercombination transition. *Physical Review A*, 110(033103), 2024.
- [6] T. Bourgeois and L. Chomaz. Effect of trap imperfections on the density of a quasi-two-dimensional uniform dipolar quantum Bose gas. *Physical Review A*, 110(043303), 2024.
- [7] Thibault Bourgeois. Tailorable optical trap with Digital Micromirror Device for Dysprosium experiment. Master's thesis, Universität Heidelberg, 2023.
- [8] Maxime Bôcher. Introduction to the theory of Fourier's series. *Annals of Mathematics*, 7(3), 1906.
- [9] F. Böttcher, J.-N. Schmidt, M. Wenzel, J. Hertkorn, M. Guo, T. Langen, and T. Pfau. Transient Supersolid Properties in an Array of Dipolar Quantum Droplets. *Physical Review X*, 9(011051), 2019.
- [10] L. Chomaz, L. Corman, T. Bienaimé, R. Desbuquois, C. Weitenberg, S. Nascimbène, J. Beugnon, and J. Dalibard. Emergence of coherence via transverse condensation in a uniform quasi-two-dimensional Bose gas. *Nature Communications*, 6(6162), 2015.
- [11] L. Chomaz, I. Ferrier-Barbut, F. Ferlaino, B. Laburthe-Tolra, B. L. Lev, and T. Pfau. Dipolar physics: a review of experiments with magnetic quantum gases. *Rep. Prog. Phys*, 86(026401), 2023.
- [12] L. Chomaz, D. Petter, P. Ilzhöfer, G. Natale, A. Trautmann, C. Politi, G. Durastante, R. M. W. van Bijnen, A. Patscheider, M. Sohmen, M. J. Mark, and F. Ferlaino. Long-lived and Transient Supersolid Behaviors in Dipolar Quantum Gases. *Physical Review X*, 9(021012), 2019.
- [13] S.L. Cornish, M.R. Tarbutt, and K.R.A. Hazzard. Quantum computation and quantum simulation with ultracold molecules. *Nature Physics*, 20(730-740), 2024.
- [14] J. Denschlag, J.E. Simsarian, D.L. Feder, C.W. Clark, L.A. Collins, J. Cubizolles, L. Deng, E.W. Hagley, K. Helmerson, W.P. Reinhardt, S.L. Rolston, B.I. Schneider, and W.D. Phillips. Generating Solitons by Phase Engineering of a Bose-Einstein Condensate. *Science*, 287(5450), 2000.
- [15] L. Dobrek, M. Gajda, M. Lewenstein, K. Sengstock, G. Birkl, and W. Ertmer. optical generation of vortices in trapped Bose-Einstein condensates. *Physical Review A*, 60(5), 1999.

- [16] B. Douet, T. Tedoldi, A. Kabacinski, A. Morana, G. Gallot, and R. Bouganne. Digital micromirror device for holographic and Fourier optics applications. *Emergent Scientist*, 5(4), 2021.
- [17] Charles Drevon. Characterisation of an accordion lattice setup for a low-dimensional dipolar quantum gases experiment. Master's thesis, Universität Heidelberg, 2023.
- [18] A. Einstein. Quantentheorie des einatomigen idealen Gases. *Königliche Preußische Akademie der Wissenschaften. Sitzungsberichte*, Gesamtsitzung vom 10. Juli 1924(261-267), 1924.
- [19] T.H. Fay and P.H. Kloppers. The Gibbs' phenomenon. *IJMEST*, 32(1), 2001.
- [20] R.W. Floyd and L. Steinberg. An adaptive algorithm for spatial gray-scale. *Proceedings of the Society of Information Display*, 17(2), 1976.
- [21] Jianshun Gao. A First Two-Dimensional Magneto-Optical Trap for Dysprosium. Master's thesis, Universität Heidelberg, 2022.
- [22] A. L. Gaunt, T. F. Schmidutz, I. Gotlibovych, R. P. Smith, and Z. Hadzibabic. Bose-Einstein Condensation of Atoms in a Uniform Potential. *Phys. Rev. Letters*, 110(200406), 2013.
- [23] J. W. Gibbs. Fourier's series. *Nature*, 59(1522), 1898.
- [24] S. Gionvanazzi and D.H.J. O'Dell. Instabilities and the roton spectrum of a quasi-1D Bose-Einstein condensed gas with dipole-dipole interactions. *Eur. Phys. J. D*, 31(439-445), 2004.
- [25] D. Gottlieb and C.-W. Shu. On the Gibbs phenomenon and its resolution. *SIAM review*, 39(4), 1997.
- [26] R. Grimm, M. Weidemüller, and Y. B. Ovchinnikov. Optical dipole traps for neutral atoms. *Advances in Atomic, Molecular and optical Physics*, 42(pages 95-170), 2000.
- [27] Giacomo Guarda. Engineering Arbitrary Optical Potentials for Ultracold Gases. Master's thesis, Università di Trento, 2024.
- [28] Gauthier Guillaume. *Transport and Turbulence in Quasi-Uniform and Versatile Bose-Einstein Condensates*. PhD thesis, University of Queensland, 2020.
- [29] B. Gustafsson. The Work of David Gottlieb: A Success Story. *Commun.Comput. Phys.*, 9(3), 2011.
- [30] Christian Götzhäuser. Building a new Dy quantum gas experiment, 2021.
- [31] R.M. Haralick, K. Shanmugam, and I. Dinstein. Textural Features for Image Classification. *IEEE Transactions on Systems, Man and Cybernetics*, 3(6), 1973.
- [32] W. He, Y. Han, W. Ming, J. Du, Y. Liu, Y. Yang, L. Wang, Y. Wang, Z. Jiang, C. Cao, and J. Yuan. Progress of Machine Vision in the Detection of Cancer Cells in Histopathology. *IEEE Access*, 10(pp. 46753-46771), 2022.
- [33] R. Horstmeyer, R. Heintzmann, G. Popescu, L. Waller, and C. Yang. Standardizing the resolution claims for coherent microscopy. *Nature Photonics*, 10(2), 2016.
- [34] S. Jin, J. Gao, K. Chandrashekhara, C. Götzhäuser, J. Schöner, and L. Chomaz. Two-dimensional magneto-optical trap of dysprosium atoms as a compact source for efficient loading of a narrow-line three-dimensional magneto-optical trap. *Physical Review A*, 108(023719), 2023.

- [35] P. Juhász, M. Krstajić, D. Strachan, E. Gandar, and R. P. Smith. How to realize a homogeneous dipolar Bose gas in the roton regime. *Physical Review A*, 105(061301), 2022.
- [36] K.B.Davis, M.-O. Mewes, M.R. Andrews, N. J. van Druten, D.M. Kurn D.S.Durfee, and W. Ketterle. Bose-Einstein Condensation in a Gas of Sodium Atoms. *Physical Review Letters*, 75(22), 1995.
- [37] Marcel Kern. Enhanced Local Control of Two-Dimensional Ultracold Atomic Clouds. Master's thesis, Universität Heidelberg, 2024.
- [38] M. Klawunn and L. Santos. Hybrid multisite excitations in dipolar condensates in optical lattices. *Phys. Review A*, 80(013611), 2009.
- [39] L. Landau. Theory of the Superfluidity of Helium II. *Physical Review*, 60(356), 1941.
- [40] T.D. Lee, K. Huang, and C.N. Yang. Eigenvalues and Eigenfunctions of a Bose System of Hard Spheres and Its Low-Temperature Properties. *Phys. Review*, 106(6), 1957.
- [41] H. Li, J.-F. Wyart, O. Dulieu, and M. Lepers. Anisotropic optical trapping as a manifestation of the complex electronic structure of ultracold lanthanide atoms: The example of holmium. *Physical Review A*, 95(062508), 2017.
- [42] J. Liang, R. N. Kohn Jr., M. F. Becker, and D. J. Heinzen. 1.5% root-mean-square flat-intensity laser beam formed using a binary amplitude spatial light modulator. *Applied Optics*, 48(10), 2009.
- [43] Y. Lu, C. M. Holland, and L. W. Cheuk. Molecular Laser-Cooling in a Dynamically Tunable Repulsive Optical Trap. *Physical Review Letters*, 128(213201), 2022.
- [44] I. Manek, Y.B. Ovchinnikov, and R. Grimm. Generation of a hollow laser beam for atom trapping using an axicon. *Optics Communications*, 147(67-70), 1998.
- [45] Gabriele Natale. Spin physics in dipolar quantum gases of erbium atoms. Master's thesis, Università di Pisa, 2017.
- [46] N. Navon, R. P. Smith, and Z. Hadzibabic. Quantum gases in optical boxes. *Nature Physics*, 17(1334), 2021.
- [47] Christopher Palmer. *Diffraction Grating Handbook, 8th edition*. Richardson Gratings Newport Corporation MKS Instruments, 2020.
- [48] Sarah Philips. Characterizing a High-Resolution Imaging System for the Dysprosium Experiment. Master's thesis, Universität Heidelberg, 2023.
- [49] Lev Pitaevskii and Sandro Stringari. *Bose-Einstein Condensation and Superfluidity*. Oxford University Press, Reprint with corrections 2016.
- [50] S. M. Popoff, R. Gutiérrez-Cuevas, Y. Bromberg, and M. W. Matthès. A practical guide to Digital Micro-mirror Devices (DMDs) for wavefront shaping. *JPhys Photonics*, 6(4), 2024.
- [51] Bahaa E. A. Saleh and Malvin Carl Teich. *Fundamentals of Photonics*. Wiley Interscience, 1991.
- [52] E.C. Samson, K.E. Wilson, Z.L. Newmann, and B.P. Anderson. Deterministic creation, pinning, and manipulation of quantized vortices in a Bose-Einstein condensate. *Physical Review A*, 93(023603), 2016.

- [53] L. Santos, G.V. Shlyapnikov, and M. Lewenstein. Roton-Maxon Spectrum and Stability of Trapped Dipolar Bose-Einstein Condensates. *Physical Review Letters*, 90(25), 2003.
- [54] M. Schmitt, E. A. L. Henn, J. Billy, H. Kadau, T. Maier, A. Griesmaier, and T. Pfau. Spectroscopy of a narrow-line optical pumping transition in dysprosium. *Optics Letters*, 38(5), 2013.
- [55] Joschka Schöner. Magnetic-Field Setup for Magneto-Optical Trapping and Interaction Tuning in a Novel Dysprosium Quantum Gas Experiment. Master's thesis, Universität Heidelberg, 2022.
- [56] Valentina Salazar Silva. The Accordion Lattice: Towards Trapping of Dysprosium Ultracold Gases in Two Dimensions. Master's thesis, Universität Heidelberg, 2023.
- [57] M. Tajik, B. Rauer, T. Schweigler, F. Cataldini, J. Sabino, S.-C. Ji F. S. Møller, I. E. Mazets, and J. Schmiedmayer. Designing arbitrary one-dimensional potentials on an atom chip. *Optics Express*, 27(33474), 2019.
- [58] L. Tanzi, E. Lucioni, F. Famà, J. Catani, A. Fioretti, C. Gabbanini, R. N. Bisset, L. Santos, and G. Modugno. Observation of a Dipolar Quantum Gas with Metastable Supersolid Properties. *Physical Review Letters*, 122(130405), 2019.
- [59] L. Tanzi, S.M. Rocuzzo, E. Lucioni, F. Famà, A. Fioretti, C. Gabbanini, G. Modugno, A. Recati, and S. Stringari. Supersolid symmetry breaking from compressional oscillations in a dipolar quantum gas. *Nature*, 574(382–385), 2019.
- [60] Texas Instruments. *DLP9000 Family of 0.9 WQXGA Type A DMDs*, 2016.
- [61] Texas Instruments. *DLP6500 .65 1080p MVSP Type A DMD datasheet (Rev. A)*, 2021.
- [62] ViALUX. *SuperSpeed V-Modules*, 2023.
- [63] Charles S. Williams. *Introduction to the Optical Transfer Function*. SPIE - The International Society for Optical Engineering, 2002.
- [64] F. Zernike. Beugungstheorie des Schneidenverfahrens und seiner verbesserten Form der Phasenkontrolle. *Physica*, 1(8), 1934.

# Acknowledgements

As this thesis project comes to a close, I would like to thank some people who have accompanied me on the way. First and foremost, would like to thank Lauriane Chomaz for being an exceptional supervisor and for her guidance and advice whenever I needed it. Thanks also to Selim Jochim for taking over the task of being second examiner.

A big thank you goes out to all current and former members of the Quantum Fluids group, especially to Karthik Chandrashekhara for being at least equally invested in the DMD setup as I myself and performing much of the heavy lifting including the setup in the main experiment. Special thanks also to Manon Ballu for proofreading the technical sections of my thesis and to Jianshun Gao and Guo-Xian Su for helping out with any minor problem or question I ever brought to them. Thanks to Wyatt Kirkby, Lennart Hoenen, Felix Kaufmes, Fabio Castañeda, Lea Neumann, Paula Seyfert, Tom Jacobsen, Eilon Zohar and Lennart Naeve for our lunchtime discussions, group parties and for creating a group atmosphere which I always cherished especially when writing the next sentence or even the next word of this thesis became unbearable. I hope to see you all soon in Dr. Jin's Café & Bar ;). Thanks also to former group members Shuwei Jin, Sarah Philips, Valentina Salazar Silva and Charles Drevon and all others whose work lead up to the successful implementation of our DMD setup.

A big thank you to Thibault Bourgeois for the many discussions on the DMD setup in general, his filtering algorithm and on density perturbations. The same goes also for Marcel Kern and his errormap algorithm and Marius Sparrn from the BECK experiment at the KIP. Thanks for the discussions also to Michael Rautenberg and Tobias Krom of the LiCs team and Juan Provencio Lameiras, former member of the HQA team.

Thanks also to the team of the mechanical workshop of the PI, in particular Leonard Lowe and Stefan Hummel from the design department and Andreas Düll and Denis Hoffmann from the construction department for keeping up with all my big and small projects over the past year, even if many of them were not or only loosely related to the DMD setup.

Thank you to all my fellow musicians of the AufTakt and APH orchestras for regularly taking my mind off of my Master project for some hours and thank you to my friends Jonathan and Patrick for doing the same during our regularly scheduled Thursday night meetings.

Perhaps the biggest thank you goes out to my family, my parents and my brother and to my wonderful girlfriend Rahel for their unconditional support at every step of the way.

Last but not least, I wish to say a final thank you to my dear grandmother Erna Losekam, who unlike myself never had any doubts I would be successful in my endeavours even if she was not entirely sure what they incorporated and who sadly passed away on the very day that I finally finished this thesis and hopefully proved her right.

# Erklärung

Ich versichere, dass ich diese Arbeit selbstständig verfasst und keine anderen als die angegebenen Quellen und Hilfsmittel benutzt habe.

Heidelberg, den 14.03.2025,

A handwritten signature in black ink, consisting of a large, stylized initial 'C' followed by a series of loops and a long horizontal stroke extending to the right.